Magnetic Resonance Study of Two-Phase Gas-Liquid Systems: Acoustic Cavitation and Vertical Bubbly Flow

by

Aidin Arbabi

Master of Science, Royal Institute of Technology (KTH), Sweden, Stockholm, 2009

A Dissertation Submitted in Partial Fulfillment
of the Requirements for the Degree of

Doctor of Philosophy

in the Graduate Academic Unit of Physics

Supervisor: Igor V. Mastikhin, Ph.D., Physics

Examining Board: Andrew Gerber, Ph.D., Mechanical Engineering
Benedict Newling, Ph.D., Physics
Bruce Balcom, Ph.D., Physics

External Examiner: Josep Seymour, Ph.D., Dept. of Chemical and Biological Engineering, Montana State University

This dissertation is accepted by the
Dean of Graduate Studies

THE UNIVERSITY OF NEW BRUNSWICK

February, 2015

©Aidin Arbabi, 2015

ABSTRACT

We performed magnetic resonance studies of gas-liquid systems: acoustic cavitation and vertical bubbly flow to obtain information about the water molecules mobility, bubble size, and void fraction, critical for a better understanding of these complex dynamic systems.

A varying magnetic susceptibility between the phases in gas-liquid systems fundamentally limits the employment of conventional magnetic resonance imaging methods for quantitative measurements. Susceptibility effects can be removed with the addition of paramagnetic salts to the solution. We, however, decided to use the susceptibility difference to extract useful information about bubble size, provided its image distortion effects are overcome. Pure phase encode imaging methods are suitable means for the quantitative measurement of these heterogeneous systems, as they incorporate fixed encoding times.

A significant modulation of the magnetic resonance parameters, as driven by susceptibility, necessitates short signal acquisition times. The fast dispersion of water molecules in the acoustically cavitating liquid permitted the employment of pure phase encode imaging methods with short phase encoding times to obtain 3D voidage and velocity maps. Compressibility, divergence, and vorticity maps of the cavitating medium were also created.

The average bubble size, both bulk and spatially resolved, was extracted for the vertical bubbly flow from the susceptibility-modulated T_2^*. For that, an analytical approach with two significantly different measurement regimes was employed. The fast mobility of water spins with respect to the short encoding times in the employed pure phase encode

methods satisfied the fast diffusion regime requirements. A good agreement was observed between magnetic resonance and optics-based estimates of bubble sizes for the slower airflow rates.

Bulk measurements of vertical bubbly flow were also performed at low magnetic field. We analyzed the susceptibility-induced effects in the Carr-Purcell-Meiboom-Gill signal using new analytical approaches, and derived two simplified equations for voidage and inclusion size estimation with basic relaxometry. The approach introduced was validated through control measurements on silica bead solutions with known bead sizes, and through comparison with measurements performed using an optics-based technique. The developed approach worked well for both control samples and bubbly flows.

Our approach can also be used to study other gas-liquid systems with spherical non-interacting inclusions, like gas hydrates and sprays, provided all the theoretical requirements are met.

DEDICATION

To my dearests: Bahareh, Shanli, and Ayli

ACKNOWLEDGEMENTS

I would like to express my special thanks to Prof. Igor V. Mastikhin, my supervisor, for his encouragement, guidance, and support over the course of my Ph.D. study at UNB, and my wife, Bahareh, for her patience and support during all these long years.

I would also like to thank Prof. Bruce Balcom, the Director of the UNB MRI centre. I was very fortunate having the chance of attending his graduate MRI course, during which I hugely extended my knowledge of MRI physics. He also never hesitated to share his valuable experience.

I am thankful of Dr. F. Marica for his helpful tips during my measurement on the DRX 8.52 MHz magnet. I also thank Mr. R. MacGregor for his helpful and friendly assistance throughout my Ph.D. study with the experiments on 2.4 T Nalorac and 4.8 T Cryomagnetics magnets.

For financial support, I greatly acknowledge New Brunswick Foundation for Innovation and Natural Sciences and Engineering Research Council of Canada.

Table of Contents

ABSTRACT ii
DEDICATION iv
ACKNOWLEDGEMENTS v
Table of Contents vi
List of Figures x
List of Symbols, Nomenclature or Abbreviations xv
1 – Introduction 1
1.1 Two-phase gas-liquid systems 1
1.1.1 Acoustic cavitation 1
1.1.2 Bubbly flow 2
1.2 Available methods 3
1.3 Experimental studies 5
1.4 Thesis organization 8
1.5 References 10
2 – Magnetic resonance imaging theory 15
2.1 Why MRI? 15
2.2 A system perspective 15
2.3 Signal generation and detection 16
2.3.1 Magnetic dipole moments 16
2.3.2 Larmor frequency 20
2.3.3 RF excitation 21
2.3.4 Free precession and relaxation 21

2.3.5 Signal detection 23

2.4 Signal characteristics 24

2.4.1 Free induction decay signal 24

2.4.2 Spin echo 25

2.4.3 Carr-Purcell-Meiboom-Gill 26

2.4.4 Pulsed magnetic field gradient spin echo 29

2.5 Signal localization 32

2.5.1 K-space 33

2.6 More advanced MR pulse sequences 35

2.6.1 3D conical single point ramped imaging with T_1 enhancement 35

2.6.2 3D motion sensitized single point imaging spin echo 38

2.7 Magnetic susceptibility 41

2.8 References 42

3 - Magnetic resonance imaging of velocity fields and the void fraction in a cavitating liquid 44

3.1 Introduction 44

3.2 Experimental 46

3.3 Results and discussion 49

3.3.1 Void fraction measurements 49

3.3.2 Velocity measurements 56

3.4 Conclusion 65

3.5 References 67

4 - Magnetic susceptibility based Magnetic Resonance estimation of micro-bubble size for the vertically upward bubbly flow 69
4.1 Introduction 69

4.2 Theory 70

4.3 Methods 75

4.3.1 Bulk measurements of void fraction, T_2^*, and diffusion: 77

4.3.2 3D measurements of void fraction, T_2^*, and diffusion: 77

4.4 Results and Discussion: 80

4.4.1 Bulk Measurements: 80

4.4.2 Spatially Resolved Measurements: 86

4.5 Conclusion: 93

4.6 References: 96

5 - MR relaxometry of micro-bubbles in the vertical bubbly flow at a low magnetic field (0.2 T) 98
5.1 Introduction 98

5.2 Theory 100

5.3 Methods 105

5.3.1 Bulk measurements of void fraction, D, and T_2: 108

5.4 Results and Discussion 109

5.4.1 Control Measurements 109

5.4.2 Bubbly Flow Measurements 113

5.5 Conclusion 121

5.6 References 124

6 – Conclusion and future work 127
6.1 Conclusion 127

6.2 Future work 129

6.3 References 133

Curriculum Vitae

List of Figures

Figure 2-1 Magnetic moment vectors $\vec{\mu}$: (A) randomly oriented, and (B) pointing aligned in the direction of the external magnetic field B_0, either pointing parallel or anti-parallel (for ^1H). As seen, the transverse components of the spin vectors are still randomly oriented in the presence of the external magnetic field B_0, leading to a zero net magnetization in the XY plane..... 18

Figure 2-2 The Carr-Purcell-Meiboom-Gill pulse sequence: A 90° RF pulse is followed by a train of 180° pulses to form multiple echoes by continuously refocusing the frequency offsets. The number of echoes, which can be generated, is limited by the T_2 of the sample. By maintaining a short time interval $2\tau_{180}$ between pulses and employing more refocusing pulses, one can minimize the attenuation effect of diffusion. The 90° phase difference between the excitation pulse and the following refocusing pulses corrects for any 180° pulse length error due to the B_1 field inhomogeneity for every second echo. 28

Figure 2-3 The pulsed field gradient spin echo pulse sequence: Similar to the SE pulse sequence with the addition of a pair of displacement encoding gradients in the direction of interest. The gradients are employed to encode the molecular self-diffusion in the system. In practice, the experiment is performed with different values of the diffusion gradients, and, then, diffusion is calculated from the slope of the $\ln(S(G_d)/S(0))$ vs. b-factor curve..... 31

Figure 2-4 3D pure phase encode conical single point ramped imaging with T_1 enhancement: only a few first points of a single cone are illustrated while, in practice, 39 cones are implemented for k-space sampling. 37

Figure 2-5 3D motion sensitized pure phase encode single point imaging spin echo: A composite refocusing hard excitation pulse can be incorporated for more accurate excitation, as illustrated. Only phase encoding in one direction is shown. 40

Figure 3-1 Experimental setup. All distances are in mm. 47

Figure 3-2 Middle slices from 3D void fraction maps for water (A) and SDS solution (B). The vertical direction corresponds to the Y (vertical) orientation in the magnet. The horizontal direction is the Z orientation, with the externally applied magnetic field, against the ultrasound direction. The color scale is in percent of the density and is different in (A) and (B). 54

Figure 3-3 Z component of velocity maps for water (A) and SDS solution (B). The color scale is in m/s, and is different in (A) and (B). The inset at the top of figure 3-3 A is the profile of velocity at point #32 indicated by the dotted lines in (A) and (B). Figures (C) and (D) are slices across the cuvette at 1.25 mm from the tip of the horn (at pixel #16 in Z direction) through X component velocity maps for water and SDS solution. 58

Figure 3-4 Middle slices of divergence maps for water (A) and SDS solution (B). C and D are the corresponding slices of V.grad(lnφ): The vertical direction corresponds to the Y (vertical) orientation, the horizontal is in the Z orientation, against the ultrasound direction. The color scale is in s^{-1}, as for (A) and (B). 61

Figure 3-5 Middle slices of vorticity (curlV magnitudes for water (A) and SDS (B) solutions in s^{-1}). C and D show the angular velocities around the direction of the flow for water and SDS solutions, respectively. 64

Figure 4-1 Theoretical analysis (Eqs. (3) and (4)): (A) Bubble-induced relaxation rate in s^{-1} vs. bubble radius in mm for the measurement time of 2 ms for various diffusion coefficients. The fast diffusion limit (Eq. (4)) is plotted in the dashed line for the diffusion coefficient D of 10^{-5} m^2/s. (B) The same for the measurement time of 15 ms and the diffusion coefficients D values of $1*10^{-5}$, $5*10^{-6}$, and $1*10^{-6}$ m^2/s. The fast diffusion limit (Eq. (4)) is plotted in solid, dashed, and dotted lines for the same diffusion values. 74

Figure 4-2 Experimental setup. 76

Figure 4-3 The relation between void fraction and flow rate in CCPM: (A) bulk, (B) volume averaged (t_p= 0.1 ms), and (C) volume averaged (t_p= 1 ms). Void fraction is normalized. (D) The bulk bubble-induced relaxation rate in s^{-1} vs. airflow rate in CCPM. 81

Figure 4-4 The T_2^*-diffusion distribution map for the airflow rates of: (A) 12.43, (B) 36.37, and (C) 94.92 CCPM. Axes are in logarithmic scales. (D) The average bubble radius estimates in mm measured with bulk MR and optical methods for 6 different airflow rates. 85

Figure 4-5 The middle slice of the R-square map for: (A) T_2^* fit of the SPRITE T_2^* mapping, and (B) diffusion fit of the SE-SPI diffusion mapping. R^2 value closer to 1 is indicative of a good agreement with the mono-exponential decay. The pixel size in the Z and X or Y direction is 0.625 mm and 0.47 mm, respectively. Maps correspond to the airflow rate of 36.37 CCPM. 88

Figure 4-6 The 3D void fraction map: (A) middle slice, and (B) axial view. The color scale shows void fraction numbers. The 3D bubble-induced relaxation rate map: (C) middle slice, and (D) axial view. The color scale is in s^{-1}. The position of the axial views is indicated by the white dashed line for each case. The pixel size in the Z and X or Y direction is 0.625 mm and 0.47 mm, respectively. Maps correspond to the airflow rate of 36.37 CCPM..... 90

Figure 4-7 (A) The middle slice of the 3D diffusion map. The color scale is in m^2/s. (B) The middle slice of the average bubble radius distribution map. The color scale is in meters. The vacant spaces correspond to zero void fraction and bubble-induced relaxations rate values. The pixel size in the Z and X or Y direction is 0.625 mm and 0.47 mm, respectively..... 92

Figure 5-1 Experimental setup for bubbly flow measurements..... 107

Figure 5-2 Susceptibility induced relaxation rate vs. echo time in the 1 μm silica bead suspension: A direct relation between the induced relaxation rate and echo time is shown. The scale on the horizontal and vertical axes is in s and s^{-1}, respectively. Error bars represent the standard error. The bigger error for longer echo times is due to the smaller number of echoes acquired..... 111

Figure 5-3 Mechanical dispersion vs. Δ in the bubbly flows: Direct dispersion-airflow rate and dispersion-Δ relations are observed. The scale on the horizontal and vertical axes is in s and m^2/s, respectively..... 115

Figure 5-4 Bubble induced relaxation rate vs. echo time in the bubbly flows: A direct relation between the induced relaxation rate, echo time, and airflow rate is observed.

The scale on the horizontal and vertical axes is in s and s^{-1}, respectively. Error bars represent the standard error..... 117

Figure 5-5 (A-C) Bubble size distribution obtained using the optical method for 3 different airflow rates. The scale on the horizontal axis is in mm. (D) Average bubble size estimates from the MR (Eqs. (5) and (8)) and optical techniques. The scale on the horizontal and vertical axes is in CCPM and mm, respectively. Error bars represent the standard error. 119

List of Symbols, Nomenclature or Abbreviations

MR	Magnetic resonance
MRI	Magnetic resonance imaging
RF	Radio frequency
SNR	Signal to noise ratio
FOV	Field of view
CCPM	cubic centimeter per minute
FID	Free induction decay signal
SE	Spin echo
SE-SPI	Spin echo single point imaging
CPMG	Carr-Purcell-Meiboom-Gill
PFGSE	Pulsed field gradient spin echo
SPRITE	Single point ramped imaging with T_1 enhancement
LD	Laser diffraction
PD	Phase Doppler
PIV	Particle imaging velocimetry
SDS	Sodium dodecyl sulfate
$\vec{\mu}$	Magnetic dipole moment
μ_z	Z component of the magnetic dipole moment
$\vec{j}$	Spin angular momentum
I	Spin quantum number
m_I	Magnetic quantum number
γ	gyromagnetic ratio

$N_{\uparrow}$	Number of spins pointing upwards
$N_{\downarrow}$	Number of spins pointing downwards
N_s	Total number of spins
$E_{\uparrow}$	Energy of the spin-up state
$E_{\downarrow}$	Energy of the spin-down state
ΔE	Energy difference between the spin states
k	Boltzmann constant
$\bar{h}$	Planck's constant divided by 2π
T_s	Absolute temperature of the spin system
α	Flip angle
E_{rf}	Radiation energy of the RF pulse.
ω_{rf}	Resonance frequency of the RF pulse.
B_0	Uniform static magnetic field
B_1	Rotating magnetic field
$\Delta B(r)$	Field offset
ω_0	Larmor frequency
ω	Resonance frequency
$\Delta\omega$	Offset frequency
M_z^0	Bulk magnetization at thermal equilibrium
$M_{xy}(0_+)$	Magnetization in the transverse plane right after the RF pulse
$M_z(0_+)$	Magnetization along the Z-axis right after the RF pulse
$M_{xy}(t)$	Transverse magnetization during the relaxation and free precession

$M_z(t)$	Longitudinal magnetization during relaxation and free precession
T	Tesla
g	Gauss
κ	Dimensionless volume susceptibility in CGS units
χ	Dimensionless volume susceptibility in SI units
χ_m	Molar susceptibility
$\Delta\chi$	Magnetic susceptibility difference
T_1	MR longitudinal relaxation lifetime
T_2	MR transverse relaxation lifetime
T_2^*	MR signal decay rate in an inhomogeneous field
τ^*	Time for the signal decay by e^{-1}
τ	Dimensionless time
τ_{pulse}	RF pulse length
t	Time
s	Second
min	Minute
t_{acq}	Acquisition time
t_E	Echo time
τ_{180}	Inter-echo time
TR	Repetition time
t_p	Phase encoding time
t_D	Characteristic diffusion time
t_c	Characteristic dephasing time

DW	Dwell time
S_0	Signal from the bulk liquid
S(G)	SE amplitude in the presence of diffusion gradients
S(0)	SE amplitude in the absence of diffusion gradients
$\Gamma(t)$	Signal attenuation function
ΔR_2	Magnetic susceptibility induced relaxation rate
R	Radius
r	Position
G	Gradient
G_d	Diffusion/velocity encoding gradient
G_f	Frequency encoding gradient
G_p	Phase encoding gradient
G_i	Background gradient
Δ	Diffusion observation time
δ	Diffusion encoding time
D	Mechanical dispersion/molecular diffusion coefficient
V	Velocity
φ	Void fraction (voidage)
ρ	Mass density
M	Molar mass
P	A dimensionless parameter

1 – Introduction

In this chapter, acoustic cavitation and vertically upward bubbly flow systems are introduced, as the current thesis is dedicated to magnetic resonance imaging (MRI) studies of these systems. The pros and cons of various available methods for their study are discussed, and, the advantages of MRI over other techniques are explained. A number of previous experimental studies on multiphase systems are introduced. Finally, we detail the scope of the thesis.

1.1 Two-phase gas-liquid systems

Multi-component systems in which a gaseous phase is dispersed throughout a liquid, known as two-phase gas-liquid systems, are commonly found in both nature and industry. These systems occur in many situations of theoretical and practical interest: from cavitation (both hydraulic and acoustic) and foams to pipeline systems for the transport of oil-gas mixtures and evaporators.

1.1.1 Acoustic cavitation

Acoustic cavitation is the process of formation, evolution, and collapse of bubbles caused by the propagation of an acoustic wave through a liquid medium. The highly nonlinear concentration of acoustic energy inside the collapsing bubbles leads to extreme temperature and pressure conditions that can be employed in biomedicine, chemistry, and industry [1].

An important parameter of cavitation is the bubble void fraction or voidage (i.e. the fraction of the volume of the liquid phase occupied by gas). Another important property is the velocity field of the cavitating liquid, as it is linked to the dynamics of the bubble cloud, both at micro and at macro-scales. Oscillating bubbles generate microstreaming, causing an active mixing, and, at low ultrasound frequencies, are also primarily responsible for the macroscopic flow (acoustic streaming), caused by energy transfer from the acoustic field, via the bubbles, to the liquid.

1.1.2 Bubbly flow

One of the most common geometries of two-phase gas-liquid systems is pipe flow. In this type of flow, two phases move simultaneously, most commonly, in horizontal or vertical pipe configurations. The gravity (buoyancy) causes the gas phase to rise: rising upward in vertical pipes and to the upper part of the pipe in horizontal ones. There are limited theories and measurement capabilities available in the field due to the complexity, deformability, and compressibility of the phases. Relative flow rates, fluid properties, and geometries determine the structure of a pipe flow [2]. Depending on the flow rate and the gas to liquid ratio, four main flow patterns are usually defined for vertical pipe flows [3].

Bubbly flow: This regime occurs at low gas to liquid ratio (slow flow rates). The gas phase appears in the form of bubbles with various sizes throughout the liquid phase. These bubbles are small compared to the diameter of the pipe, and their shape is not significantly influenced by the pipe walls [3]. Bubbly flow, itself, is usually classified into four sub regimes depending on the magnitude of interaction among interfaces [4]: ideally separated bubbly flow, interacting bubbly flow, churn turbulent bubbly flow, and

clustered bubbly flow. In ideally separated bubbly flow, no direct or indirect interaction is observable between bubbles, and bubbles exist as single objects in the liquid phase. Transition from the ideally separated bubbly flow to the interacting bubbly flow, where direct or indirect interactions among bubbles occur through collisions, happens for higher void fractions. With a further increase in the void fraction, bubbles coalesce, and flow changes to churn turbulent bubbly flow. The transition from the bubbly flow to the slug flow regime occurs during the clustered bubbly flow regime. Here coalesced bubbles (so called cap bubbles) and smaller bubbles co-exist. Cap bubbles, after traveling a certain distance, form a gas slug or separate into individual bubbles.

Three other regimes occur at even greater flow rates and void fractions. *Slug (plug) flow:* the gas phase appears mostly as large bullet shaped bubbles and sometimes small bubbles distributed throughout the liquid phase, *Churn flow:* a highly unstable and turbulent flow pattern; the liquid phase pulses up and down at the pipe wall, and *Annular flow:* the gas phase travels through the center of the pipe while the liquid phase appears partly as drops scattered in the gas phase and partly as an annular film on the pipe wall [5].

Void fraction and bubble size distribution are two properties of interest in all such systems.

1.2 Available methods

Various experimental techniques have been developed to study these parameters. The most prominent are photographic techniques, which are employed for quantification of

the bubble size by obtaining photographs of the system through a transparent section of the column [6].

Laser tomography permits visualization of the active zones with a great accuracy [7]. In this method, monochromatic laser light is applied to the sample. Diffraction of the light by cavitation bubbles is then employed to identify the zones of high bubble density.

Recently developed acoustical techniques are used for the indirect measurement of the bubble size distribution in a pulsed acoustic field [8]. Here, the solution is exposed to ultrasound pulses separated by a pulse off-time. The pulse off-time is increased until the sonoluminescence intensity is diminished as a result of bubbles' dissolution. Then, the total dissolution time of bubbles is used for the bubble size calculation.

Optical techniques, based on tracing particles added to the liquid (particle imaging velocimetry), permit spatial mapping of the velocity fields [9-10]. Here, the liquid medium is seeded by fluorescent tracers. Then, a plane in the flow is illuminated by a laser light in order to track the positions of particles in that plane using a digital camera. A few moments later, another laser pulse illuminates the same plane, creating a second particle image. From these two images, the particle displacements are obtained for the entire flow region. As only the displacement of the fluorescent tracers from picture to picture is of interest, a high pass filter is applied on the digital camera to make the cavitation bubbles transparent.

However, all these methods have significant limitations. Optical methods require transparency of the media, suffer from light reflection from the bubble-liquid interface, have limited measurement depth, and are limited to relatively low gas fractions. Laser tomography provides only qualitative information, and acoustical techniques do not

provide a direct way of measurement, and, like optical techniques, fail at high void fractions. For the measurement of bubble sizes in systems with high void fractions, many invasive probes, such as hot film anemometry, have been developed. However, their intrusive nature is a source of systematic errors [11].

MRI is a promising technique to study gas-liquid systems. Its non-invasive nature does not interfere with the gas-liquid interface, and it can be used for the study of optically and acoustically opaque systems. It is inherently a 3D method, and the information-carrying signal comes directly from the bulk of the sample. MRI can also be rendered sensitive to various parameters like spin density and relaxation rates.

1.3 Experimental studies

There are a limited number of MRI studies of gas-liquid systems in the literature; only a few of them are referred to here. Lynch and Segel first examined bubbly flows using magnetic resonance (MR). They demonstrated the linear relationship between the MR signal intensity and the volume-averaged void fraction in a vertical bubbly flow using continuous wave MR spectroscopy [12]. Abouelwafa and Kendall measured the void fraction and flow rate in two-phase water-oil and water-air flow systems using continuous wave nuclear magnetic resonance (NMR) spectroscopy [13]. Leblond et al. measured the volume averaged void fraction and the velocity propagator of the liquid phase through the basic pulsed field gradient spin echo (PFGSE) sequence [14]. Le Gall et al. also used PFGSE to study liquid velocity fluctuations in bubbly flow in different geometries [15]. Daidzic et al. obtained a spatially resolved void fraction map in a stationary water column in a permanent magnet using a conventional spin-warp pulse sequence [16].

Holland et al. determined bubble sizes from MRI signal using a Bayesian technique [17]. Reyes obtained 2D temporally resolved measurements in gas-liquid slug flow [18]. Gladden et al. demonstrated both spatial and temporal resolution MRI measurements on a gas-liquid system [19]. They performed quantitative visualization of these dynamic, optically opaque, and magnetically heterogeneous systems using a modified version of the frequency encoding based Turbo Spin Echo sequence. Visualizing the movement of bubbles in a ceramic monolith over a very short time scale of 146 ms enabled them to track individual gas bubbles and obtained information about bubble size distribution and velocity. Tayler et al. used a low flip angle snapshot spiral imaging method for the measurement of spatially and temporally resolved velocity fields of unstable flow systems and assessed the method as an "auspicious basis" for the study of these kinds of samples [20]. They doped the liquid phase with a paramagnetic salt to remove the magnetic susceptibility induced distortions.

Instead of removing the susceptibility difference in the system with paramagnetic salts, one can exploit it to obtain information about the bubble size and density. This approach, complementary to tracing individual bubbles, has been applied to measurements of stabilized gas-filled micro-bubbles. Alexander et al. did preliminary research on the effects of pressure-stable liposome micro-bubbles filled by several different gases and gas concentrations on MR relaxation times at various pressures through the conventional SE and gradient echo pulse sequences [21]. Dharmakumar et al. derived analytical expressions which take into account the void fraction, diffusion, and average bubble radius to qualitatively explain the functional behavior of T_2 and T_2^* decays [22]. Morris et al. have presented an MRI-based technique for spatially resolved pressure mapping in

porous media with a multi-slice multi-echo pulse sequence using air-filled liposome micrometer-sized bubbles as pressure sensitive MR contrast agents [23,24]. Sukstanskii and Yablonskiy have provided a detailed theoretical description of the FID and SE signal formation in the framework of the Gaussian phase distribution approximation for permeable and impermeable spherical and infinitely long cylindrical inclusions [25,26]. Ziener et al. analyzed the CPMG transverse relaxation rate as a function of inter-echo time in the Gaussian approximation framework for a simple model of a spherical particle [27].

Conventional MRI techniques (i.e. frequency encoding based) can suffer from susceptibility induced image distortions, which make quantitative data collection difficult. Very fast diffusion observed in bubbly flows contributes to the problem. However, it is known from research in MRI of porous media that one can use the susceptibility effects to one's advantage to obtain information on pore size distribution and other properties of porous materials by using pure phase encode MRI methods. These methods, unlike frequency-encoding MRI techniques, achieve immunity to the time domain artifacts by freezing the signal time evolution [28]. There are a number of MRI studies of gas-liquid systems using pure phase encode MRI techniques. Sankey et al. studied horizontal bubbly flow using the pure phase encode SPRITE MRI technique [29]. They acquired quantitative liquid velocity maps and an approximate void fraction of gas-liquid flow. Mastikhin et al. studied the dynamics of acoustically cavitated liquid with conical single point ramped imaging with T_1 enhancement (SPRITE) MRI to obtain spatially resolved velocity and void fraction maps of cavitating distilled water and surfactant solutions [30]. Arbabi and Mastikhin in [31] obtained bulk and spatially

resolved T_2 relaxation and mechanical dispersion information of vertical bubbly flow at various airflow rates with conical SPRITE and motion-sensitized single point imaging spin echo (SE-SPI). They estimated average bubble sizes using analytical expressions, originally developed by Dharmakumar et al. [22].

1.4 Thesis organization

The thesis is organized as follows:

Chapter 2 briefly reviews the basic principles of MRI. Only ideas and methods directly relevant to the subsequent chapters will be covered.

Chapter 3 describes a new method to measure 3D void fraction maps and to estimate water mobility in the vicinity of cavitating bubbles using pure phase encode MRI. Compressibility, divergence, and vorticity maps of the cavitating medium will also be presented, calculated from the 3D void fraction and velocity maps. This chapter is largely based on the article "Magnetic resonance imaging of velocity fields and the void fraction in a cavitating liquid" published in Experiments in Fluids, 2012, 52, 95-104 [30].

Chapter 4 describes an approach, originally developed for the MR analysis of stable micro-bubbles, to study vertical bubbly flows. This chapter is largely based on the article "Magnetic susceptibility based Magnetic Resonance estimation of micro-bubble size for the vertically upward bubbly flow" published in the Journal of Magnetic Resonance, 225, 36-45, 2012 [31].

Chapter 5 describes the measurement of vertical bubbly flows in a low field strength magnet, 0.2 T, through another method. This method is based on the previously

introduced approaches, originally developed for the MR analysis of randomly distributed and isolated spherical inclusions and a simple model of a spherical particle. In this chapter two simplified equations are derived for the estimation of void fraction and size of spherical inclusions with basic relaxometry. This chapter is largely based on the article "MR relaxometry of micro-bubbles in the vertical bubbly flow at a low magnetic field (0.2 T)" published in the Journal of Magnetic Resonance, 2014, 249, 16-23 [32].

Chapter 6 presents concluding remarks and directions for future work related to the topics in the thesis.

The author of the thesis performed all of the experiments and undertook all of the data analysis in this thesis. He wrote the research articles corresponding to Chapter 3 as the second author and Chapters 4-5 as the first author.

1.5 References

[1] D. Flannigan and K. Suslick, "Plasma formation and temperature measurement during single-bubble cavitation", Nature, 2005, 434, 52–55.

[2] R.F. Mudde, "Gravity-driven bubbly flows", Annual Review of Fluid Mechanics, 2005, 37, 393-423.

[3] D. J. Nicklin, "Two-phase bubble flow", Chemical Engineering Science, 1962, 17, 693-702.

[4] M. A. Zubir, M. Z. Zainon, "Two phase flow behavior and pattern in vertical pipes", Journal of Applied Sciences, 2011, 11 (9), 1491-1500.

[5] A. J. Ghajar, "Non-boiling heat transfer in gas-liquid flow in pipes-a tutorial", Journal of the Brazilian Society of Mechanical Sciences and Engineering, 2005, 27.

[6] N.E. Tayali, C.J. Bates, "Particle sizing techniques in multiphase flows: A review", Flow Measurement and Instrumentation, 1990, 1(2), 77-105.

[7] R. Viennet, V. Ligier, J. Hihn, D. Bereziat, P. Nika, M. Doche, "Visualisation and electrochemical determination of the actives zones in an ultrasonic reactor using 20 and 500 kHz frequencies", Ultrasonics Sonochemistry, 2004, 11(3–4), 125–129.

[8] J. Lee, M. Ashokkumar, S. Kentish, F. Grieser, "Determination of the size distribution of sonoluminescence bubbles in a pulsed acoustic field", Journal of the American Chemical Society, 2005, 127(48), 16810–16811.

[9] A. Mandroyan, M. Doche, J. Hihn, R. Viennet, Y. Bailly, L. Simonin, "Modification of the ultrasound induced activity by the presence of an electrode in a sono-reactor

working at two low frequencies (20 and 40 kHz). Part II: Mapping flow velocities by particle image velocimetry (PIV)", Ultrasonics Sonochemistry, 2009, 16(1), 97–104.

[10] M. Choi, D. Doh, T. Hwang, C. Cho, D. Paeng, G. Rim, A. Coleman, "Acoustic streaming in lithotripsy fields: preliminary observation using a particle image velocimetry method", Ultrasonics, 2006, 44(2), 133–145.

[11] S.C. Saxena, D. Patel, D.N. Smith, J.A. Ruether, "An assessment of experimental techniques for the measurement of bubble size in a bubble slurry reactor as applied to indirect coal liquefaction", Chemical Engineering Communications, 1988, 63(1), 87-127.

[12] G. F. Lynch, S. L. Segel, "Direct measurement of void fraction of a 2-phase fluid by nuclear magnetic resonance", International Journal of Heat Mass Transfer, 1977, 20, 7–14.

[13] M. S. A. Abouelwafa, E. J. M. Kendall, "Optimization of continuous wave nuclear magnetic resonance to determine in situ volume fractions and individual flow rates in 2 component mixtures", Review of Scientific Instruments, 1979, 50, 1545–1549.

[14] J. Leblond, S. Javelot, D. Lebrun, L. Lebon, "Two-phase flow characterization by nuclear magnetic resonance", Nuclear Engineering and Design, 1998, 184, 229–237.

[15] F. Le Gall, S. Pascal-Ribot, J. Leblond, "Nuclear magnetic resonance measurements of fluctuations in air-water two-phase flow: pipe flow with and without `disturbing' section", Physics of Fluids, 2001, 13, 1118-1129.

[16] N. E. Daidzic, E. Schmidt, M. M. Hasan, S. Altobelli, "Gas–liquid phase distribution and void fraction measurements using MRI, Nuclear Engineering and Design, 2005, 235, 1163–1178.

[17] D.J. Holland, A. Blake, A.B. Tayler, A.J. Sederman, L.F. Gladden, "A Bayesian approach to characterising multi-phase flows using magnetic resonance: Application to bubble flows", Journal of Magnetic Resonance, 2011, 209, 83-87.

[18] J.N. Reyes, "The use of MRI to quantify multi-phase flow patterns and transitions: an application to horizontal slug flow", Nuclear Engineering and Design, 1998, 184, 213-228.

[19] L.F. Gladden, M.H.M. Lim, M.D. Mantle, A.J. Sederman, E.H. Stitt, "MRI visualisation of two-phase flow in structured supports and trickle-bed reactors", Catalysis Today, 2003, 79–80, 203–210.

[20] A.B. Tayler, D.J. Holland, A.J. Sederman, L.F. Gladden, "Time resolved velocity measurements of unsteady systems using spiral imaging", Journal of Magnetic Resonance, 2011, 211,1–10.

[21] A.L. Alexander, T.T. McCreery, T.R. Barrette, A.F. Gmitro, E.C. Unger, "Microbubbles as novel pressure-sensitive MR contrast agents", Magnetic Resonance in Medicine, 1996, 35(6), 801-6.

[22] R. Dharmakumar, D.B. Plewes, G.A. Wright, "On the parameters affecting the sensitivity of MR measures of pressure with microbubbles", Magnetic Resonance in Medicine, 2002, 47, 264–273.

[23] R.H. Morris, M. Bencsik, A.K. Vangal, Y. Perrie, "Three-dimensional fluid pressure mapping in porous media using magnetic resonance imaging with gas-filled liposomes", Magnetic Resonance Imaging, 2007, 25, 509–512.

[24] R.H. Morris, M. Bencsik, N. Nestle, P. Galvosas, D. Fairhurst, A. Vangala, Y. Perrie, G. McHale, "Robust spatially resolved pressure measurements using MRI with novel buoyant advection-free preparations of stable microbubbles in polysaccharide gels", Journal of Magnetic Resonance, 2008, 193, 159–167.

[25] A.L. Sukstanskii, D.A. Yablonskiy, "Gaussian approximation in the theory of MR signal formation in the presence of structure-specific magnetic field inhomogeneities", Journal of Magnetic Resonance, 2003, 163, 236–247.

[26] A.L. Sukstanskii, D.A. Yablonskiy, "Gaussian approximation in the theory of MR signal formation in the presence of structure-specific magnetic field inhomogeneities. Effects of impermeable susceptibility inclusions", Journal of Magnetic Resonance, 2004, 167, 56–67.

[27] C.H. Ziener, T. Kampf, P.M. Jakob, W.R. Bauer, "Diffusion effects on the CPMG relaxation rate in a dipolar field", Journal of Magnetic Resonance, 2010, 202, 38–42.

[28] A.E. Marble, I.V. Mastikhin, R.P. MacGregor, M. Akl, G. LaPlante, B.G. Colpitts, P. Lee-Sullivan, B.J. Balcom, "Distortion free single point imaging of multi-layered composite sandwich panel structures", Journal of Magnetic Resonance, 2004, 168, 164-174.

[29] M. Sankey, Z. Yang, L. Gladden, M. L. Johns, D. Lister, B. Newling, "SPRITE MRI of bubbly flow in a horizontal pipe", Journal of Magnetic Resonance, 2009, 99, 126–135.

[30] I.V. Mastikhin, A.Arbabi, B. Newling, A. Hamza, A. Adair, "Magnetic resonance imaging of velocity fields, the void fraction and gas dynamics in a cavitating liquid", Experiments in Fluids, 2012, 52, 95–104.

[31] A. Arbabi, I.V. Mastikhin, "Magnetic susceptibility based magnetic resonance estimation of micro-bubble size for the vertically upward bubbly flow", Journal of Magnetic Resonance, 2012, 225, 36–45.

[32] A. Arbabi, J. Hall, P. Richard, S. Wilkins, and I. V. Mastikhin, "MR relaxometry of micro-bubbles in the vertical bubbly flow at a low magnetic field (0.2 T)", Journal of Magnetic Resonance, 2014, 249, 16-23.

2 – Magnetic resonance imaging theory

This thesis is mainly directed at the MRI study of acoustic cavitation and vertical bubbly flow. In this chapter, we briefly review the basic principles of MRI with particular emphasis on parts relevant to the subsequent chapters of the thesis. For more detailed information, the reader is referred to reference books [1-5].

2.1 Why MRI?

MRI is a tomographic imaging modality: with MRI one can produce images of internal physical and chemical characteristics of an object from externally measured MRI signal. MRI has distinct advantages over other imaging techniques. It operates in the radio frequency (RF) range, so no ionizing radiation is used, MR signal comes directly from the sample, MR images are very rich in information content, and various contrast factors can be employed. Unlike many other tomographic techniques, MRI can generate slices in any direction without changing the position of the sample or machine.

2.2 A system perspective

The main components of an MRI scanner are a static field magnet, magnetic field gradient system, and the RF system. The main magnet is a resistive, a permanent, or a superconducting magnet, and its function is to create a very strong uniform static magnetic field (B_0) to generate a net magnetization out of the spins in the sample. Usually superconducting magnets are employed, and this is one of the reasons why MRI scanners are expensive. They are usually between 0.2 to 3 T (even stronger in research systems);

very strong if compared to the Earth's magnetic field (~$5*10^{-5}$ T). The magnetic field gradient system is a set of three orthogonal gradient coils, which introduce a time varying gradient in the different directions of X, Y, and Z in the magnetic field. The gradient system is an important component of an MRI scanner, as it is essential for signal localization, slice selection, and spatial encoding. The efficacy of a gradient system is determined by its maximum strength and the rate at which this maximum gradient strength can be reached (i.e. rise time). The third component is the RF system. Its task is to generate the RF pulse to excite the nuclei, and also to receive the signal coming from the sample. This system produces an oscillating magnetic field, referred to as B_1, much weaker than the static magnetic field B_0 (but still strong enough to induce rotation of magnetization). Both the transmitter and receiver can be combined as a single coil, thus the name transceiver coil.

2.3 Signal generation and detection

2.3.1 Magnetic dipole moments

A fundamental property of nuclei is that those with odd atomic weights and/or odd atomic numbers, such as the nucleus of the hydrogen atom ^1H, have an angular momentum $\vec{J}$, often called spin. A nucleus with a nonzero spin creates a local magnetic field, which is represented by a vector quantity of $\vec{\mu}$, called the magnetic dipole moment or magnetic moment. The spin angular momentum and magnetic moment vectors are related to each other by $\vec{\mu} = \gamma.\vec{J}$, where γ is a physical constant known as the gyromagnetic ratio. A related constant $\bar{\gamma}$ is also widely used, which is defined as

$\bar{\gamma} = \gamma/2\pi$. The value of γ is nucleus dependent, for instance, γ=2.675*10^8 rad/s.T for ^{1}H, while γ=7.075*10^7 rad/s.T for ^{31}P.

Spins in a spin system are randomly oriented, thus leading to a zero magnetization (figure 2-1). In order to create a net magnetization, spin vectors are lined up by exposing the object to a strong external magnetic field B_0 (by convention along the z-axis). A magnetic moment vector, in the field B_0, can take one of a discrete set of orientations, which is determined by the magnetic quantum number m_I. For any nucleus with a nonzero spin, m_I takes the following set of values:

m_I=-I, -I+1, …, I (I is the spin quantum number) (1)

which corresponds to 2I+1 possible orientations for the Z component of $\vec{\mu}$ with respect to the direction of the external magnetic field. For instance, for ^{1}H with the spin quantum number $I = 1/2$, $m_I = \pm 1/2$, which corresponds to two possible orientations for the Z component of magnetic moments: pointing upward or parallel ($m_I = 1/2$) and pointing downward or anti-parallel ($m_I = -1/2$).

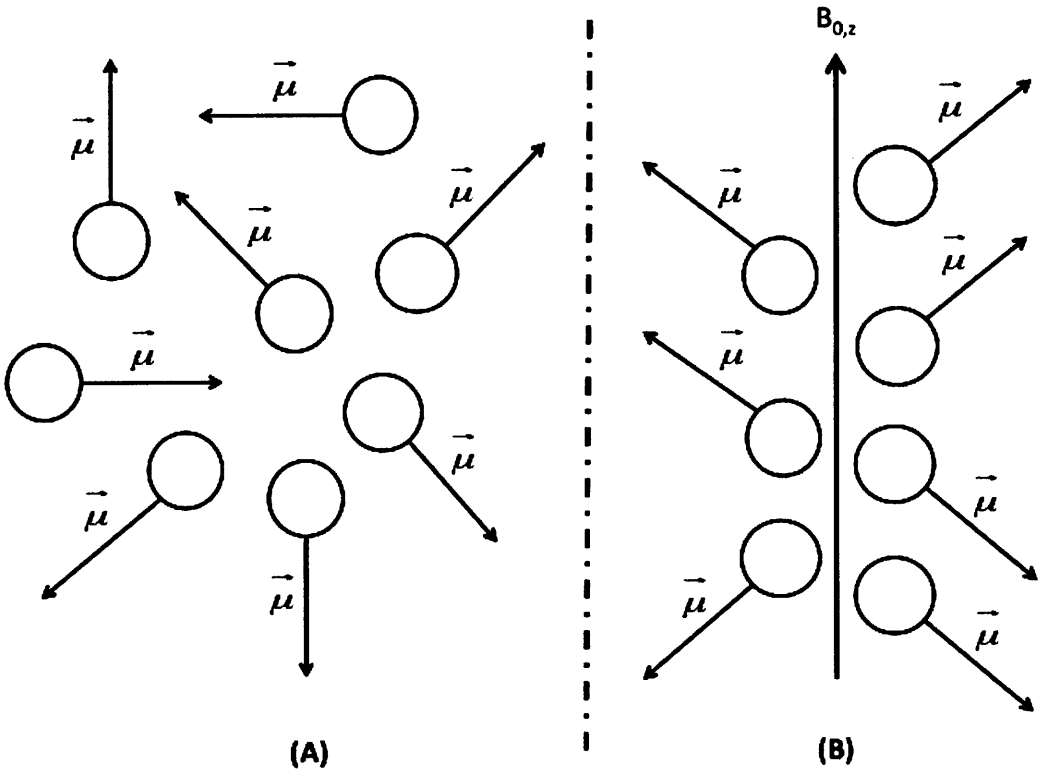

Figure 2-1 Magnetic moment vectors $\vec{\mu}$: (A) randomly oriented, and (B) pointing aligned in the direction of the external magnetic field B_0, either pointing parallel or anti-parallel (for ^1H). As seen, the transverse components of the spin vectors are still randomly oriented in the presence of the external magnetic field B_0, leading to a zero net magnetization in the XY plane.

Spins in different orientations have different energies of interaction with the external magnetic field B_0:

$$E = -\vec{\mu}.\vec{B}_0 = -\mu_z B_0 = -\gamma\bar{h}m_I B_0 \tag{2}$$

Hence, for parallel and anti-parallel spins (for ^1H) we have, respectively:

$$E_\uparrow = -\frac{1}{2}\gamma\bar{h}B_0 \tag{3}$$

$$E_\downarrow = \frac{1}{2}\gamma\bar{h}B_0 \tag{4}$$

As is understood from Eqs. (3) and (4), the spin-up state is the lower energy state. Fortunately, due to this energy difference between the spin states ($\Delta E = \gamma\bar{h}B_0$), known as the Zeeman splitting phenomenon, slightly more protons will point up than point down. According to the Boltzmann relationship we have:

$$\frac{N_\uparrow}{N_\downarrow} = e^{(\frac{\Delta E}{kT_s})} \approx 1 + \frac{\Delta E}{kT_s} \qquad ;\Delta E \ll kT_s \tag{5}$$

where $N_\uparrow$ is the number of spin up spins, $N_\downarrow$ is the number of spin down spins, k is the Boltzmann constant $1.38*10^{-23}$ J/K, and T_s is the absolute temperature of the spin system.

This excess of nuclei pointing up leads to the generation of an observable bulk magnetization M_z^0 pointing along the direction of B_0. This bulk magnetization is the source of the MRI signal. For a given half-spin system ($I = 1/2$), as indicated by Eq. (6) below, one can increase the magnitude of the bulk magnetization M_z^0 by either increasing B_0 or decreasing the temperature.

$$M_z^0 = \frac{\gamma^2 \bar{h}^2 B_0 N_s}{4kT_s} \tag{6}$$

where N_S is the total number of spins.

2.3.2 Larmor frequency

Spin vectors, while placed in an external magnetic field, experience a torque forcing them to precess clock wisely about the Z-axis, if observed against the direction of the magnetic field. The angular frequency of this precession can be described by Eq. (7), which is known as the Larmor frequency. This equation simply shows that the precession frequency of a spin system is linearly dependent on the strength of magnetic field B_0, and the gyromagnetic ratio γ.

$$\omega_0 = \gamma . B_0 = 2\pi f_0 \tag{7}$$

2.3.3 RF excitation

The bulk magnetization is rotated to the transverse plane using a RF pulse. This RF pulse, an envelope filled with a short-lived oscillating B_1 field perpendicular to the B_0 field, tips away the magnetization from the Z-axis to the XY plane (forced excitation), creating a measurable transverse component. The angle created between the Z-axis and the bulk magnetization is referred to as the flip angle α. The desired flip angle can be obtained by either adjusting the oscillating magnetic field strength B_1 or the RF pulse length τ_p (in case of a rectangular pulse we have $\alpha = \gamma B_1 \tau_p$). To obtain a perfect rotation, the resonance frequency of the RF pulse must match that of the spin system. This phenomenon is referred to as the on-resonance condition:

$$E_{rf} = \Delta E = \gamma \omega_{rf} \tag{8}$$

$$\omega_{rf} = \omega_0 \tag{9}$$

where E_{rf} and ω_{rf} are the radiation energy and resonance frequency of the RF pulse, respectively.

2.3.4 Free precession and relaxation

Once displaced from its thermal equilibrium state, the spin system returns to its lower state, after the B_1 field is removed and sufficient time elapses. This process is characterized by the free precession of the magnetization about the Z-axis, recovery of

the longitudinal component of the bulk magnetization (called T_1, longitudinal, or spin-lattice relaxation), and decay of the transverse component of the magnetization (called T_2, transverse, or spin-spin relaxation).

T_1 and T_2 relaxation processes occur due to the energy exchange between the spins and surrounding molecules, and interaction among spins, respectively. An important point about the T_1 and T_2 relaxation processes is that both follow an exponential function:

$$M_{xy}(t) = M_{xy}(0_+)e^{\frac{-t}{T_2}}e^{-i\omega_0 t} \tag{10}$$

$$M_z(t) = M_z(0_+)e^{\frac{-t}{T_1}} + M_z^0(1 - e^{\frac{-t}{T_1}}) \tag{11}$$

where $M_{xy}(0_+)$ and $M_z(0_+)$ are the magnetization in the transverse plane and along the Z-axis immediately after the RF pulse, respectively, and $e^{-i\omega_0 t}$ characterizes the free precession of spins, and its duration depends on T_2.

The exponential description, of course, is only valid for spins residing in liquid state molecules, especially for transverse relaxation. For solids and macromolecules, this mechanism is far more complicated. Note that T_1 and T_2 are not the times at which the longitudinal and transverse relaxations are completed. They are characteristic times that describe longitudinal and transverse relaxation of the spin system, respectively. One should also note that T_2 relaxation is irreversible, and always occurs at a rate faster than T_1.

2.3.5 Signal detection

The MR signal detection is, in fact, based on Faraday's law of induction and the principle of reciprocity. The time varying precession of the magnetization through the receiver coil (RF probe), according to Faraday's law, induces a voltage in the coil. This voltage signal is a high frequency signal, which can impose unnecessary problems on the receiving electronic circuits. Only the frequency offset $\Delta\omega = \omega_0 - \omega$ need be considered. As a result, the high frequency component of the voltage signal is removed through the signal demodulation method (i.e. removal of the carrier signal $e^{-i\omega_0 t}$). The signal demodulation consists of multiplying the voltage signal by a reference sinusoidal signal, and then low pass filtering. To detect the direction of rotation, a second demodulation is employed by a sinusoidal signal perpendicular to the first one. This technique is called quadrature detection, which is accomplished with two "detectors" orthogonal to each other. Quadrature detection also improves the signal to noise (SNR) ratio by a factor of the square root of 2. Finally, the demodulated signal is detected as a function of time, and, then, is converted to a frequency distribution by means of a Fourier transformation.

The acquisition of a signal can be repeated multiple times in order to improve the SNR. In performing this repeated signal acquisition, it is possible to vary the phase of the RF pulses and receiver for the removal of some MR artefacts. This process is known as phase cycling.

In practice, the MR signal is digitally sampled at a given interval, known as the dwell time DW, which corresponds to the frequencies sampled over a window, referred to as the spectral width of 1/DW.

2.4 Signal characteristics

In the previous sections, the activation process of the MR signal was explained briefly. In this section, we examine in detail basic MR time signals observed from a spin system after the pulse excitation. These signals are the basis for many sophisticated MR pulse sequences (see section 2.6). For each signal, we describe its excitation requirements and general characteristics.

2.4.1 Free induction decay signal

Free induction decay signal (FID), the simplest form of an MR time signal, is observed after the action of a single RF pulse on a spin system. "Free" refers to the fact that the free precession of the magnetization about the axis of the static magnetic field generates the signal, "induction" refers to Faraday's law of induction, and "decay" indicates that the signal's amplitude decreases over time.

The maximum amplitude of the FID signal occurs at time zero, and depends on both the flip angle α and the value of the bulk magnetization at thermal equilibrium M_z^0 (in the case of a single spectral component, $S(t) \propto M_z^0 \sin\alpha\, e^{\frac{-t}{T_2}}$). The decay rate of the FID signal is strongly dependent on the homogeneity of the magnetic field within the sample. In the case of a single spectral component, the decay rate of the FID signal is governed by T_2, but, in the presence of field inhomogeneity, a new time constant T_2^* describes the decay of the FID signal:

$$\frac{1}{T_2^*} = \frac{1}{T_2} + \gamma \Delta B_0 \tag{12}$$

where γ is the gyromagnetic ratio, and ΔB_0 is the Full Width at Half Maximum (FWHM, also referred to as linewidth) of the Lorentzian field distribution function. This equation is valid only for Lorentzian field distributions. The T_2^* time constant can be approximated from the frequency domain linewidth of an FID signal:

$$\text{FWHM} = \frac{1}{\pi T_2^*} \tag{13}$$

2.4.2 Spin echo

Spin echo (SE), another form of MR signal known as RF echoes, is a gold standard for many MR pulse sequences. It is a two-sided symmetrical signal that consists of two mirrored FIDs, each side of which carries a T_2^* decay. However, the amplitude of the SE signal is controlled by the T_2 time constant, making it a suitable method for T_2 measurement in the absence of any spin mobility. The symmetry of the SE signal is also useful for the symmetrical coverage of k-space (see 2.5.1), removing the probe dead time problem in contrast to the FID signal.

To generate a SE signal, first, a 90° RF pulse is applied to the spin system to create a transverse component of the bulk magnetization. It is then followed by a delay time of τ_{180}, during which spins with different Larmor frequencies precess about the Z-axis losing their phase coherence. A 180° pulse is then required to reverse dephasing due to the field

offsets. Provided another delay time of τ_{180} is allowed to pass, all spins will recover a phase coherence at time $t_E=2\tau_{180}$, referred to as echo time. One can also replace the refocusing pulse by a composite pulse for more uniform excitation. Pulses other than 90°-180° can also be used to create echoes (sometimes referred to Hahn echoes), however, this combination creates the maximum possible echo signal.

2.4.3 Carr-Purcell-Meiboom-Gill

In the presence of molecular self-diffusion D and B_0 field inhomogeneity (background gradient G_i), the amplitude of the SE signal is not only a function of T_2, but also proportional to the cube of τ_{180} ($\propto \exp\left(-\left(\frac{t_E}{T_2}+\frac{2}{3}\tau_{180}^3\gamma^2G_i^2D\right)\right)$) [6]. This makes the Hahn SE unsuitable for the measurement of the MR T_2 relaxation time. Firstly, we must repeat the basic experiment many times by systematically increasing the echo time from experiment to experiment, and secondly, we need to remove the attenuation effect of the molecular self-diffusion D to be able to extract T_2.

One can, however, employ the Carr-Purcell-Meiboom Gill (CPMG) pulse sequence to diminish the molecular self-diffusion D effects. This pulse sequence is another form of RF echoes, which is derived from the Hahn SE sequence. As shown in figure 2-2, typically a train of 180° pulses are applied following a 90° RF pulse to refocus the B_0 inhomogeneity spin dephasing and form multiple echoes. In the actual implementation of the CPMG pulse sequence, usually, only the peak of each echo is collected, and, then, T_2 is extracted by fitting the acquired data points to an exponential decay. Typically a large

number of echoes are acquired, which is directly dependent on the object's signal lifetime.

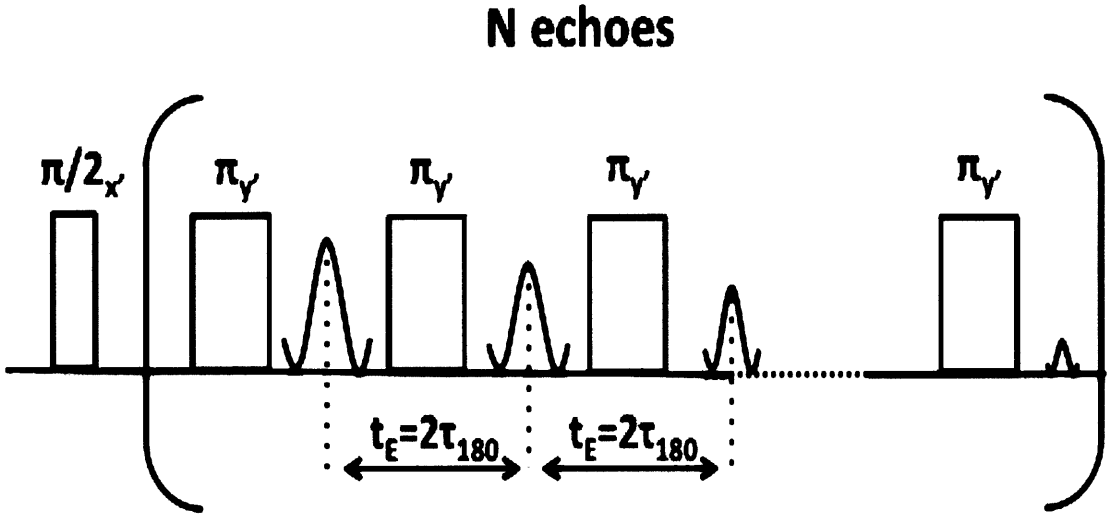

Figure 2-2 The Carr-Purcell-Meiboom-Gill pulse sequence: A 90° RF pulse is followed by a train of 180° pulses to form multiple echoes by continuously refocusing the frequency offsets. The number of echoes, which can be generated, is limited by the T_2 of the sample. By maintaining a short time interval $2\tau_{180}$ between pulses and employing more refocusing pulses, one can minimize the attenuation effect of diffusion. The 90° phase difference between the excitation pulse and the following refocusing pulses corrects for any 180° pulse length error due to the B_1 field inhomogeneity for every second echo.

The 90° phase difference between the excitation pulse and the following refocusing pulses ensures the self-correction for any refocusing pulse length error in alternate echoes [7]. By making the time interval between pulses small, and employing more 180° pulses, the diffusion effect on the echo amplitude can be minimized.

2.4.4 Pulsed magnetic field gradient spin echo

PFGSE pulse sequence is similar to the SE pulse sequence, with the exception of the addition of a pair of displacement encoding gradients. These gradients are applied on either side of the refocusing RF pulse with duration δ, amplitude G_d, and separation Δ to encode the diffusion (figure 2-3) in the direction of the gradient.

Static spins are not affected by these gradients as the phase they accumulate during the first gradient at their respective position is removed after the 180° pulse and second gradient. Diffusing spins, however, do not have the same position when the second gradient is applied, and they accumulate a phase based on the distance they travelled during the separation time Δ (i.e. $\emptyset = \gamma G_d \delta(\Delta r)$). Because a wide range of Δr displacements are possible due to the spins' random motion (i.e. molecular diffusion), at the echo time, spins are stochastically out of phase leading to the cancelation of the signal, by both normal T_2 process and diffusion. The ratio of the echo amplitudes can be described by Eq. (14) [8]:

$$\frac{S(G_d)}{S(0)} = \exp(-bD) \qquad ; b = \gamma^2 G_d^2 \delta^2 (\Delta - \frac{\delta}{3}) \tag{14}$$

where S(G) is the echo amplitude in the presence of diffusion gradients, and S(0) is the echo amplitude without any diffusion gradient.

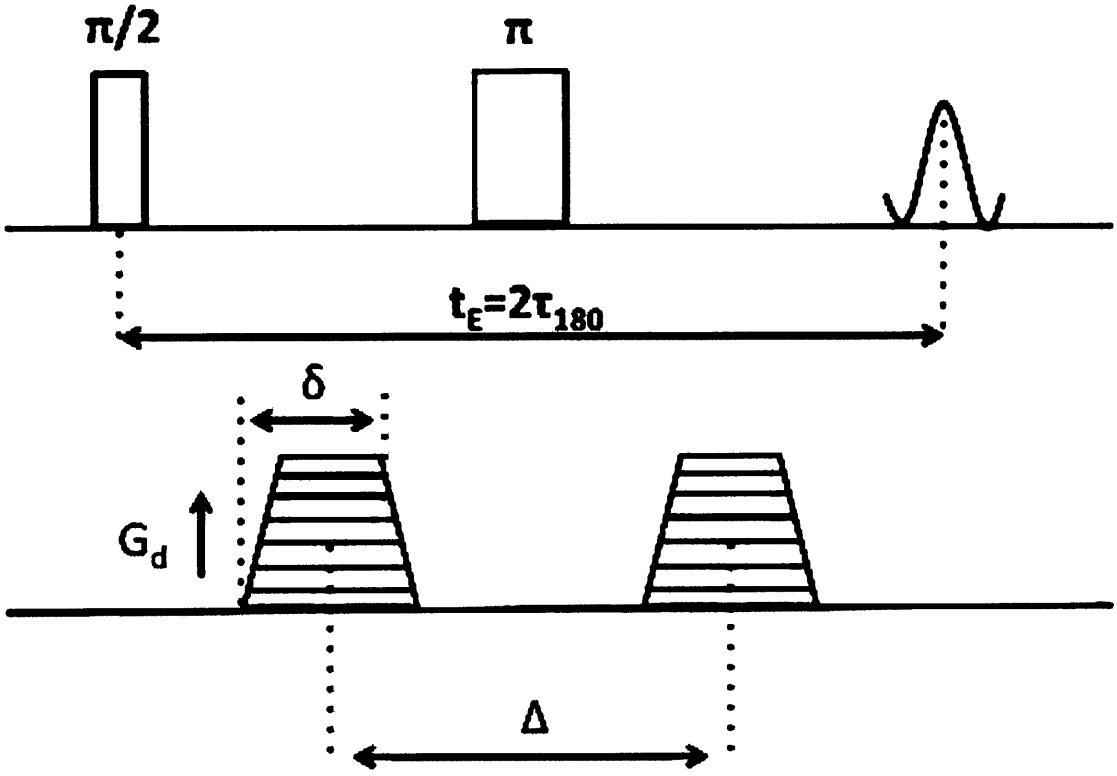

Figure 2-3 The pulsed field gradient spin echo pulse sequence: Similar to the SE pulse sequence with the addition of a pair of displacement encoding gradients in the direction of interest. The gradients are employed to encode the molecular self-diffusion in the system. In practice, the experiment is performed with different values of the diffusion gradients, and, then, diffusion is calculated from the slope of the $\ln(S(G_d)/S(0))$ vs. b-factor curve.

By systematically changing G_d, δ, Δ, and plotting $\ln(S(G_d)/S(0))$ vs. b-factor, the diffusion of the sample can be extracted from the slope of the curve. In practice, usually, the experiment is repeated for several different values of G_d, while keeping δ and Δ constant. This pulse sequence is not suitable for samples with short T_2 and slow diffusion, as minimal phase accumulation may be obtained in reasonable Δ time.

One can also employ the PFGSE pulse sequence for the study of coherent flows [9]. In this case, the flow displacement and velocity information is extracted from the phase shift ($\emptyset = \gamma G_d \delta(\Delta r) = \gamma G_d V \delta \Delta$), which is introduced to the spin system due to spins' coherent Δr displacement. Practically, the difference between two measurements is considered with an increment in the velocity-encoding gradient. In this way, the phase shift accrued due to any background gradient is also removed.

Spatial encoding gradients can also be incorporated in 2 or 3 spatial directions for multi-dimensional diffusion/velocity weighted imaging.

2.5 Signal localization

The generated signal, in fact, is a sum of local signals from all parts of the sample, referred to as the bulk signal. For a spatially homogenous sample, the local signals are the same, and as a result, no signal localization is required. However, most samples are heterogeneous, and this makes the signal localization necessary.

Signal localization, which is accomplished with the help of the magnetic field gradient system, is basically of two types: selective excitation and spatial encoding. Slice selective

excitation is not covered here, as it is irrelevant to the subsequent chapters. The basic concepts of the spatial encoding, however, will be covered through the k-space concept.

2.5.1 K-space

K-space is a mathematical domain where the acquired MR image signal is stored as digitized data. In fact, the k-space formalism establishes a mathematical connection between the spatial encoding and the Fourier transform [10]; the MR image is reconstructed from k-space by inverse Fourier transformation. As k-space is the reciprocal of image space, the field of view (FOV) of an MR image is determined by the spacing between adjacent points in k-space ($FOV = 1/\Delta k$). The image nominal resolution, on the other hand, is determined by the width of the k-space sampled ($\delta = 1/2k_{max}$). To meet the Nyquist-Shannon sampling theorem and avoid aliasing (i.e. also known as "fold over" artifact; misregistration of the signal outside of the FOV to the opposite side of the image), the FOV must be equal to or larger than the object being imaged. The center of k-space stores low frequency information determining the contrast and gross structure, while the image fine details are determined by the high spatial frequency data, which is mapped to the outer peripheral regions of k-space. For noise reduction, low pass filters (e.g. an exponential filter) may be employed, as noise is a high spatial frequency low amplitude component. The filtering is usually performed in the k-space domain by a multiplication with the filter function. As in other imaging applications, a line broadening without decreasing the image resolution is needed, the rule of thumb is to not perform a convolution with a function broader than the image pixel size.

The reciprocal space vector, k, is defined as:

$$k = \frac{1}{2\pi}\gamma G t \tag{15}$$

In accordance to Eq. (15), the two parameters, which may be varied for the navigation of k-space, are the gradient G or time t. In fact, the location of the data in k-space depends on the net strength and duration of the phase and frequency encoding gradients; a low-amplitude or short-duration gradient event encodes low-spatial-frequency information, and vice versa. Usually, a mixture of frequency and phase encoding is employed to fully sample k-space; each method encoding perpendicular directions. Frequency encoding makes the resonance frequency of the local signal linearly dependent on its spatial origin ($\omega = \omega_0 + \gamma G_f . x$). This is done by the application of a fixed gradient G_f in direction X for a varying time of t_{acq} (i.e. acquisition time, number of sampled points multiplied by DW). For phase encoding, a known gradient G_p is turned on in direction Y for a fixed short time interval of t_p, determined by the pulse sequence. During this time interval, local signals accumulate a phase angle ($-\gamma G_p . y . t_p$) according to their spatial location. In the most basic sampling strategy (i.e. rectilinear sampling), k-space is filled line-by-line. Each line is sampled at each excitation during the frequency encoding. Between each repetition, the phase encoding gradient is incremented to move the sampled data to the next line in k-space in the k_y direction. The change in the phase encoding gradient is constant between adjacent lines, and this results in a sequential line-by-line filling of k-

space from top to bottom. For 3D imaging, an additional phase encoding gradient is applied in the 3rd direction.

Although, conventionally, a mixture of frequency and phase encoding is employed to sample k-space, in the case of samples with short T_2 or T_2^*, pure phase encode imaging methods may be employed to acquire the signal before it substantially decays. In this scheme, k-space is traversed point-by-point rather than line-by-line, and consequently, it may be time consuming resulting in low measurement sensitivity. Pure phase encode methods, however, have certain advantages over conventional schemes [11,12]. They are immune to time-evolution artifacts because they freeze the time (i.e. the phase error due to the off-resonance effects is the same for all k-space points), whilst conventional methods are prone to artifacts due to B_0 inhomogeneity, chemical shift, and susceptibility variations. Conventional sampling methods are also limited by the linewidth restriction on resolution (blurring) due to the signal evolution during encoding (i.e. the data acquisition window must be narrow compared to the signal lifetime).

2.6 More advanced MR pulse sequences

In this section we introduce more advanced MR pulse sequences, which are relevant to the subsequent chapters. These pulse sequences will be employed in Chapters 3 and 4.

2.6.1 3D conical single point ramped imaging with T_1 enhancement

The 3D conical SPRITE pulse sequence (figure 2-4), a further development of the SPRITE sequence [12], is composed of a train of short broadband (non selective) RF

pulses separated by the repetition time TR [13]. Two imaging gradients are sinusoidally ramped while the third one is linearly ramped through a discrete number of gradient amplitudes for each cone (phase encoding in all 3 directions). In practice, 39 cones are employed to sample k-space. As RF pulses are applied in the presence of spatial encoding gradients, to achieve a homogeneous excitation, the duration of RF pulses must be short enough that their bandwidth covers the range of frequencies introduced by the magnetic field gradients. A single point from each resultant FID is acquired following a phase encoding time t_p. Although not enough time is permitted for the recovery of the longitudinal magnetization between RF pulses, there is no longitudinal magnetization saturation of the central k-space point, as the data acquisition commences from the k-space origin proceeding to the extremes. Consequently, the MR signal at the k-space origin has the form of that of a FID, making conical SPRITE suitable for 3D spin density and T_2^* mapping.

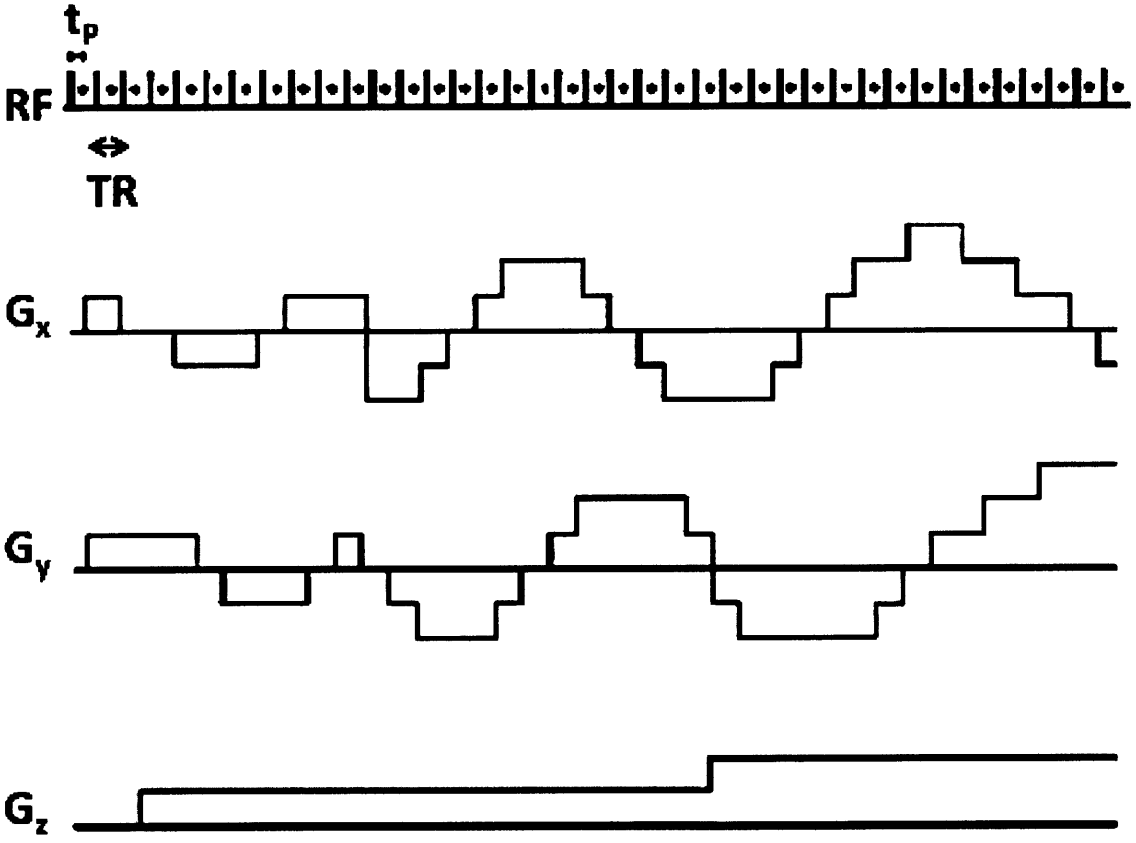

Figure 2-4 3D pure phase encode conical single point ramped imaging with T_1 enhancement: only a few first points of a single cone are illustrated while, in practice, 39 cones are implemented for k-space sampling.

With the superposition of motion sensitizing gradients in the encoding interval in the desired spatial direction, this pulse sequence can be also made sensitive to motion [14]. Having all the benefits of the standard 3D conical SPRITE, the motion-sensitized version scheme is appropriate for the measurement of fast flows with short T_2^*. Because the characteristic measurement time t_p can be made sufficiently short, fluid displacement in the encoding interval lies within the image pixel resolution (i.e. no ghosting effect or signal cancellation in the case of turbulent flow). The method, however, has intrinsic temporal averaging of the data as the acquisition of a 3D image takes at least several minutes.

2.6.2 3D motion sensitized single point imaging spin echo

The 3D motion sensitized SE-SPI, as the name indicates, is a 3D pure phase encode pulse sequence that may be employed to obtain spatially resolved diffusion maps [15]. This pulse sequence, as shown in figure 2-5, is very similar to the standard PFGSE sequence with the exception of phase encoding gradients added in 3 spatial directions. At each excitation, the echo amplitude is acquired to fill a single k-space data point. The whole measurement is repeated for several different values of the diffusion-encoding gradients, referred to as q-values, to generate the 3D diffusion weighted map. Compared to the conventional 3D PFGSE in which frequency-phase encoding imaging gradients are employed, using only phase encoding imaging gradients in the 3D motion sensitized SE-SPI permits incorporating shorter echo times t_E, making it appropriate to the study of heterogeneous materials with natural broad line widths. It also provides better image resolution compared to the standard PFGSE. The method, however, suffers from very

long total measurement time, as other pure phase encode techniques. This drawback, however, may be overcome through the employment of reduced k-space sampling strategies (see 4.3.2) [16,17].

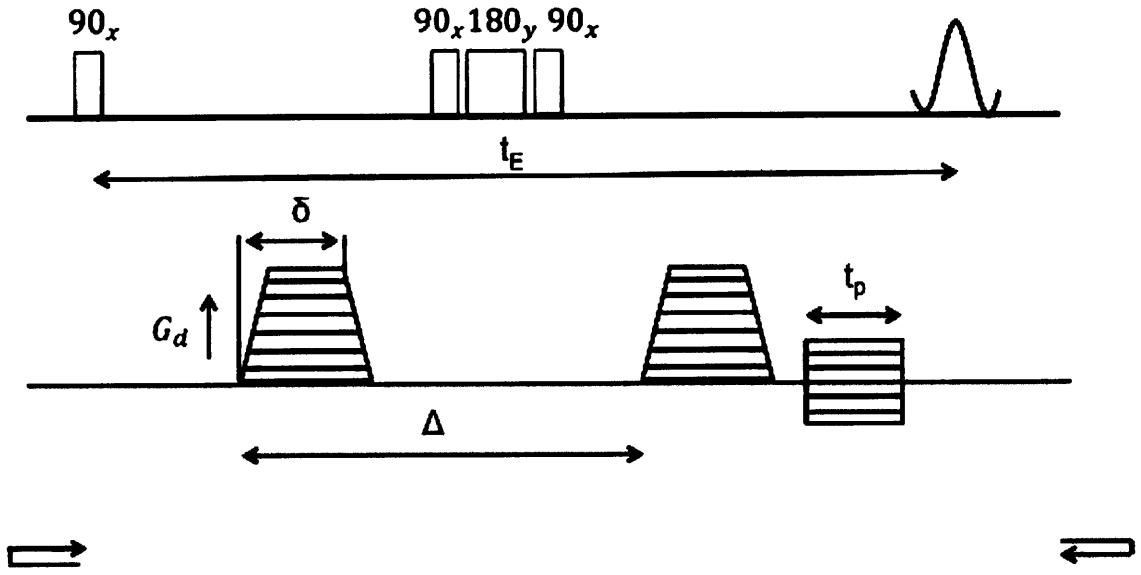

Figure 2-5 3D motion sensitized pure phase encode single point imaging spin echo: A composite refocusing hard excitation pulse can be incorporated for more accurate excitation, as illustrated. Only phase encoding in one direction is shown.

2.7 Magnetic susceptibility

When a material is exposed to a magnetic field B_0, a magnetization M_z^0 is induced in the material, which is related to B_0 through $M_z^0 = \kappa B_0$, where κ is called the volume susceptibility. Since B_0 and M_z have the same dimensions, κ is dimensionless in the CGS system [18]. To obtain the value of dimensionless SI volume susceptibility χ, one multiplies the dimensionless CGS value of volume susceptibility κ by 4π.

Another parameter defined from the volume susceptibility κ is referred to as the molar susceptibility χ_m:

$$\chi_m = \kappa \frac{M}{\rho} \tag{16}$$

where M is the molar mass and ρ is the mass density.

Substances may have negative or positive susceptibility values. Those with no unpaired electrons have negative molar susceptibility χ_m, and are termed diamagnetic. Substances with unpaired electrons have positive molar susceptibility χ_m, are named paramagnetic, and show a stronger dependence on temperature ($\propto 1/T$) compared to diamagnetic materials.

2.8 References

[1] C.P. Slichter, "Principles of magnetic resonance", Third enlarged and updated edition, Springer-Verlag, New York, 1996.

[2] P.T. Callaghan, "Principles of nuclear magnetic resonance microscopy", Oxford University Press, Oxford, 1991.

[3] M.A. Bernstein, K.F. King, X.J. Zhou, "Handbook of MRI pulse sequences", Elsevier Academic Press, Burlington, MA, USA 2004.

[4] D.G. Nishimura, "Principles of magnetic resonance imaging", Publisher: Author, 2010.

[5] Z.Liang, P.C. Lauterbur, "Principles of magnetic resonance imaging: a signal processing perspective", IEEE Press, New York, 2000.

[6] J.W. Hennel and J. Klinowski, "Fundamentals of nuclear magnetic resonance", Harlow, Essex, United Kingdom: Longman Scientific & Technical, 1993.

[7] M.H. Levitt, and R. Freeman, "Compensation for pulse imperfections in nmr spin echo experiments", Journal of Magnetic Resonance, 1981, 43, 65-80.

[8] E.O. Stejskal, "Use of spin echoes in a pulsed magnetic field gradient to study anisotropic, restricted diffusion and flow", Journal Chemical Physics, 1965, 43, 3597-3603.

[9] M.D. Mantle, A.J. Sederman, "Dynamic MRI in chemical process and reaction engineering", Progress in Nuclear Magnetic Resonance Spectrsocopy, 2003, 43, 3-60.

[10] A. B. Tayler, "Experimental characterization of bubbly flow using MRI", A Thesis submitted for the degree of Doctor of Philosophy, Trinity College, 2011.

[11] A.E. Marble, I.V. Mastikhin, R.P. MacGregor, M. Akl, G. LaPlante, B.G. Colpitts, P. Lee-Sullivan, B.J. Balcom, "Distortion free single point imaging of multi-layered composite sandwich panel structures", Journal of Magnetic Resonance, 2004, 168, 164-174.

[12] B.J. Balcom, R.P. Macgregor, S.D. Beyea, D.P. Green, R.L. Armstrong, and T.W. Bremner, "Single-Point Ramped Imaging with T1 Enhancement (SPRITE)", Journal of Magnetic Resonance, 1996, 123, 131–134.

[13] M. Halse, D. Goodyear, B. MacMillan, P. Szomolanyi, D. Matheson, B. Balcom, "Centric scan sprite magnetic resonance imaging", Journal of Magnetic Resonance, 2003, 165(2), 219–229.

[14] Newling B, Poirier C, Zhi Y, Rioux J, Coristine A, Roach D, Balcom B, "Velocity imaging of highly turbulent gas flow", Physical Review Letters, 2004, 93(15), 154503.

[15] Li L, Han H, Balcom B, "Spin echo spi methods for quantitative analysis of fluids in porous media", Journal of Magnetic Resonance, 2009, 198(2), 252–260.

[16] D. Xiao, B. J. Balcom, "Two-dimensional T_2 distribution mapping in rock core plugs with optimal k-space sampling", Journal of Magnetic Resonance, 2012, 220, 70-78.

[17] A. Arbabi and I.V. Mastikhin, "Magnetic susceptibility based magnetic resonance estimation of micro-bubble size for the vertically upward bubbly flow", Journal of Magnetic Resonance, 2012, 225, 36–45.

[18] W.M. Haynes, "Handbook of chemistry and physics", 93rd edition, CRC press, 2012.

3 - Magnetic resonance imaging of velocity fields and the void fraction in a cavitating liquid

3.1 Introduction

In acoustic cavitation, the relationship between bubble dynamics on the micro-scale and flow properties on the macro-scale is critical in determining sonochemical reaction kinetics. In an acoustically cavitated liquid, cavitating bubbles are not stable. They change in size following the oscillations of the acoustic field, grow, move, coalesce, and eventually collapse. The motion of nuclear spins of the liquid in the changing magnetic field gradients near the bubbles will result in a complicated modulation of the MR relaxation by the average bubble size and dynamics. It can be shown that, depending on the characteristic measurement time and the mobility of the water near spherical bubbles, the MR relaxation will exhibit either mono-exponential (''fast diffusion regime'') or a non-exponential behavior (''slow diffusion regime'').

Moreover, if only the information on the void fraction is of interest, the void fraction estimate can be obtained by measuring the MR signal decay of spins of the liquid (water here) and extrapolating it to extract the spin density of the liquid, which will be proportional to the liquid density minus the bubble void fraction. This information can be used to estimate the compressibility of the cavitating liquid, and its influence on the macroscopic velocity field.

In this chapter, we applied a new method based on 3D pure phase encode MRI technique with short characteristic measurement times t_p (0.1–2 ms), which allowed us to

estimate the upper limits for mixing by microstreaming, and obtain information on the bubble void fraction. We also measured the 3D velocity fields in the cavitating fluid using a pure phase encode motion sensitized MRI method on a characteristic timescale of 1 ms (3.5 min to acquire a 3D dataset). The relationship between the void fraction and the liquid compressibility was investigated. The exponential behavior of the MR signal decay indicated the fast diffusion regime, with the relationship between local mechanical dispersion D and the average bubble radius R, $D \gg 2R^2/10^{-4}$ s, resulting in dispersion orders of magnitude greater than diffusion in quiescent water. In two different samples, distinguished by the presence or absence of surfactant, we showed how different interactions between the bubbles and the liquid result in a different void fraction, velocity, divergence, and vorticity of the medium.

In inhomogeneous media, such as a strongly cavitating liquid, the magnetic field variation between the gas inside the bubbles and the surrounding water will produce distortions in conventional MRI methods as a consequence of the abrupt changes in magnetic susceptibility at the gas–liquid boundaries. Collection of quantitative data may be impossible. One can, however, use the susceptibility effects to one's advantage, if the sensitivity of the MRI technique to such distortions is controllable. All types of MRI measurements were phase-encoded techniques, and, as a result, immune to the image distortions produced by the susceptibility differences in cavitating samples, enabling the quantitative characterization of spin density.

3.2 Experimental

Two samples with different bubble dynamics [1,2], water and water with the addition of 1 mM of surfactant (sodium dodecyl sulfate [SDS]), were used. The experimental setup is shown in figure 3-1. All MRI measurements were performed on a horizontal bore superconducting 2.4 T magnet (Nalorac, Martinex) with the Apollo console (Tecmag, TX). A magnetostrictive ultrasonic transducer (19.1 kHz, Industrial Sonomechanics, NY) with a 1.7 cm-diameter sapphire horn was immersed in a 12 cm-long cylindrical plastic cuvette (i.d. of 3 cm) with the solution. The cuvette was placed along the direction of the main magnetic field. The distance between the horn tip and the cuvette front wall was 1.9 cm (1/4 wavelength). Imaging experiments were performed during cavitation with an acoustic output corresponding to an acoustic pressure of 5.7 Atm (measured in double-degassed water by a microphone in the front wall), with the horn tip velocity amplitude of 0.46 m/s, as measured by a KD-300 Fotonic Sensor (MTI Instruments, NY). The distilled water was doped with 5 mM of $MnSO_4$ to reduce the ^1H MR relaxation time.

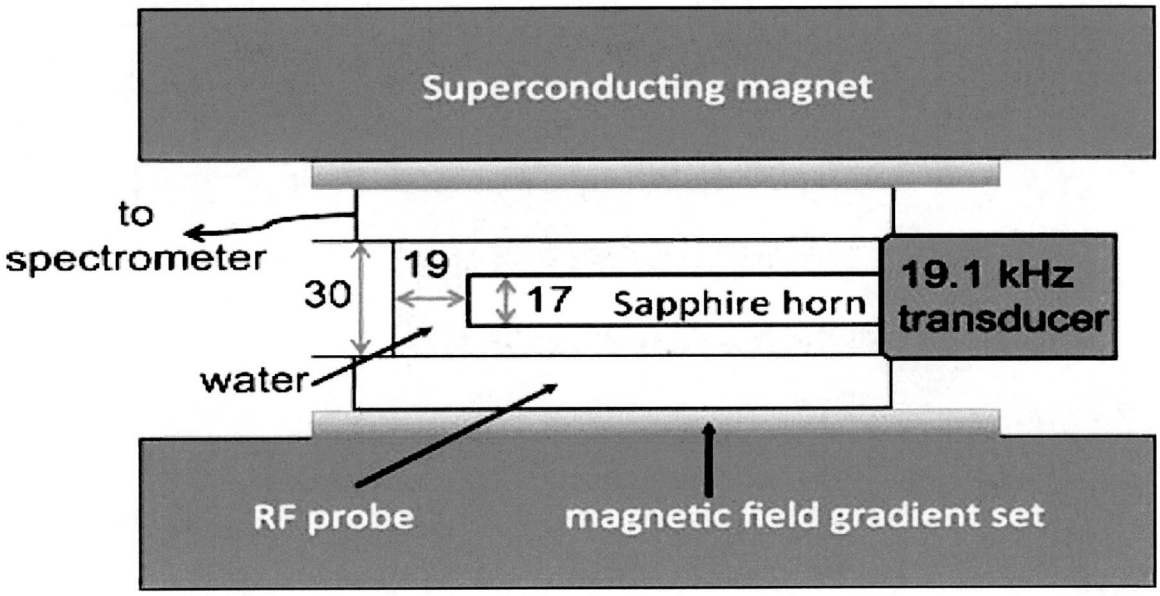

Figure 3-1 Experimental setup. All distances are in mm.

Spin density measurements employed the 3D conical SPRITE sequence with 8 encoding times t_p from 0.1 to 2 ms (two averages, 7 min acquisition time per step). For the sake of visualization, regions with void fraction greater than 30% were removed from the maps: They corresponded to a well-localized area at the top of the cuvette where a (several pixel wide) gaseous cavity formed as the result of degassing. The MRI measurements of a cavitating sample alternated with measurements of a stationary sample to acquire template data for phase correction to account for eddy currents induced by gradient switching, for both the spin density and velocity measurements.

For the velocity measurements, a motion sensitized 3D conical SPRITE was used (see also 2.6.1) with the motion encoding gradient pulses of duration δ equal to the displacement interval $\Delta=\delta=0.5$ ms and 9 velocity-encoding steps (3.5 min acquisition time per step), zero filled to 32 steps in postprocessing. The velocity encoding was performed in X, Y, and Z directions, Z being by convention the direction of the main magnetic field and opposite to the horn's orientation. Nominal spatial resolution was 0.9 mm in X and Y and 1.25 mm in Z for all 64^3 datasets.

In case of a displacement in the phase encoding direction during the encoding time t_p, with the encoding gradient waveform not velocity compensated, there will be a signal phase shift leading to a misregistration (''ghosting'') in the image located at $x = v*t_p$. This was potentially an issue in our spin density measurements. To investigate the potential range of velocities present in the system, preliminary velocity measurements were performed prior to the series of spin density experiments. It was found that the measured velocities did not exceed 0.5 m/s in Z direction, and were lower in the other directions. For the range of employed encoding times, the resulting misregistration would

be on the order of 0.05-1 mm. With the employed image resolution, therefore, the expected ghosting was less than the pixel size for the longest encoding time of 2 ms, and much smaller for other encoding times.

3.3 Results and discussion

3.3.1 Void fraction measurements

Magnetic susceptibility is a measure of magnetization of a material placed in a magnetic field that either increases or decreases the magnetic field in the material. If an external magnetic field is applied to two materials with different susceptibilities, such as water and an air bubble, the magnetic field inside the bubble will be different from that in water, by about 9.4 ppm. At the boundary, the magnetic field will change from one value to the other, thus generating a magnetic field gradient, which extends to proximity. The susceptibility difference can be quantified by MRI directly for macroscopic objects, if the imaging resolution is greater than the transition region, or, for microscopic objects, indirectly via changes in MR relaxation times.

Changes in magnetic susceptibility at the boundaries of water containing pores in porous media have long been known to reduce MR relaxation times of the water due to the diffusion of the nuclear spins in the induced magnetic field gradients [3]. MR relaxation time measurements are used to measure pore size distribution and other properties of porous materials [4]. Here, we apply a similar approach by treating the cavitating liquid as a transiently porous material.

The signal intensity in a centric SPRITE sequence is that of the FID: $S(t) = S(0)e^{\left(\frac{-t_p}{T_2^*}\right)}$ [5]. Without diffusion, the local susceptibility changes $\Delta\chi$ produced by the bubbles will reduce the T_2^* relaxation time to:

$$\frac{1}{T_2^*} = \frac{1}{T_2} + \gamma\Delta B(r), \qquad \Delta B(r) = C\Delta\chi B_0 \tag{1}$$

and C carries information on bubble size distribution, concentration and mobility. For stabilized spherical bubbles, an expression that takes into account the diffusion of spins D, the normalized void fraction φ, the average bubble radius R, and the characteristic measurement time t_p can be analytically derived (from [6], corrected):

$$\frac{1}{T_{2,new}^*} = \frac{1}{T_{2,B}^*} + \frac{16}{5}\cdot\frac{\varphi}{D^2 t_p}\cdot\left(\frac{1}{3}\gamma B_0\Delta\chi R^2\right)^2 \cdot\left[\exp\left(\frac{-Dt_p}{2R^2}\right) - 1 + \frac{Dt_p}{2R^2}\right] \tag{2}$$

As can be seen from the Eq. (2) (following the discussion in [6]), the duration of the measurement time t_p with respect to the average bubble radius, and the diffusion in the medium will result in two significantly different measurement regimes (Eqs. (3) and (4)): one where $t_p \gg 2R^2/D$, and the decay constant has no dependence on t_p (a purely mono-exponential decay), the other where $t_p \ll 2R^2/D$, and the decay constant varies with t_p. The magnetic field changes are significant at a distance from the bubble that is on the order of the bubble radius (essentially, in the bubble boundary layer). For the mono-

exponential decay, the measurement time t_p must be longer than the average diffusion time for the spins in the bubble-induced magnetic field gradients.

$$\frac{1}{T_{2,new}^*} = \frac{1}{T_{2,B}^*} + \frac{8}{5}.\varphi.\left(\frac{1}{3}\gamma B_0 \Delta\chi\right)^2.\frac{R^2}{D} \qquad \text{if } t_p \gg \frac{2R^2}{D} \tag{3}$$

$$\frac{1}{T_{2,new}^*} = \frac{1}{T_{2,B}^*} + \frac{2}{5}.\varphi.\left(\frac{1}{3}\gamma B_0 \Delta\chi\right)^2.t_p \qquad \text{if } t_p \ll \frac{2R^2}{D} \tag{4}$$

Our shortest measurement time, t_p=0.1 ms, is about two oscillation periods for the chosen ultrasound frequency. If the chosen measurement time range (0.1–2 ms) results throughout in mono-exponential decays, then the random motion of ^1H in H_2O caused by cavitation in the acoustic field is much faster than self-diffusion.

In our measurements, the mono-exponential fit was found to be satisfactory for both types of samples, with the adjusted R^2 of 0.97–0.99 almost everywhere (except pixel-wide regions bordering the outer walls of the cuvette, R^2=0.85–0.9), with the fitting uncertainty below 1.1%, thus pointing toward the fast motion regime. We can introduce a local mechanical dispersion coefficient D as an analog of the self-diffusion coefficient that will characterize the water motion in the boundary layer of the bubble. It should obey the following relation: $D \gg 2R^2/10^{-4}$ s.

The average bubble radius is difficult to estimate due to a variety of bubble sizes and short/long bubble lifetimes: The modulation of the MR signal by the susceptibility effects produced by all the bubbles inside each voxel is averaged over the course of the measurement, i.e., several minutes. We have chosen to use 1 μm size as a conservative

estimate. For that radius, the mechanical dispersion coefficient will be in excess of $2*10^{-8}$ m^2/s, an order of magnitude greater than the water diffusion coefficient. This is not a surprise as the water molecules next to the bubbles must move with the same speeds of those of the bubble boundaries.

This result agrees with many observations in the literature that the microstreaming of the liquid around the cavitating bubble is quite fast and is one of the main factors responsible for the active mixing of the liquid (see for example, [7]). Our measurement represents an independent technique for obtaining information about the local liquid motion around the cavitating bubbles.

Another, technical, consequence of the mono-exponential behavior of the MR signal is that it is straightforward to obtain an estimate of the bubble void fraction from the given measurements. Indeed, the information on the complicated motion of the liquid in the bubble-induced magnetic fields will be contained in the relaxation time parameter $1/T^*_{2,cav}$, while the void fraction information will be proportional to the spin density $S(0)_{Cav}$, which can be extracted after the mono-exponential fitting. Its subtraction from the spin density map $S(0)_{NonCav}$ obtained for the measurements of the quiescent water sample (no cavitation) will yield the normalized void fraction map.

The middle slices from 3D maps for the two samples shown in figure 3-2 demonstrate a much greater void fraction for water (A) than for the water/SDS mixture (B). This result is consistent with volumetric measurements in [8] wherein the total bubble volume was measured volumetrically, and the greatest drop in the bubble volume was found at 1 mM of SDS (the measurements, however, were performed at frequencies more than 10 times higher than in the present study). The highest void fraction is located near the center of

the horn for both samples. The measurement uncertainty is 1%, making the void fraction data about 10 times greater than the uncertainty for the water samples, and about 2–3 times greater than that for the samples with the SDS. The data represent not an instantaneous picture of the cavitating bubbles but the void fraction averaged over the measurement time (several minutes).

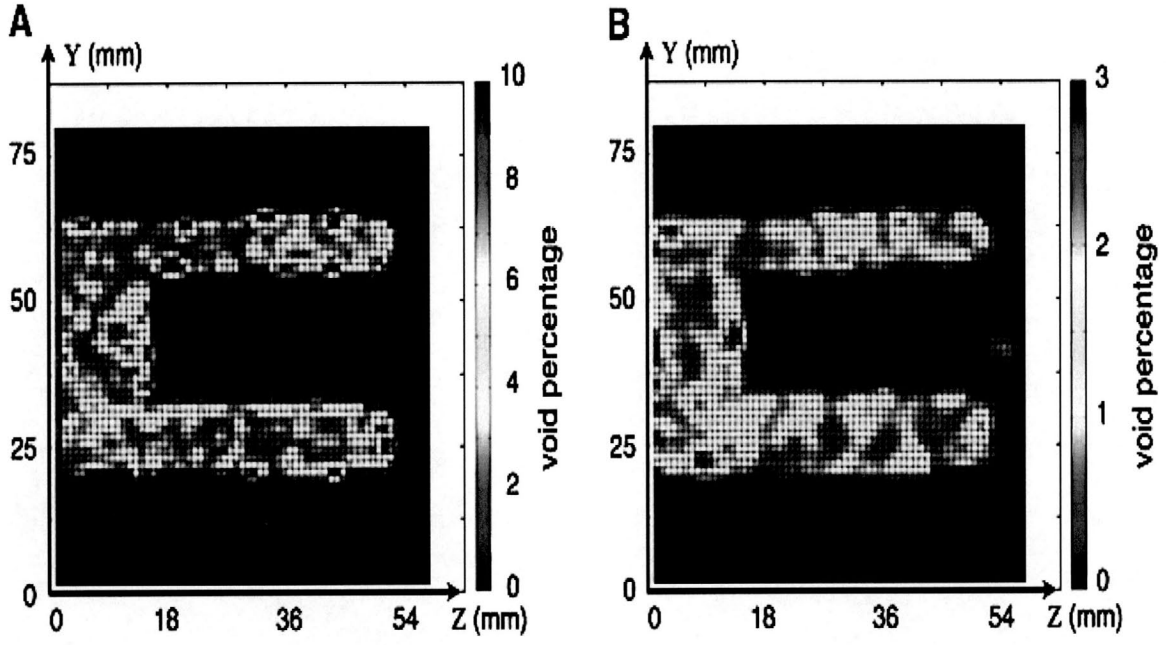

Figure 3-2 Middle slices from 3D void fraction maps for water (A) and SDS solution (B). The vertical direction corresponds to the Y (vertical) orientation in the magnet. The horizontal direction is the Z orientation, with the externally applied magnetic field, against the ultrasound direction. The color scale is in percent of the density and is different in (A) and (B).

The void fraction numbers obtained with the method presented are higher than the ones obtained with optical methods [9]. In that paper, the authors applied two different optical techniques, laser diffraction (LD) and phase Doppler (PD), to investigate the acoustic cavitation cloud. The void fraction values of 10^{-5}-10^{-4} were obtained with LD and $5*10^{-3}$-10^{-4} with PD as functions of acoustic output at 10 (LD) and 15 mm (PD) distance from the tip of the horn. The LD technique utilized a laser beam of 9 mm diameter intersecting with the cavitation cloud in the probe volume of length 100 mm and as such was a spatially averaging method. The PD technique counted bubbles passing through the intersection of two laser beams and was a local and time averaging method. The techniques required a great level of finesse to overcome experimental difficulties associated with several factors contributing to the light scattering and diffraction, and the authors acknowledge that ''some of these [bubbles] can be missed and this can have a great effect on void fraction.'' Due to technical limitations of the optical techniques, it was impossible to perform measurements in the regions closer than 10 mm from the tip of the horn.

At 10 mm from the horn, we measured the void fraction of $8*10^{-3}$ in water and $3*10^{-3}$ in SDS (averaged by the volume of the same size as for LD measurements in [9]). Here, we would like to point out the necessity of a reasonably high resolution for the MRI measurements: If there were no spatial encoding, and the signal from the whole cuvette would be measured, the variations in the spin density, and, in consequence, the void fraction, would be minuscule, and the sensitivity of MRI would not be sufficient to detect them.

While optical techniques can potentially miss the cavitating bubbles and thus underestimate the void fraction, the presented MRI measurement technique can overestimate the void fraction. As the measurement takes several minutes, large degassing bubbles will travel through the cuvette, reducing the measured spin density. Also, as the nuclear magnetization decreases with the increasing temperature, there is a potential mechanism of a cavitation-driven reduction in spin density due to demagnetization of spins by high temperature in the vicinity of collapsing bubbles. The reduction in magnetization would be small but comparable to the void fraction numbers.

There are several other possible mechanisms responsible for the reduction in MR signal, but not, in our opinion, of the measured spin density. First, the MR relaxation time T_2^* can be reduced by free radicals injected into the liquid after the bubble collapses, which, however, would only reduce T_2^* without affecting the spin density. Second, the velocity-driven ''ghosting'' can contribute to the signal; however, for the given resolution and range of measured velocities, the ghosting should be contained within a single pixel. In addition, its effect would be greater in media with greater velocities. As the flow in SDS solution was faster while its void fraction data were lower than those in water, this mechanism does not appear applicable.

3.3.2 Velocity measurements

The mean velocity maps show the formation of a macroscopic flow along the direction of the sound, with a circulation around the horn (water and SDS sample Z velocity slices, shown in figure 3-3 A and B). A slice of the X component velocity map, taken at one

pixel (1.25 mm) from the horn's surface, shows that the circulation becomes quite strong near the horn (figure 3-3 C and D). It appears that the circulation pattern influences the geometry of the void fraction: The circulation refreshes the horn surface and directs the bubbles toward the center. In its turn, the absorption of acoustic energy by the bubbles leads to the flow, thus providing a feedback for more developed circulation and forming the cavitation cloud. This effect is more pronounced in void fraction, and velocity maps for the surfactant-containing samples.

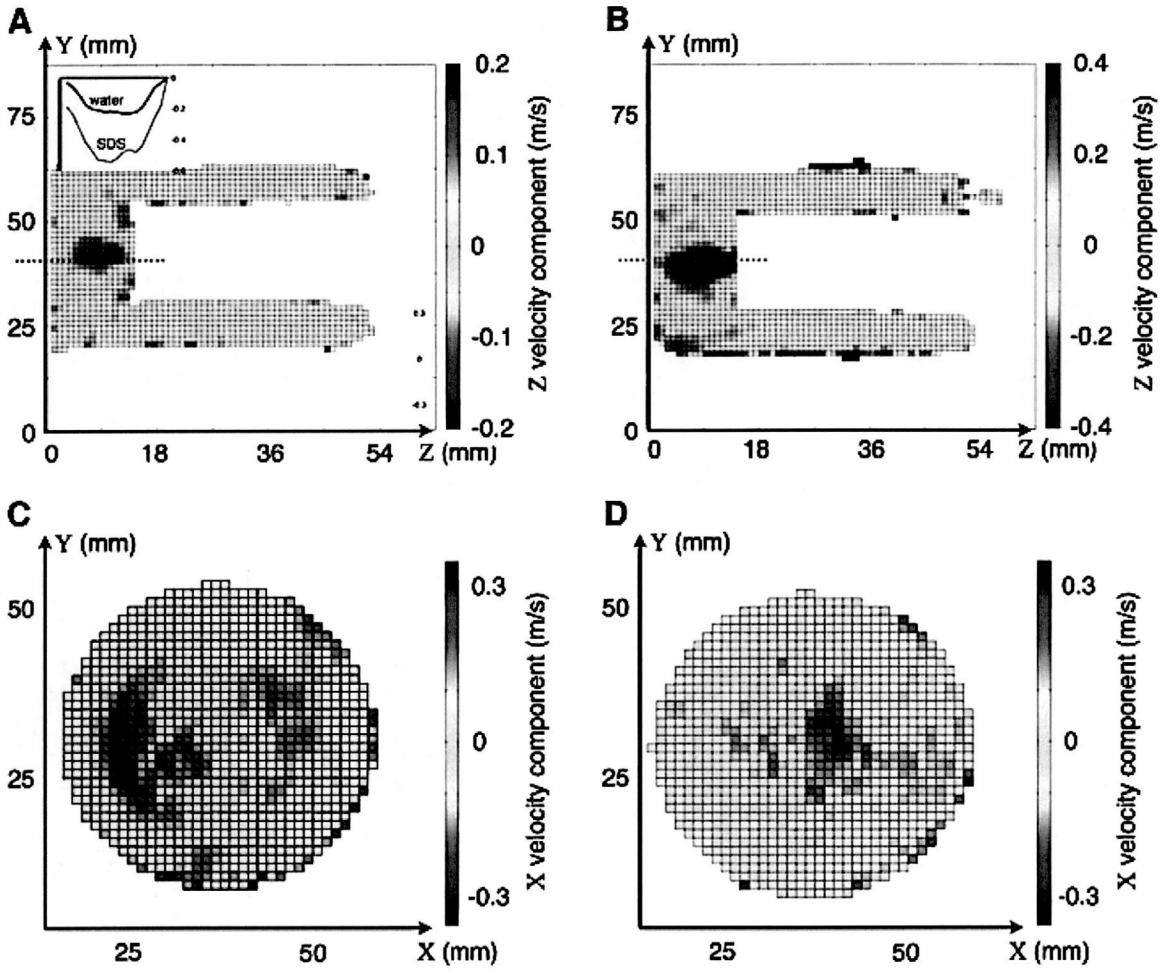

Figure 3-3 Z component of velocity maps for water (A) and SDS solution (B). The color scale is in m/s, and is different in (A) and (B). The inset at the top of figure 3-3 A is the profile of velocity at point #32 indicated by the dotted lines in (A) and (B). Figures (C) and (D) are slices across the cuvette at 1.25 mm from the tip of the horn (at pixel #16 in Z direction) through X component velocity maps for water and SDS solution.

The water flow is faster in surfactant solutions. A possible explanation is a better coupling between the bubbles and the surrounding water due to higher bubble stability. At the given ultrasonic frequency (19.1 kHz), acoustic streaming in the liquid is produced by the cavitating bubbles [10], and macroscopic motion of water is a result of a balance between the coherent and incoherent bubble motions. As the bubbles are produced at the surface of the horn, they are pushed away by the acoustic radiation force. The amount of water following them depends on the number and the total surface area of the bubbles. The SDS film prevents the bubbles from coalescing and growing quickly, leaving rectified diffusion (growth caused by the change in the bubble surface area and the gradient of pressure as a function of the bubble volume) as the main growth mechanism, which takes a much longer time than our measurement interval [11-14]. These factors result in the development of stronger and more coherent flow.

A region of elevated velocity is also present in the surfactant solution at approximately $^1/_4$ wavelength behind the tip of the horn and at the region of expected accumulation of the bubbles of smaller than the resonant size [15]. The same region is manifest, to varying degrees, in the void fraction, velocity and divergence maps.

The velocity profiles, as taken along the dotted lines in figure 3-3 away from the center of the horn (each velocity value is measured from a volume of 0.9*0.9*1.25 mm), are shown in the upper inset to figure 3-3 A. Two facts are worth mentioning: first, the velocity increase is consistent for the first 6 mm from the horn for both samples, where the void fraction is the greatest, and second, the acceleration of the fluid is much higher in the SDS sample: 37 m/s^2 vs. 6.6 m/s^2 (using $dv/dt = vdv/dt$).

The presence of the cavitating bubbles makes the two-phase fluid compressible. We can calculate the importance of compressibility for the flow behavior by comparing the first two terms in the continuity equation (figure 3-4 A and B):

$$\mathrm{div}\,\vec{V} + \vec{V}.\mathrm{grad}(\ln\varphi) + {}^{\mathrm{d}(\ln\varphi)}/_{\mathrm{dt}} = 0 \qquad (5)$$

where φ is the normalized density expressed as the ratio of the spin density maps with and without the cavitation.

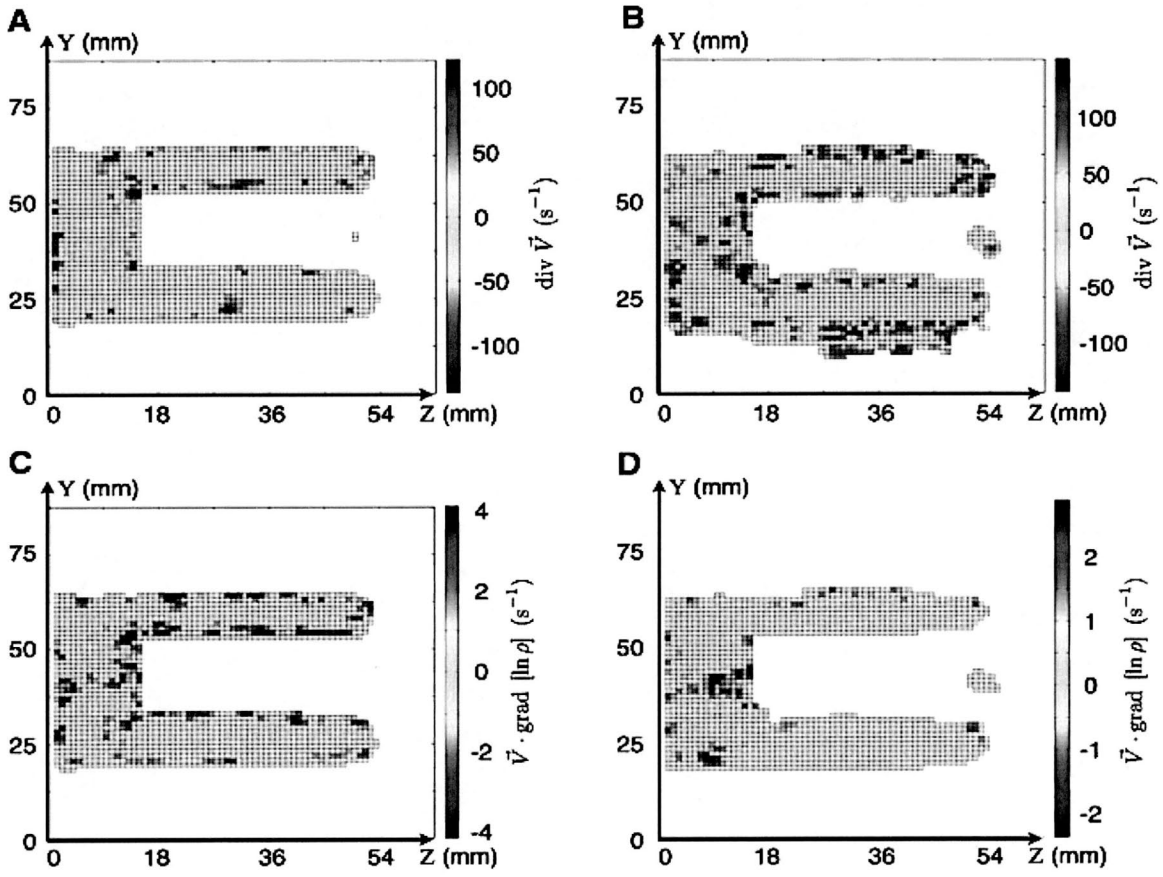

Figure 3-4 Middle slices of divergence maps for water (A) and SDS solution (B). C and D are the corresponding slices of V.grad(lnφ): The vertical direction corresponds to the Y (vertical) orientation, the horizontal is in the Z orientation, against the ultrasound direction. The color scale is in s^{-1}, as for (A) and (B).

The term of the density gradient is non-zero (figure 3-4 C and D), and is at its maximum next to the regions of highest void fraction, near the tip of the horn. The gradient density map for the water sample looks much more uneven than that for the surfactant solution, with both positive and negative regions noticeable, possibly because of more actively coalescing bubbles playing a large role. For the SDS sample, the high intensity region is further from the horn and is mostly positive, possibly indicating a region of bubble expansion. The gradient term of the equation is much smaller than the divergence of the velocity, which is larger, on average, by a factor of 50.

The derivatives of the velocity data are noisy, with uncertainties as high as 28%, preventing a quantitative analysis. However, the major features of the velocity divergence and vorticity maps, localized near the horn tip, permit several qualitative observations. The velocity divergence for our system characterizes the conversion of acoustic energy into kinetic energy of the liquid and, as such, can be used as a measure of the interaction between the bubble cloud and the liquid. The high divergence area near the horn is wider and of greater magnitude for the SDS solution and is also at a greater distance from the horn than in the water sample: The bubbles that interact strongly with the liquid occupy a more extended area in the surfactant solution. In the water solution, the region of high divergence where the interaction is the greatest, is smaller and closer to the tip of the horn. This is presumably because the bubbles have not increased too much in size (coalescence reducing the bubble–liquid interaction further from the horn).

The vorticity maps (the magnitude of $\mathrm{curl}\vec{V}$ and angular velocity $\vec{\omega} = \frac{1}{2}(\mathrm{curl}\vec{V}).\vec{Z}$ are shown in figure 3-5) show a higher turnover rate in the SDS solution in the region with a greater void fraction, indicating an active rotation locally. This is not noticeable in the

water sample. Another well-defined feature of the flow in the SDS solution is the opposite signs of the angular velocity on the opposite sides of the central jet, due to the rotation produced by the circulation of water (also seen in figure 3-3 D).

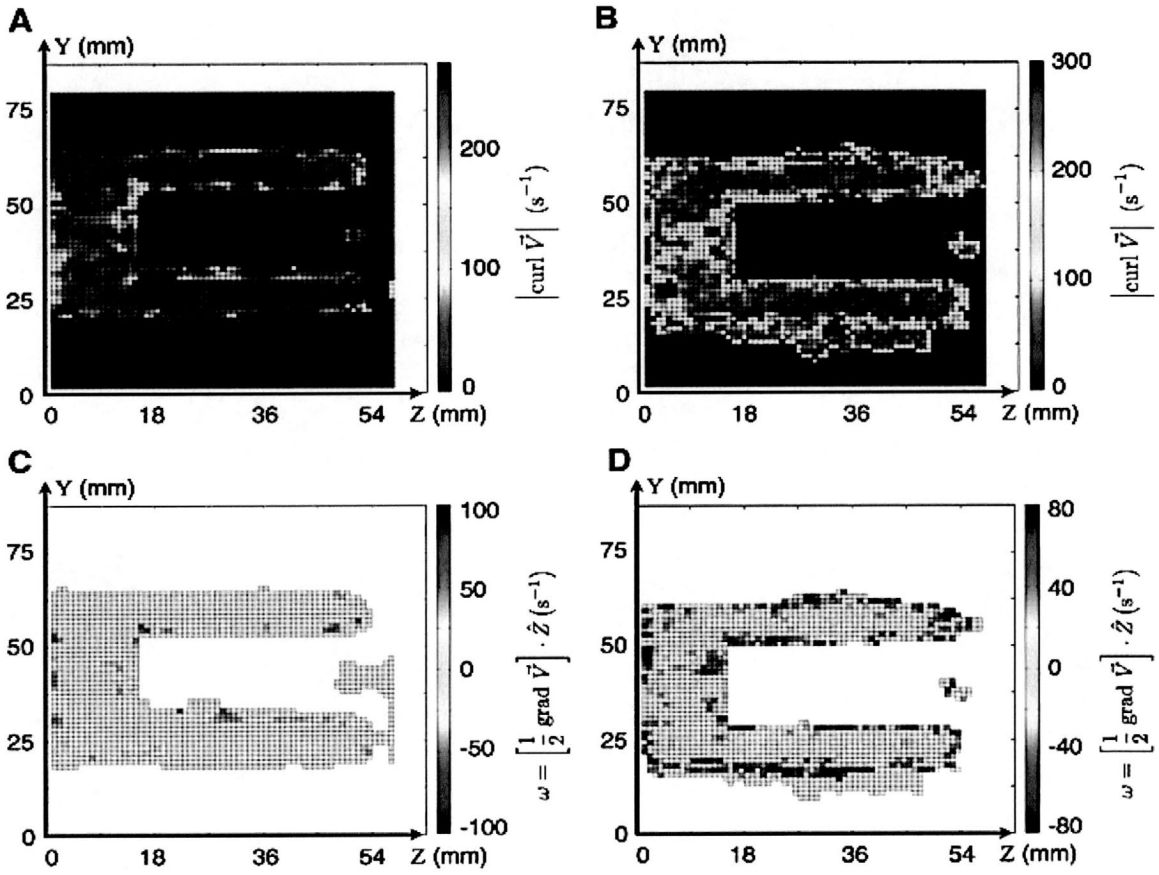

Figure 3-5 Middle slices of vorticity (curlV magnitudes for water (A) and SDS (B) solutions in s^{-1}). C and D show the angular velocities around the direction of the flow for water and SDS solutions, respectively.

3.4 Conclusion

In this chapter, we demonstrated the application of phase encoding MRI techniques with short characteristic measurement times (in the 0.1–2 ms range) to studies of acoustic cavitation. The technique allowed us to obtain data free from inhomogeneity-produced artifacts, and enabled a quantitative analysis of processes in the cavitating medium.

We estimated the mobility of water in the vicinity of the cavitating bubbles: As the MR signal decay exhibited exponential behavior, the local mechanical dispersion D had to be at least an order of magnitude greater than diffusion in the quiescent water for bubbles of average radius 1 μm, and much greater still for the larger bubbles, as $D \gg 2R^2/10^{-4}$ s.

We presented a new technique to measure the void fraction, and applied it to two samples with different cavitation properties and average bubble volume. The technique represents an independent method for obtaining information about the local liquid motion around the cavitating bubbles. It should be noted that the analysis used here applies strictly only to spherical bubbles and thus has limitations. The approach can be further refined to obtain information about the bubble size distribution, when the analysis of susceptibility effects of various bubble sizes and shapes on the relaxation time is performed (see Chapters 4 and 5).

We further quantified the flow processes in the system by measuring three-dimensional velocity fields, which demonstrated the relationship between the bubble dynamics on the micro-scale and the flow properties on the macro-scale.

The bubble lifetime and evolution determine the flow of the surrounding liquid, which, in turn, participate in the formation of void fraction shape, directing the bubbles toward the center of the horn, thus creating a feedback mechanism. This mechanism can be

manipulated by a modification of the bubble dynamics via the addition of surfactants, leading to changes in both bubble and liquid flow fields, which can be quite useful in applications of strong cavitation.

We believe that the presented measurement approach, phase encoding MRI techniques with short characteristic measurement times, are useful in studies of both acoustic and hydrodynamic cavitation [16] and multi-phase flow systems in general.

3.5 References

[1] D. Sunartio, M. Ashokkumar, F. Grieser, "Study of the coalescence of acoustic bubbles as a function of frequency, power, and watersoluble additives", Journal of American Chemical Society ,2007, 129(18), 6031–6036.

[2] Y. Iida, M. Ashokkumar, T. Tuziuti, T. Kozuka, K. Yasui, A. Towata, J. Lee, "Bubble population phenomena in sonochemical reactor: I. Estimation of bubble size distribution and its number density with pulsed sonication-laser diffraction method", Ultrasonics Sonochemistry, 2010, 17(2), 473–479.

[3] R. Brown and P. Fantazzini , "Conditions for initial quasi-linear T2-1versus tau for carr-purcell-meiboom-gill nmr with diffusion and susceptibility differences in porous-media and tissues", Journal of Physical Review B, 1993, 47(22), 14823–14834.

[4] J. Mitchell, T. Chandrasekera, M. Johns, L. Gladden, "Nuclear magnetic resonance relaxation and diffusion in the presence of internal gradients: the effect of magnetic field strength", Physical Review E, 2010, 81, 026101.

[5] I.V. Mastikhin, B. Balcom, P. Prado, C. Kennedy, "Sprite MRI with prepared magnetization and centric-space sampling", Journal of Magnetic Resonance, 1999, 136(2), 159–168.

[6] R. Dharmakumar, D. Plewes, G. Wright, "On the parameters affecting the sensitivity of mr measures of pressure with microbubbles. Magnetic Resonance in Medicine, 2002, 47, 264–273.

[7] P. Tho, R. Manasseh, A. Ooi , "Cavitation microstreaming patterns in single and multiple bubble systems", Journal of Fluid Mechanics, 2007, 576, 191–233.

[8] S. Wu, T. Leong, S. Kentish, M. Ashokkumar, "Frequency effects during acoustic cavitation in surfactant solutions", Journal of Physical Chemistry B, 2009, 113(52), 16568–16573.

[9] F. Burdin, N. Tsochatzidis, P. Guiraud, A. Wilhelm, H. Delmas, "Characterisation of the acoustic cavitation cloud by two laser techniques", Ultrasonics Sonochemistry, 1999, 6(1–2), 43–51.

[10] I. Mastikhin and B. Newling, "MRI measurements of an acoustically cavitated fluid in a standing wave", Physical Review E, 2005, 72(5), 056310.

[11] A. Eller and H. Flynn, "Rectified diffusion during nonlinear pulsations of cavitation bubbles", Journal of Acoustical Society of America, 1965, 37(3), 493–503.

[12] L. Crum , "Acoustic cavitation series: part five rectified diffusion", Ultrasonics, 1984, 22(5), 215–223.

[13] K. Yasui, "Influence of ultrasonic frequency on multibubble sonoluminescence", Journal of Acoustical Society of America, 2002, 112(4), 1405–1413.

[14] M. Ashokkumar, "The characterization of acoustic cavitation bubbles – An overview", Ultrasonics Sonochemistry, 2011, 18, 864–872.

[15] T. Leighton, "Bubble population phenomena in acoustic cavitation", Ultrasonics Sonochemistry, 1995, 2(2), 123–136.

[16] S. Gopalan and J. Katz , "Flow structure and modeling issues in the closure region of attached cavitation", Physics of Fluids, 2000, 12, 895.

4 - Magnetic susceptibility based Magnetic Resonance estimation of micro-bubble size for the vertically upward bubbly flow

4.1 Introduction

In this chapter, we applied the approach developed for the MR analysis of stable micro-bubbles to studies of vertical bubbly flows using pure phase encode methods. We analyzed the general equation relating the void fraction, T_2^* change, diffusion, and the average bubble radius, and showed that, due to slow diffusion in the quiescent water, the long measurement times make the use of pure phase encode methods impractical. However, much faster diffusion in the bubbly flows extends the fast diffusion limit down to short (2 ms) measurement times. This permits the use of the simplified analytical expression to extract the micro-bubble size information, both in bulk and spatially resolved, and enabling us to employ the pure phase encode conical SPRITE and SE-SPI measurements to accomplish that goal.

We demonstrated that the strong bubble-induced reduction in T_2^* necessitates the use of very short encoding times and pure phase encode methods to accurately measure the void fraction.

Average bubble sizes were measured at various airflow rates. There was an expected underestimation of bubble sizes at faster airflow rates due to the limitations of the theory; derived for small bubble sizes and non-interacting bubbles (low void fractions and airflow rates). This approach lends itself to studies of bubbly flows and cavitating media characterized by small bubble sizes and low void fractions.

4.2 Theory

Gaseous bubbles have different susceptibility from surrounding water, and this introduces a field gradient which alters the MR T_2^* relaxation time. The broadening of the magnetic field within voxels is the reason for local T_2^* changes, which can be described by Eq. (1) in the absence of diffusion:

$$\frac{1}{T_2^*} = \frac{1}{T_2} + \gamma \Delta B(r), \qquad \Delta B(r) = C \Delta \chi B_0 \tag{1}$$

where γ is the gyromagnetic ratio, C carries information about the spherical bubble radius and position, $\Delta\chi$ is the magnetic susceptibility difference, B_0 is the magnetic field in free space, and $\Delta B(r)$ is the field offset. For a sphere of radius R and magnetic susceptibility χ_1 immersed in a medium with different magnetic susceptibility χ_2, the field offset can be expressed in the spherical coordinate system as (assuming a uniform static magnetic field B_0 along the Z axis) [1]:

$$\Delta B_z(r, \theta) = \frac{1}{3} . B_0 . (\chi_2 - \chi_1) . \left(\frac{R}{r}\right)^3 . (3 \cos^2 \theta - 1) \tag{2}$$

The magnetic susceptibility variation within the sample also reduces the MR T_2 relaxation time, which occurs as a result of phase accumulation by spins diffusing through the local perturbations. Magnetic susceptibility induced MR T_2^* changes in the presence of diffusion cannot be described by Eq. (1) anymore. After the initial RF pulse

has created a transverse net magnetization, the spins diffusing in different regions near the bubble will acquire different phases. As a result, their initial phase coherence will be lost and the net magnetization will decrease as a function of $\Delta\chi$, B_0, position r, bubble radius R, and the diffusion coefficient D. Assuming the Gaussian spin phase distribution in the voxel, we can apply the Anderson-Weiss mean field theory to the signal in the presence of stable micro-spheres as magnetic field perturbers [2-4]. The resulting expression takes into account the diffusion of spins D, the normalized void fraction φ, the average bubble radius R, and the measurement time t_p (from [5], corrected):

$$\frac{1}{T^*_{2,new}} = \frac{1}{T^*_{2,B}} + \frac{16}{5}\cdot\frac{\varphi}{D^2 t_p}\cdot\left(\frac{1}{3}\gamma B_0 \Delta\chi R^2\right)^2 \cdot\left[\exp\left(\frac{-Dt_p}{2R^2}\right) - 1 + \frac{Dt_p}{2R^2}\right] \tag{3}$$

The expression has been tested experimentally for the case of stable micro-spheres, in particular in [5], showing a qualitative agreement between the experiment and theory but with a difference on the order of magnitude in control and practical micro-spheres. Two asymptotic limits can be defined based on the characteristic measurement time t_p with respect to the average bubble radius and the diffusion in the medium:

$$\frac{1}{T^*_{2,new}} = \frac{1}{T^*_{2,B}} + \frac{8}{5}.\varphi.\left(\frac{1}{3}\gamma B_0 \Delta\chi\right)^2 .\frac{R^2}{D} \qquad \text{if } t_p \gg \frac{2R^2}{D} \tag{4}$$

$$\frac{1}{T^*_{2,new}} = \frac{1}{T^*_{2,B}} + \frac{2}{5}.\varphi.\left(\frac{1}{3}\gamma B_0 \Delta\chi\right)^2 .t_p \qquad \text{if } t_p \ll \frac{2R^2}{D} \tag{5}$$

In Eq. (4), the fast diffusion limit, the decay constant has no dependence on t_p (a purely mono-exponential decay). We can interpret it as follows: the magnetic field changes are significant at the distance from the bubble of the order of the bubble radius, and the spins must have enough time to sample this region (the measurement time must be longer than the average diffusion time for the spins to diffuse in the bubble induced magnetic field gradients). In the other limit, Eq. (5), the decay constant varies with the measurement time.

It is important to point out that Anderson-Weiss mean field theory [4] and its consequent developments (among others, papers by Stables et al. [6] and Dharmakumar et al. [5]) require the randomness in the spin motion (the Gaussian-Markov process) to simplify the correlation function and come up with the analytical description that is employed here. However, the random spin motion can be of any origin: the molecular diffusion as well as the mechanical dispersion will satisfy the theoretical requirements as long as the spins randomly move in the area with bubble-induced magnetic field gradients. In the studied system, air bubbles rising in stagnant water introduce a substantial velocity gradient into the water motion, and this velocity gradient takes place on the scale of a bubble size. Migration of water molecules across the velocity gradient greatly enhances the random molecular displacement in a manner akin to Taylor dispersion due to the shear flow on the bubble scale, i.e. where it is the most important. We will continue to use the term "diffusion" in this paper, but with an understanding that a more correct term is "dispersion".

Figure 4-1 A, where bubble-induced relaxation rate is plotted as a function of the bubble radius, shows general Eq. (3) for the void fraction φ of 0.018, measurement time

t_p of 2 ms, magnetic susceptibility difference $\Delta\chi$ of 7 ppm, magnetic field strength B_0 of 4.8 T, and different values of diffusion coefficient D. The dashed line in the figure represents the fast diffusion limit (Eq. (4)) for the fastest diffusion value. The parabolic regions close to the origin correspond to the fast diffusion limit where Eq. (4) is applicable, and where information on bubble size can be reliably extracted. The equation's use beyond that limit will lead to a bubble size underestimation. This problem can be overcome by employing longer measurement times, as it will shift the fast diffusion limit into the larger bubble size region. In figure 4-1 B, the general Eq. (3) is plotted for the measurement time t_p of 15 ms and three different values of diffusion $1*10^{-5}$, $5*10^{-6}$, and $1*10^{-6}$ m^2/s, while other parameters are kept unchanged. One can see that for 15 ms measurement time, the use of the fast diffusion limit (Eq. (4)) extends much further. Here, the fast diffusion limit is plotted in solid, dashed, and dotted lines for the same diffusion values.

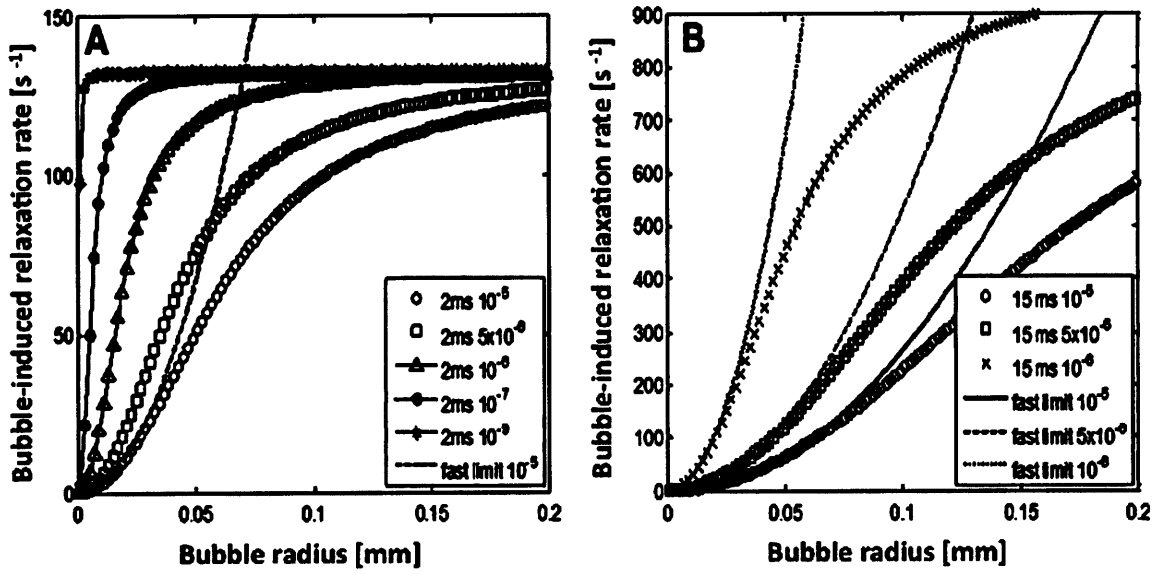

Figure 4-1 Theoretical analysis (Eqs. (3) and (4)): (A) Bubble-induced relaxation rate in s^{-1} vs. bubble radius in mm for the measurement time of 2 ms for various diffusion coefficients. The fast diffusion limit (Eq. (4)) is plotted in the dashed line for the diffusion coefficient D of 10^{-5} m^2/s. (B) The same for the measurement time of 15 ms and the diffusion coefficients D values of $1*10^{-5}$, $5*10^{-6}$, and $1*10^{-6}$ m^2/s. The fast diffusion limit (Eq. (4)) is plotted in solid, dashed, and dotted lines for the same diffusion values.

The same analytical approach generates an expression linking the MR T_2 relaxation with the void fraction, diffusion, and average bubble radius. However, it exhibits a non-monotonic behavior versus the bubble size, complicating the bubble size analysis based on T_2 measurements, so it was not explored further.

4.3 Methods

Figure 4-2 shows the experimental setup. All MRI measurements were performed on a vertical bore superconducting 4.8 T magnet (Cryomagnetics, Tennessee) with the Apollo console (Tecmag, TX). The sample was placed in a 2 cm diameter cylindrical glass tube open on top for free air flow, and equipped at the bottom with a 1.2 cm diameter frit (14-16 μm sized porous glass, "medium" size, Aldrich, ON) with a ball valve. The tube's bottom end was connected to an adjustable Matheson flow meter and then to a source of air regulated to flow at 6 different rates: 12.43, 22.67, 36.37, 52.96, 72.4, 94.92 cubic centimeter per minute (CCPM). The liquid phase was doped by either 0.4 mM or 5 mM of manganese sulfate ($MnSO_4$) to reduce the MR longitudinal and transverse relaxation times for faster acquisition. It should be noted that an addition of 5 mM of $MnSO_4$ reduces the susceptibility difference by 25%, which must be taken into account [7].

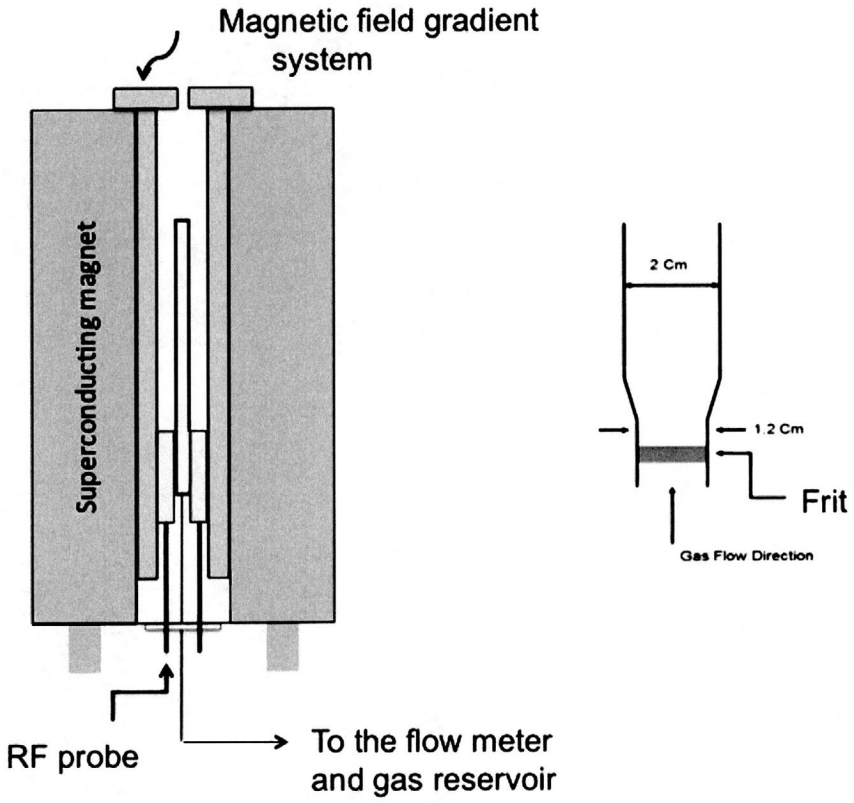

Figure 4-2 Experimental setup.

Optical measurements were performed with a Sony HDRFX1000 High Definition MiniDV Handycam Camcorder with 20x optical zoom and side illumination. The 1 ms shutter speed was employed to facilitate distinguishing individual bubbles. Bubbles with well-defined shapes were measured, and the results were averaged.

4.3.1 Bulk measurements of void fraction, T_2^*, and diffusion:

The standard single RF pulse sequence was used to obtain the FID of 5 mM of $MnSO_4$ solution with 2048 acquisition points, DW of 10 μs, and 1 signal average. The sample glass tube was filled with solution to completely occupy the RF probe sensitive volume. The measurements were done for 6 airflow rates (see above) and the stationary sample. The FID amplitudes were used to calculate the bulk void fraction for each flow rate.

For the T_2^*-diffusion distribution map, we employed the standard PFGSE sequence, and acquired the right half of the echo of 0.4 mM of $MnSO_4$ solution with 512 acquisition points, DW of 31.5 μs, and 4 signal averages. The measurements were done for 20 nonlinearly spaced values of diffusion weighting gradients (0 – 10.8 g/cm) with δ=0.5 ms and Δ=10 ms. The 2D inverse Laplace transform was employed to obtain the T_2^*-diffusion distribution [8].

4.3.2 3D measurements of void fraction, T_2^*, and diffusion:

The spin density and T_2^* mapping employed the 3D pure phase encode conical SPRITE sequence (see 2.6.1). The measurement was done on 5 mM of $MnSO_4$ solution at the same 6 airflow rates as the bulk measurements, with the total measurement time of 1 h

for each dataset, which included 8 different encoding times from 0.12 to 2.02 ms with two signal averages and nominal spatial resolution of 0.625 mm for Z and 0.47 mm for the X and Y directions. The RF excitation pulse length was 3.75 μs (corresponding to the Ernst angle of 22.5°). The MR signal equation at the k-space origin for conical SPRITE has the form of the FID equation [9], so data was fitted to a mono-exponential model ($M_z^0 \sin(\alpha) e^{\frac{-t_p}{T_2^*}}$) yielding the 3D spatially resolved T_2^* maps. For the void fraction measurement, the MRI measurements of the bubbly flow alternated with the measurements of the stationary sample (i.e. no gas flow), and the void fraction map was calculated using Eq. (6):

$$\varphi = \frac{(M_z^0 \sin(\alpha))_{st} - (M_z^0 \sin(\alpha))_{bubbly}}{(M_z^0 \sin(\alpha))_{st}} \tag{6}$$

Using non-velocity compensated spatial encoding gradient waveforms could lead to a ghosting artifact, in the case of a displacement in the phase encoding direction during the encoding time t_p. However, the maximum flow velocity for samples in the Z direction did not exceed 10 cm/s (as checked by MR velocimetry) and was less for the other directions. This means the resulting ghosting for the longest phase encoding time employed was less than the pixel size (0.625 mm) and much lower for the other encoding times.

The volume-averaged void fraction was measured using Eq. (6) for two different phase encoding times, 0.1 and 1 ms, by integrating over the sample volume.

For the diffusion measurement, the 3D motion sensitized pure phase encode SE-SPI (see 2.6.2) was used for 8 different q-values at the same airflow rates and nominal spatial resolution as the void fraction and T_2^* maps with four signal averages. The diffusion encoding was performed in the Z direction: the direction of the main magnetic field and gas flow. The diffusion weighting gradients up to 21.6 g/cm were used with TE=4 ms, δ=0.5 ms, Δ=1 ms, and the encoding time t_p=0.62 ms.

With 4 ms for the echo time and 130 ms for the magnetization recovery time, one time scanning of the complete 64^3 dataset would take about 10 hr. This issue was resolved by using a reduced k-space sampling approach, cutting the measurement time down to less than 20 min for each q-value for each signal average [10]. A template was obtained doing the zero q-point measurement for the no flow condition. Then, all k-space points with the magnitude lower than a threshold and their corresponding imaging gradient values were identified and withdrawn. For all MRI measurements only significant k-space points were sampled and omitted points were replaced by zeros. Since the insignificant k-space points were mostly located in the periphery of the reciprocal space, filling the reduced k-space with zeros acted like a low pass filter. Much shorter measurement time and higher SNR could be achieved by using Gadolinium based agents such as $GdCl_3$, however, the high sensitivity of relaxation parameters of the Gd-based solution to small temperature rises caused by active magnetic field gradients was discovered to be problematic.

4.4 Results and Discussion:

4.4.1 Bulk Measurements:

The bulk and 3D SPRITE volume-averaged measurements of void fraction demonstrate the scale of T_2^* changes induced by bubbles in the bubbly flows. In figure 4-3 A, the void fraction is shown to be linearly dependent on the airflow rate while the strong T_2^* effect driven by the susceptibility difference is negligible (very short phase encoding time). The void fraction measured by volume averaging of 3D SPRITE data with the phase encoding time of 0.1ms still shows a linear dependency on the airflow rate (figure 4-3B), while for the void fraction obtained by volume averaging of 3D SPRITE data acquired at the longer phase encoding time of 1 ms, the deviation from the linearity rapidly increases with the airflow rate (figure 4-3 C), becoming more than 5 times greater than the short encoding time data. This result proves the T_2^* change in the sample due to the presence of bubbles, and suggests that this effect is large enough to show up at long time scales, and can be ignored only by the employment of very short measurement times. Figure 4-3 D demonstrates how the susceptibility driven relaxation rate changes linearly with the airflow rate.

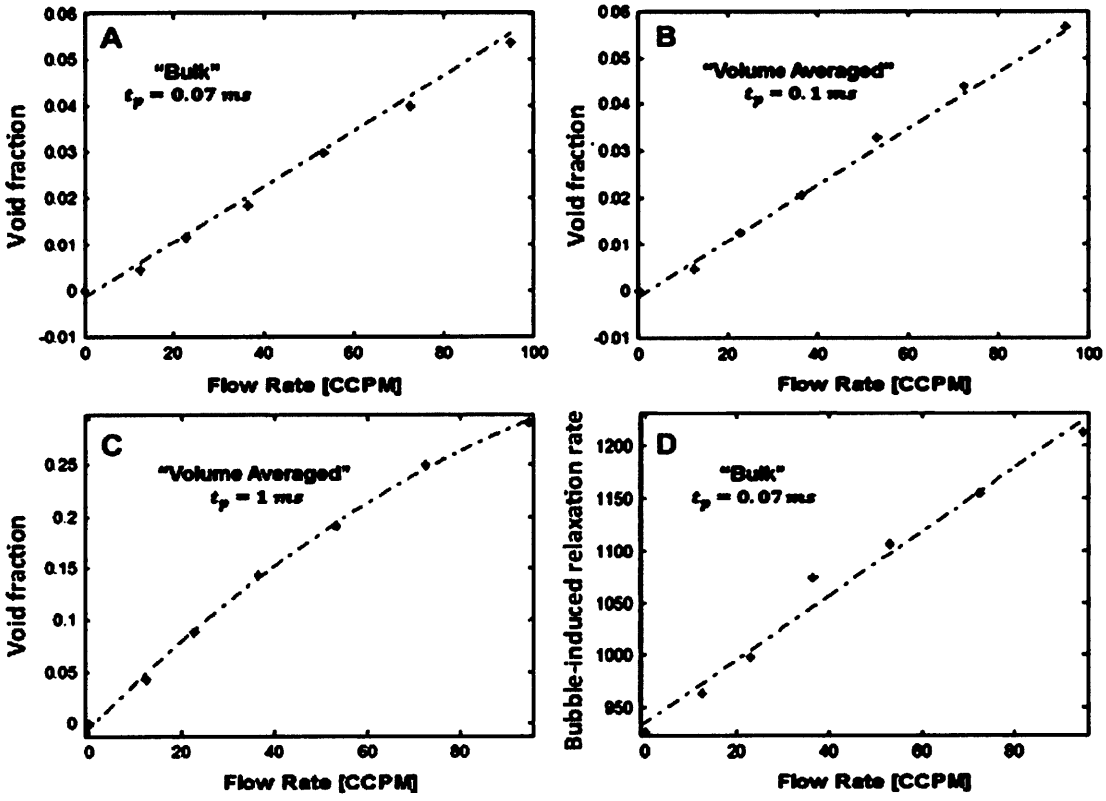

Figure 4-3 The relation between void fraction and flow rate in CCPM: (A) bulk, (B) volume averaged (t_p= 0.1 ms), and (C) volume averaged (t_p= 1 ms). Void fraction is normalized. (D) The bulk bubble-induced relaxation rate in s^{-1} vs. airflow rate in CCPM.

The relaxation effects are reduced at shorter encoding times. If one desires to measure the void fraction map without performing T_2^* mapping (as was the case in this work) but rather by simply using the SPRITE sequence with short encoding times, it is imperative first to measure the signal in the absence of the bubbly flow. The resulting dataset will carry information on the T_2^* of water in the absence of the flow, with a single point intensity of $S = S_0 e^{(\frac{-t_p}{T_2^*})}$. The intensity of the dataset for the bubbly flow will be then $S = S_0 e^{-t_p\left(\frac{1}{T_2^*}+\frac{1}{T_{2,bubble}^*}\right)}$. The intensity will be then reduced by the factor of $e^{-(\frac{t_p}{T_{2,bubble}^*})}$. If the deviation of less than 5% from the true value of the void fraction is desired, then it is easy to show that $t_p = -T_{2,bubble}^* * \ln(0.95)$. Having $\frac{1}{T_{2,bubble}^*} = 300\ s^{-1}$ as for our highest flow rate, the encoding time required for accurate measurements of the void fraction must be less than 170 μs.

T_2^*-diffusion distribution maps are displayed in figure 4-4 A-C for the airflow rates of (A) 12.43, (B) 36.37, and (C) 94.92 CCPM. Axes are in logarithmic scales. As the airflow rate increases, diffusion increases steadily up to 10^{-5} m^2/s until two distinct peaks, separated both along the diffusion and T_2^* relaxation axes, appear at the highest airflow rates (starting at 72.4 CCPM, not shown). This indicates a transition from the clustered bubbly flow to slug flow; characterized by the appearance of large (several mm radius) and coalesced "cap" bubbles, which is also confirmed by visual observations.

For the measurement time of 15 ms, the maximum bubble size reliably estimated from the T_2^*-diffusion and the void fraction data is on the order of 0.07 mm. The employed model assumes bubbly flow well separated spherical bubbles. For the lowest airflow rates, this requirement still holds, and we can calculate the average bubble size as a

function of the airflow rate, shown in figure 4-4 D. The model considers bubbles as non-interacting spheres. When bubbles grow, they begin to interact, and the model will no longer be useful. We can estimate its upper applicability range as the one when diffusing spins experience magnetic field gradients of more than one bubble. We can represent each bubble as surrounded by a sphere of doubled radius. The close-packing of equal spheres has a maximum filling volume fraction of 0.74. For the case of bubbles as equal spheres surrounded by double radius spheres, the maximum void fraction is then 0.74/8 = 0.0925. This, of course, is the uppermost limit; in reality, bubbles begin to interact at much lower void fractions.

When bubbles interact, regions with the magnetic field gradients begin to overlap, and the total gradient experienced by water spins in the bubbles' vicinity will be reduced. Therefore, at very low airflow rates, when the bubbles do not interact, the relaxation rate will follow linearly the airflow rate increase. When the airflow rate increases further, and the bubble numbers become such that the bubbles actively interact and coalesce, the relaxation rate will increase more slowly. To summarize, we should expect that the average bubble size, as measured with the proposed approach, would be underestimated at higher airflow rates.

The optical method, on the other hand, overestimates the bubble size as larger bubbles prevent detection of smaller ones, and the light reflection on their menisci visually exaggerates bubble sizes. There is also a principal difference in that the employed optical measurement does not measure the bubble density, only their average sizes at a fixed moment in time whereas the MR measurement uses the signal averaged over time and over volume: either over the whole sample as in the bulk measurement or over the voxel

as in the 3D spatially resolved measurement. The bubble radius estimates obtained with the bulk MR and optics-based methods are compared in figure 4-4 D. The error bars of the optics-measured bubble size show the standard deviation, which increases with the airflow rate (not completely shown for the highest flow rate as the bubble size becomes comparable with the pixel size) where the presence of (at least) two distinct bubble sizes manifests itself also in the MR measurements.

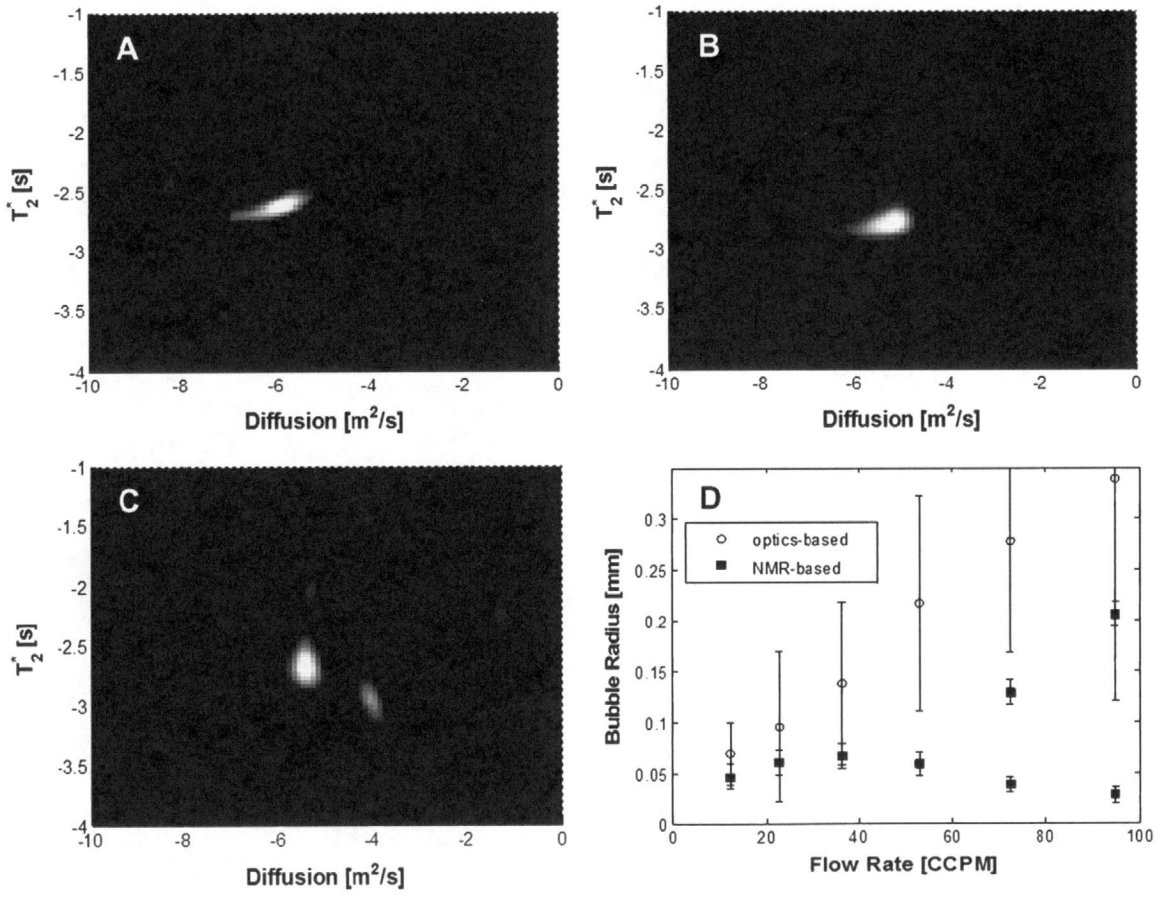

Figure 4-4 The T_2^*-diffusion distribution map for the airflow rates of: (A) 12.43, (B) 36.37, and (C) 94.92 CCPM. Axes are in logarithmic scales. (D) The average bubble radius estimates in mm measured with bulk MR and optical methods for 6 different airflow rates.

4.4.2 Spatially Resolved Measurements:

SPRITE MRI seems a promising technique for the study of two phase gas-liquid dynamic systems (generally all systems that can be described by time averaged properties) for four main reasons: (1) it can image samples with short T_2^* due to short encoding times, (2) it is not affected by time domain artifacts like those caused by magnetic susceptibility and chemical shift, (3) fast flow rates can be imaged successfully without being affected by the ghosting effect because of its short characteristic phase encoding times, and, (4), when combined with a centric k-space sampling scheme, it can provide quantitative spin density weighted images. A typical SPRITE acquisition time for a 3D dataset is several minutes so the information about a fast-changing sample becomes statistically averaged. The characteristic measurement time of SPRITE, however, is the encoding time, i.e. time between the RF pulse and the data acquisition of the resulting FID, and it can be quite short. In our measurements, the longest encoding time was 2 ms. That imposed limitations on the average bubble size estimation: for bubbles larger than ~0.05 mm, the fast diffusion limit would not hold (see Theory and figure 4-1). That also means that the magnetization decay would no longer be mono-exponential if larger bubbles dominated the volume.

We performed T_2^* mapping with the 3D conical SPRITE by acquiring datasets at 8 different encoding times for the airflow rate of 36.37 CCPM, and did the mono-exponential fitting of the measured FID to extract both the spin density and T_2^* information. The goodness of the mono-exponential fitting was checked by calculating the R^2 values. Figure 4-5 A shows the middle slice of the resulting 3D R^2 map. R^2 values greater than 0.95 almost everywhere confirm the mono-exponential fit as a perfect model

for the void fraction and T_2^* mapping (R^2 value can take any value between 0 and 1 and closer to 1 means a better fitting) except near the top of the sample where R-square values are lower. That was expected as the gaseous bubbles, after propagation through the liquid phase started coalescing and approaching the free surface by forming non-spherical over-sized bubbles comparable to the pixel size. The quality of the diffusion measurement mono-exponential fit was also found to be satisfactory based on its R^2 map (figure 4-5 B) except for the right end of the sample starting at column # 43 to the right, which is omitted in the figure. This portion of the sample was lying in the non-linear part of the RF probe with a 12% reduction in sensitivity. This manifested itself more in the SE-SPI measurement where an exact refocusing pulse is required.

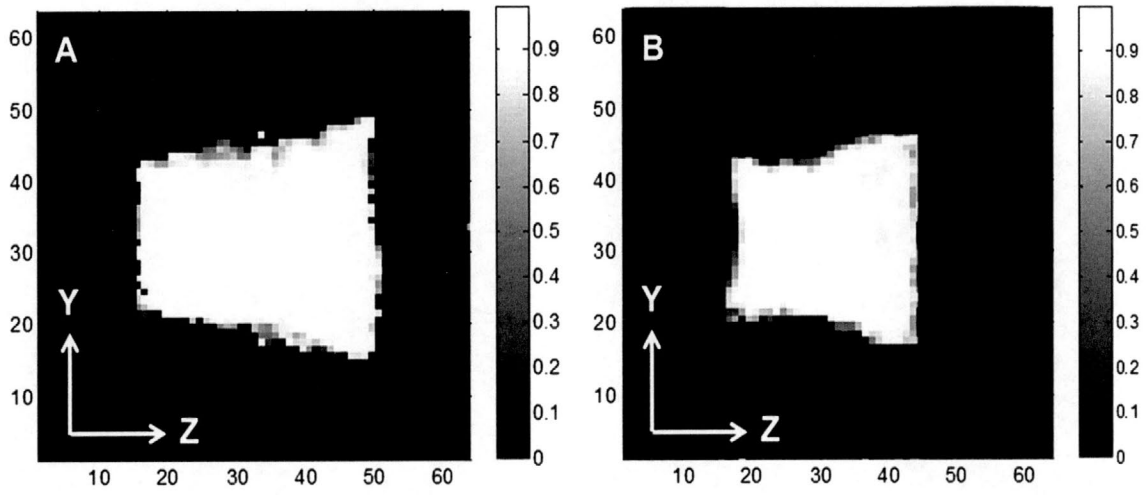

Figure 4-5 The middle slice of the R-square map for: (A) T_2^* fit of the SPRITE T_2^* mapping, and (B) diffusion fit of the SE-SPI diffusion mapping. R^2 value closer to 1 is indicative of a good agreement with the mono-exponential decay. The pixel size in the Z and X or Y direction is 0.625 mm and 0.47 mm, respectively. Maps correspond to the airflow rate of 36.37 CCPM.

The mono-exponential decay of the conical SPRITE signal made it straightforward to extract T_2^* relaxation time and spin density (void fraction) information. The middle slice of the 3D void fraction map is presented in figure 4-6 A. Figure 4-6 B shows the axial view of the void fraction taken from column # 17 immediately next to the frit (indicated by the white dashed line in figure 4-6 A). The middle slice of the 3D bubble-induced relaxation rate map is also shown in figure 4-6 C, and figure 4-6 D illustrates the bubble-induced relaxation rate on the same axial plane. According to the axial view maps, the highest void fraction and bubble-induced relaxation rate values are located on the upper left corner and lower central part of the frit. The non-uniformity of the void fraction and bubble-induced relaxation rate values on the axial maps indicates an uneven gas stream through the frit, which was caused by blocked holes. The analysis of the Y-Z views reveals that void fraction and bubble-induced relaxation rate values are higher close to the frit, and they become smaller as moving away from the frit to the other end of the sample. This may suggest that it is the density of gaseous bubbles that is the determining factor. This agrees well with our visual observations in which a denser population of bubbles was observed at the bottom of the sample where the glass tube had its smallest diameter; as bubbles reached the wider section of the glass tube they scattered all over the available space. It should be noted that the data does not represent an instantaneous image of the bubbles, but an average void fraction and bubble-induced relaxation rate over the measurement time (several minutes for each phase encoding times).

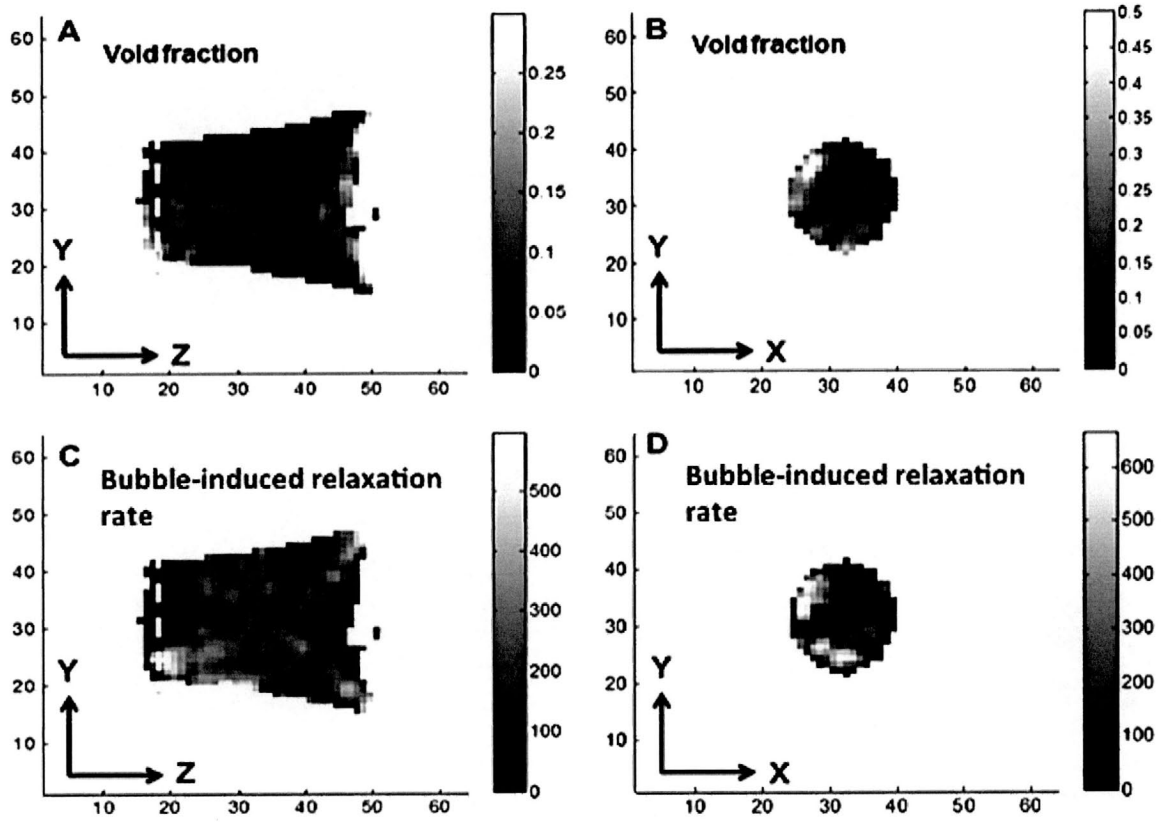

Figure 4-6 The 3D void fraction map: (A) middle slice, and (B) axial view. The color scale shows void fraction numbers. The 3D bubble-induced relaxation rate map: (C) middle slice, and (D) axial view. The color scale is in s^{-1}. The position of the axial views is indicated by the white dashed line for each case. The pixel size in the Z and X or Y direction is 0.625 mm and 0.47 mm, respectively. Maps correspond to the airflow rate of 36.37 CCPM.

With SE-SPI, reading the MR signal in the absence of the spatial encoding gradients enables a narrow filter width for better SNR. No linewidth restriction on image resolution (no extra blurring), as the other positive feature of the sequence, makes the sequence a perfect choice for accurate diffusion measurements in heterogeneous media where magnetic susceptibility variation within the sample can be an obstacle for quantitative measurement. The middle slice of the 3D diffusion map is illustrated in figure 4-7 A. We hypothesize at least two different mechanisms pushing the diffusion about 10^3 times greater than that of ordinary water: the bubble density and bubble coalescence. The diffusion map shows the formation of the greatest diffusion values where an active coalescence of micro-bubbles and generation of over-sized ones was occurring (the right end). Two other distinct diffusion regions on the left half of the map correspond to areas with a dense population of primary and secondary micro-bubbles.

Figure 4-7 B shows the resultant bubble size distribution map. Numbers, representing the average radius of bubbles, are in the range of 5-100 μm with the smaller numbers close to the frit (region 1), and bigger ones occupying region 2: this illustrates the growth process of gaseous bubbles, which is mainly governed by the coalescence of primary bubbles observed in region 1.

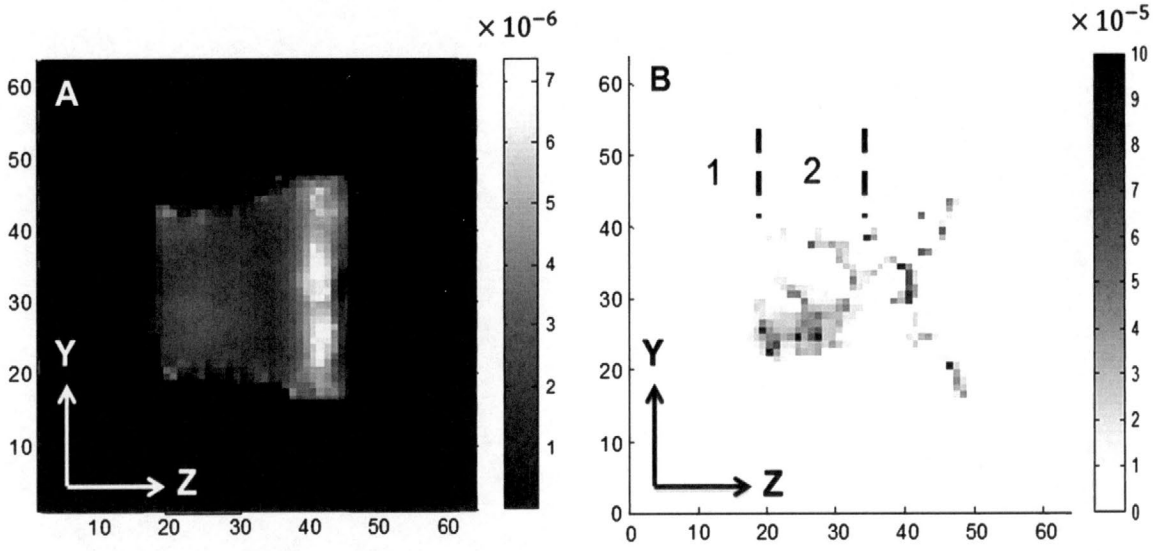

Figure 4-7 (A) The middle slice of the 3D diffusion map. The color scale is in m^2/s. (B) The middle slice of the average bubble radius distribution map. The color scale is in meters. The vacant spaces correspond to zero void fraction and bubble-induced relaxations rate values. The pixel size in the Z and X or Y direction is 0.625 mm and 0.47 mm, respectively.

The average bubble radii obtained with the 3D SPRITE/SE-SPI measurement are in good agreement with those obtained with the bulk measurement. There is also a reasonable agreement with the optical measurements at the low airflow rates.

As discussed in the theory section, this analytical approach holds as long as the spin motion in the bubble vicinity is random, no matter if it is caused by the molecular diffusion or by bubbles rising in water. Our dispersion measurements yielded values of dispersion 1000 times greater than diffusion in quiescent water. The bulk measurements agree well with our spatially resolved measurements of dispersion, meaning that the bubble-inflicted stochasticity takes place at less than the voxel-size level. High R^2 values for the mono-exponential fitting of the diffusive decay further indicate that there is a uniform mixing on the voxel level (i.e. two distinct pools of water with different diffusive decays are not present). Furthermore, inside each voxel for the airflow rates employed in this paper, there are at least 12 bubbles of 30 μm radius. The signal from each voxel thus will be an average over all these different ensembles of spins. It is not the goal of this paper to identify a specific randomization mechanism of the spin motion near the bubbles but it is reasonable to state that there are two levels of randomness present in the system under investigation: one at the molecular level (molecular diffusion), and the other, dominant, at the bubble level. Reasonable agreement between the optical and MR measurements, in our opinion, lends further support to this statement.

4.5 Conclusion:

In this paper, we evaluated the applicability of pure phase encode methods, SPRITE and SE-SPI, for measurements of void fraction and average micro-bubble size (up to 0.07

mm) in vertical bubbly flows. To this end, we employed an approach previously developed for the analysis of MR signal from a medium-filled stable micro-bubbles. The air-water susceptibility difference at the bubble interface generates magnetic field gradients; reducing the MR T_2^*. The approach has been previously applied to extract information on local pressure parameters when the initial micro-bubble size is known beforehand [5,11,12]. We attempt to extract information on the unknown micro-bubble size from MR parameters. For that to be successful, it is essential that the water motion in the bubbly flow satisfies the fast diffusion limit with respect to the measurement time. For quiescent water, the fast diffusion limit requires long measurement times incompatible with short encoding times in the SPRITE sequence. However, a very fast dispersion in bubbly flow, three orders of magnitude faster than in quiescent water, makes the use of phase encoding methods practical. The combination of void fraction, T_2^*, and dispersion maps yields the 3D resolved bubble size maps.

The theoretical analysis is derived for non-interacting bubbles so it is expected that as the number of bubbles increases with the airflow rate, the bubble size estimates will be underestimated. For low bubble density (void fraction) and small micro-bubble sizes, the measurement reliability increases. This makes the presented measurement well suited for studies of micro-bubbles in cavitating media where the bubble sizes do not exceed several dozens of microns and the void fraction is on the order, or well below, 1% for the total volume [13]. With the limitations of the analytical approach, Monte-Carlo simulations [12,14] should be considered as an alternative technique to relate the average bubble size, dispersion, and MR relaxations at greater void fraction and airflow rates.

The measurement approach, an acquisition of statistically averaged MR signal modulated by the air-water susceptibility difference in the bubbly flows, represents an interesting counterpoint to recent ultra-fast MRI measurements of a single bubble where the susceptibilities of air and water are matched [15]. While much more time-consuming, our approach enables measurements of micro-bubbles of sizes below MRI spatial resolution and at greater bubble numbers and faster airflow rates.

The bulk measurements of the bubble size were robust and rapid. Although the susceptibility effects are naturally greater at higher fields, very strong changes in T_2^* caused by the bubbly flows make possible an implementation of a similar type of measurement on medium-field benchtop systems for industry-oriented research.

4.6 References:

[1] P.T. Callaghan, "Susceptibility-limited resolution in nuclear magnetic resonance microscopy", Journal of Magnetic Resonance, 1990, 87(2), 304-318.

[2] C.F. Hazelwood, D.C. Chang, U.L. Nichols, D.E. Woessner, "Nuclear magnetic resonance transverse relaxation times of water protons in skeletal muscle", Biophysics Journal, 1974, 14, 583.

[3] P.T. Callaghan, "Principles of nuclear magnetic resonance microscopy", Oxford University Press, NY, 1991.

[4] P.W. Anderson, P.R. Weiss. "Exchange narrowing in paramagnetic resonance", Reviews of Modern Physics, 1953, 25, 269.

[5] R.Dharmakumar, D.B. Plewes, G.A. Wright, "On the parameters affecting the sensitivity of MR measures of pressure with microbubbles", Magnetic Resonance in Medicine, 2002, 47, 264–273.

[6] L.A. Stables, R.P. Kennan, J.C. Gore, "Asymmetric spin-echo imaging of magnetically inhomogenous systems: theory, experiment, and numerical studies", Magnetic Resonance in Medicine, 1998, 40, 432-442.

[7] A.B. Tayler, "Experimental characterization of bubbly flow using MRI", A Thesis submitted for the degree of Doctor of Philosophy, Trinity College, 2011.

[8] M.D. Hurlimann, L.Venkataramanan, "Quantitative measurements of two-dimensional distribution functions of diffusion and relaxation in grossly inhomogeneous fields", Journal of Magnetic Resonance, 2002, 157, 31-42.

[9] I.V. Mastikhin, B.J. Balcom, P.J. Prado, and C.B. Kennedy, "SPRITE MRI with prepared magnetization and centric k-space sampling", Journal of Magnetic Resonance, 1999, 136, 159–168.

[10] D. Xiao, B.J. Balcom, "Two-dimensional T_2 distribution mapping in rock core plugs with optimal k-space sampling", Journal of Magnetic Resonance, 2012, 220, 70-78.

[11] A.L. Alexander, T.T. McCreery, T.R. Barrette, A.F. Gmitro, E.C. Unger, "Microbubbles as novel pressure-sensitive MR contrast agents", Magnetic Resonance in Medicine, 1996, 35(6), 801-6.

[12] R.H. Morris, M. Bencsik, A.K. Vangal, Y. Perrie, "Three-dimensional fluid pressure mapping in porous media using magnetic resonance imaging with gas-filled liposomes", Magnetic Resonance Imaging, 2007, 25, 509–512.

[13] I.V. Mastikhin, B.Newling, "Dynamics of dissolved gas in a cavitating fluid", Physical Review E, 2008, 78, 006316

[14] R.H. Morris, M. Bencsik, N. Nestle, P. Galvosas, D. Fairhurst, A. Vangala, Y. Perrie, G. McHale, "Robust spatially resolved pressure measurements using MRI with novel buoyant advection-free preparations of stable microbubbles in polysaccharide gels", Journal of Magnetic Resonance, 2008, 193, 159–167.

[15] A.B. Tayler, D.J. Holland, A.J. Sederman, and L.F. Gladden "Exploring the origins of turbulence in multiphase flow using compressed sensing MRI", Physical Review Letters, 2012, 108, 264505 - 264509.

5 - MR relaxometry of micro-bubbles in the vertical bubbly flow at a low magnetic field (0.2 T)

5.1 Introduction

Most studies on multi-phase systems (see Section 1.3 and Chapters 3 and 4 in this thesis) were performed at high magnetic fields [1-13]. Those studies employed advanced MRI techniques that required fine-tuned pulse sequences with a sophisticated manipulation of magnetic field gradients. Direct implementation of such techniques on low-field instruments is difficult, if not impossible. At the same time, a quantitative MR measurement performed on a low-field system could be of major practical interest, as such systems are commonly used in industry-oriented research.

In this chapter, bulk measurements of vertical bubbly flow at a low magnetic field of 0.2 T were performed. The void fraction measurement was straightforward. The susceptibility-induced modulation of the CPMG decay was quite considerable. To determine if a quantitative analysis of this modulation was possible, we applied Gaussian approximation approaches (as distinct from Dharmakumar's approach, employed in Chapter 4), originally developed by Sukstanskii et al. [14], for randomly distributed, randomly oriented, and isolated impermeable spheres, and Ziener et al. [15], for a simple model of a spherical particle. These new approaches are expected to provide better estimations than those from Dharmakumar's. The simulations run by Dharmakumar et al. in [16], demonstrated a scaling factor of about an order of magnitude between theory and simulation results. In contrast, Ziener et al. obtained a very good agreement between their

theory and experimental results. This is partly because of larger number of assumptions made by Dharmakumar et al. for their derivation, and the fact that the analytical expressions by Sukstanskii et al. and Ziener et al. are based on geometry specific solutions of the diffusion equation through boundary conditions at these surfaces. Sukstanskii et al. also propose a very detailed validity criterion for their method, which permits a more reliable determination of the applicability range of their equations.

The accuracy criterion of the Gaussian approximation was discussed, and its adequacy was verified by control measurements of two different suspensions of silica beads with the same void fraction and different bead radii, 1 and 3μm. We analyzed the MR SE and CPMG signal attenuation functions that relate the void fraction, relaxation rate, spins' randomness, and average micro-sphere radius, in both long and short-time limits. The control measurements of the silica bead suspensions showed that long "characteristic measurement times" (i.e. inter-echo times) and smaller inclusion sizes permit describing the CPMG relaxation rate in the long-time limit regime as linear vs. inter-echo times, and obtaining estimates of the average inclusions' size with a good accuracy.

Two simplified equations were extracted from the short and long-time regimes of the CPMG transverse relaxation rate expressions, which can, for appropriate inter-echo time values τ_{180}, yield estimates of the void fraction and R^2/D with basic relaxometry, without prior information on the system's diffusion or mechanical dispersion, or gas-liquid susceptibility difference.

For bubbly flows, the much more complex dynamics of the system along with the shorter range of echo times (employed due to the limited signal lifetime), added an extra error to the estimates due to the inherent limitations of the theory. Good agreement was

observed between the MR and optics-based estimates for the slowest airflow rate. The deviation, however, increased for higher airflow rates. The simplified equations provided void fraction estimates in excellent agreement with those measured from the FID, and better bubble size estimates than those obtained with the long-time limit equation.

This approach seems well-suited for the study of multiphase systems like cavitating media and ideally separated bubbly flows.

5.2 Theory

Magnetic susceptibility is a measure of the magnetization of a material placed in a magnetic field that either increases or decreases the magnetic field in the material. When a magnetized object is embedded in a given medium with a different magnetic susceptibility, it perturbs the present uniform static magnetic field by introducing magnetic field gradients at the boundaries. This phenomenon can be described for a spherical object at a spherical coordinate system (r,θ) in SI units with Eq. (1) [17] :

$$\Delta B(r) = \frac{1}{3}.\left(\frac{R}{r}\right)^3 .\Delta\chi.B_0.(3\cos^2\theta - 1) \quad (1)$$

where $\Delta\chi$ is the magnetic susceptibility difference, B_0 is the present uniform static magnetic field, and $\Delta B(r)$ is the field offset created. These magnetic field perturbations play a significant role in the process of MR signal formation by enhancing the apparent

rate of MR spin-spin relaxation, which, in fact, occurs as a result of phase accumulation by spins diffusing through the non-uniform magnetic fields.

Magnetic susceptibility-induced inhomogeneities originating from structure-specific objects (e.g. spherical or cylindrical inclusions) can provide useful information about the object's structure and function. Assuming a Gaussian approximation for phases accumulated by diffusing spins in the susceptibility induced field offsets, the MR signal can be formulated as [14]:

$$S(t) = S_0(t)\exp^{-\Gamma(t)} \tag{2}$$

where $S_0(t)$ is the MR signal from the bulk liquid, and $\Gamma(t)$ is the signal attenuation function due to the presence of perturbers. For the SE signal (experiment with $90^\circ - t_E/2 - 180^\circ - t_E/2$), the attenuation function $\Gamma(t)$ has been derived in [14] for randomly distributed and isolated impermeable spheres of radius R for two asymptotic limits:

For the long-time limit $t_E \gg t_D$:

$$\Gamma(t_E) = \frac{4}{45}\varphi(\gamma\Delta\chi B_0)^2 . {t_D}^2 . \left[\frac{4}{9}\tau - \frac{2(\sqrt{8}-1)}{3}\left(\frac{\tau}{\pi}\right)^{1/2} + \frac{11}{27} - \frac{(4\sqrt{2}-1)}{27(\pi\tau)^{1/2}} + O(\tau^{-\frac{3}{2}})\right] \tag{3}$$

In the short-time limit, $t_E \ll t_D$:

$$\Gamma(t_E) = \frac{4}{45}\varphi(\gamma\Delta\chi B_0)^2.{t_D}^2.\left[\frac{3}{4}\tau^3 - \frac{36(4-\sqrt{2})}{35\pi^{1/2}}\tau^{7/2} + O(\tau^4)\right] \quad (4)$$

where φ is the void fraction, γ is the gyromagnetic ratio, $\Delta\chi$ is the magnetic susceptibility difference, B_0 is the field strength, t_D is the characteristic diffusion time, defined as R^2/D, and $\tau = t_E/t_D$. D, here, is a measure of the randomness of the spins' motion, which can be of any origin. Molecular diffusion or mechanical dispersion will satisfy the theoretical requirements as long as the spins randomly move across the bubble-induced magnetic field gradients. For the bubbly flows, bubbles rising in stagnant water introduce a substantial velocity gradient into the water motion, and the migration of water molecules across this gradient greatly enhances the random molecular displacement, hence, called mechanical dispersion.

We can further simplify Eqs. (3) and (4) for very long and very short τ times [14]. For very long echo time $t_E \gg t_D$ (i.e. $\tau \gg 1$), the long-time expansion of the attenuation function (Eq. (3)) is linear in time, and the relaxation rate ΔR_2 induced by impermeable spherical objects can be approximated by the leading term in Eq. (3):

$$\Delta R_2 = \frac{16}{45}.\varphi.(\frac{1}{3}\gamma\Delta\chi B_0)^2.t_D \quad (5)$$

However, for smaller τ values, one should consider the contribution of the other terms, otherwise, it may lead to an erroneous result, as they remain substantial up to very large τ values, and their contribution decreases with time slowly.

For very short echo time $t_E \ll t_D$ (i.e. $\tau \ll 1$), the contribution of the second term ($\sim \tau^{7/2}$) in the short-time regime of the attenuation function (Eq. (4)) might also be ignored.

Ziener et al., in [15], obtained the same results for the SE signal attenuation for a spherical particle for both long and short-time limits. In the long inter-echo time limit, $\tau_{180} \to \infty$, they also showed that the SE and CPMG converge to the same asymptotic form in Eq. (5) above. For the opposite limit of short inter-echo times, $\tau_{180} \to 0$, however, their expression for the CPMG relaxation rate differs by the numerical factor 4 from the leading term in Eq. (4):

$$\Delta R_2 = \frac{1}{60} . \varphi . (\gamma \Delta\chi B_0)^2 . \frac{t_E^2}{t_D} \tag{6}$$

The further analysis of Eqs. (5) and (6) shows that we can extract two important sets of parameters from the measurement of CPMG relaxation rates at long and short inter-echo times. By multiplying Eqs. (5) and (6), we can derive an equation for the inclusion's void fraction φ, which could be used for rough estimates:

$$\varphi = \left(\frac{9/2}{(\gamma \Delta\chi B_0)^2 * t_{E,st}} \right) \sqrt{75 * \Delta R_{2,lt} * \Delta R_{2,st}} \tag{7}$$

By dividing Eqs. (5) and (6), we can also derive an equation for R^2/D, which can be employed to estimate the inclusions' average size:

$$\frac{R^2}{D} = \sqrt{\frac{27 * \Delta R_{2,lt} * t_{E,st}^2}{64 * \Delta R_{2,st}}} \tag{8}$$

where subscript "lt" and "st" refer to the long and short inter-echo times, respectively.

A major potential advantage of this manipulation is the possibility of estimating the void fraction and R^2/D with basic T_2 relaxometry measurements, without the need to employ a magnetic field gradient. In addition, R^2/D estimates can be obtained without prior information on the gas-liquid susceptibility difference.

Generally, the Gaussian approximation framework is considered to be valid for the above stated limits if: for short times, diffusing spins accumulate sufficiently small phases, and in the case of long-time regime, spins sample all possible magnetic field values before the significant decay of the signal. The latter occurs when the characteristic diffusion time t_D is much smaller than the characteristic dephasing time t_c (defined as $(3/\gamma\Delta\chi B_0)$ for spherical inclusions). Sukstanskii and Yablonskiy [14] discussed, in detail, the adequacy of the Gaussian approximation for systems with non-uniform magnetic field gradients (as in the case of susceptibility-induced field inhomogeneities). Accordingly, the discrepancy between the exact signal and its Gaussian approximation on the interval $0 \leq \tau \leq \tau^*$ (τ^* is the time for the signal decay by e^{-1}) can be described by the exponential function (9):

$$\varepsilon = A \exp\left(-k.(p.\varphi)^{1/2}\right) \tag{9}$$

where $A \approx 1.25$ and $k \approx 27$, and p, a dimensionless parameter, is defined as $t_c/t_D = 3D/(\gamma\Delta\chi B_0 R^2)$. It can be understood from (9) that the Gaussian approximation can describe the exact signal with an accuracy up to 10% for $p * \varphi > 0.01$, and for $p * \varphi < 0.01$ the error increases exponentially fast with the decrease of the parameter $p.\varphi$.

5.3 Methods

Two different silica monodisperse bead suspensions with a void fraction of 0.019, and bead radius sizes of 1 and 3 μm (Microspheres-Nanospheres, NY) were employed as control samples. The control measurements were performed on a vertical bore superconducting 4.8 T magnet (Cryomagnetics) with the Apollo console (Tecmag, TX). The silica bead suspensions were shaken prior to each acquisition for a uniform bead distribution. It was impossible to avoid losses of beads during the pipette transfer of the suspension to the MR cell due to their excessive precipitation on all surfaces, with the actual void fraction different from the tabulated one. As a result, in our analysis, we relied on the bead radii as the reliable control parameter.

We completed the bubbly flow measurements on a vertical bore permanent 0.2 T magnet (Oxford Instruments, UK). For these measurements, a 2 cm-diameter cylindrical glass tube was filled with water to the length of 5 cm; with the liquid column entirely within the RF probe sensitivity region. The tube was equipped with a 1.2 cm diameter frit (14-16 μm sized porous glass, "medium" size, Aldrich, ON) at the bottom (figure 5-1). Airflow, regulated at different airflow rates by a Matheson flow meter, was then injected into the water phase through the frit. All bubbly flow measurements were done at 3

specific airflow rates: 12.43, 22.67, and 36.37 CCPM. Water was doped with a small amount of manganese sulfate ($MnSO_4$) to reduce the apparent MR spin-lattice and spin-spin relaxation times for faster acquisition.

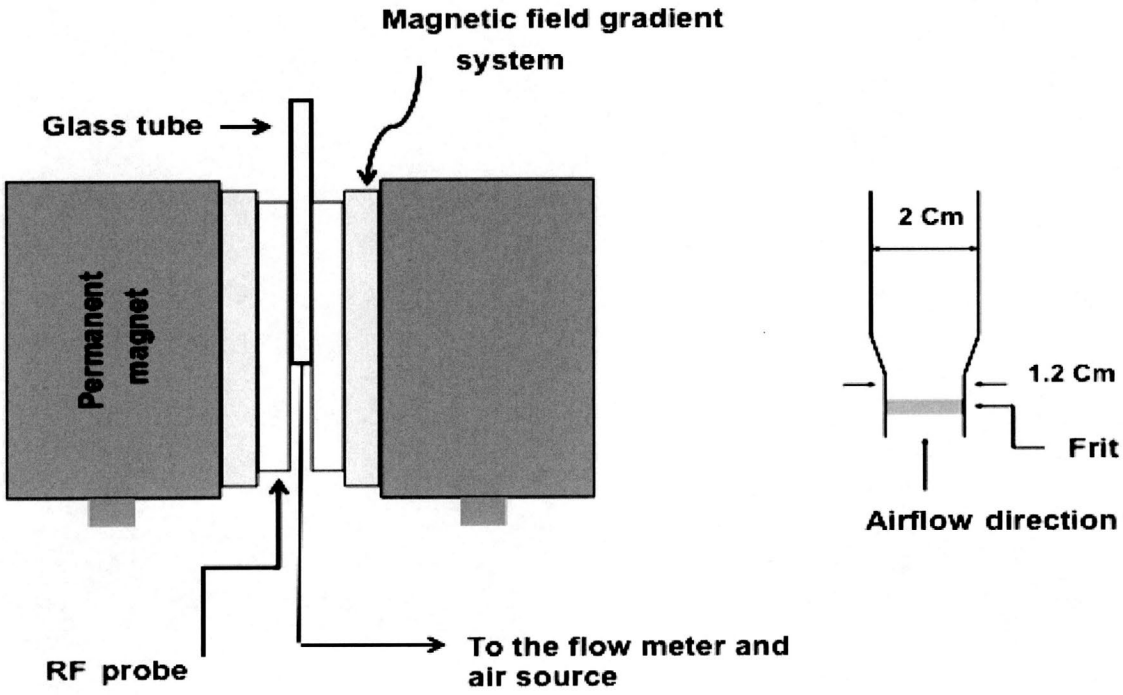

Figure 5-1 Experimental setup for bubbly flow measurements.

Optical measurements were performed with a Dantec Dynamics Nanosense MKIII High speed camera (815 Hz) with resulting image pixel resolution of 39 μm. Only bubbles with well-defined shapes were considered, and those smaller than the camera's resolution, as well as blurry bubbles due to the insufficient focal depth of the camera, were excluded from the measurement. The number of image pixels along the longest diameter of each selected bubble was manually counted, and, then, converted to mm based on the camera's image pixel resolution. The results were then averaged out.

5.3.1 Bulk measurements of void fraction, D, and T_2:

To calculate the void fraction of the bubbly flows, the FID of the $MnSO_4$ solution was acquired with 5120 acquisition points (to be used for the analysis of the FID Gaussian shape), DW 8 μs, and 32 signal averages using the standard single RF pulse sequence. The sample glass tube was filled with the solution to occupy completely the RF probe sensitive volume. The measurements were done for the stationary sample and the above-stated airflow rates. FID amplitudes at 26 μs were used to calculate the bulk void fraction:

$$\varphi = \frac{(M_Z^0 \sin(\alpha))_{st} - (M_Z^0 \sin(\alpha))_{flow}}{(M_Z^0 \sin(\alpha))_{st}} \quad (10)$$

The mechanical dispersion D information of the bubbly flows were collected using the standard PFGSE sequence for Δ=3, 20, and 40 ms. The measurements were done for 8 nonlinearly spaced gradient values (0 – 19.55 g/cm) with δ=350 μs. Diffusion was also

measured in the 1 μm silica bead suspension using the PFGSE with δ=2.25 ms and Δ=12.5 ms for 8 gradient values (0 – 0.36 g/cm).

The MR T_2 relaxation rates were measured from the standard CPMG pulse train at a wide range of echo times t_E: 0.57, 0.65, 0.75, 0.85, 0.95, 1.95, 3.95, 5.95, 9.95, 19.95, 39.95 and 79.95 ms for the 1 μm silica bead suspension, and 0.5, 1, 2, 4, 6, 10, 20, 40, 80, and 100 ms for the bubbly flows. The number of echoes collected, however, was different for different measurement points, and determined by the signal lifetime: from 1024 for 0.57ms t_E to 6 for 79.95 ms t_E for the 1 μm control sample, and from 3072 for 0.5 ms t_E to 16 for 100 ms t_E for the bubbly flows.

The field of flow was calculated for δ=350 μs, Δ=40 ms, and $\Delta G = 0.2$ g/cm to be (-0.43 to +0.43 m/s). The propagator analysis for the highest airflow rate showed a symmetric propagator, with the majority of the water spins stationary. The fraction of the fastest spins to the stationary spins, and to the total number of spins was calculated to be 12.6% and 5.9%, respectively.

5.4 Results and Discussion

5.4.1 Control Measurements

Diffusion D was measured in the 1.0 μm silica bead suspension to be $(2.44 \pm 0.019) * 10^{-9}$ m^2/s at temperature 15°C as read from the gradient set's cooling system. This is slightly greater than the water's molecular self-diffusion coefficient at that temperature, which is most likely caused by beads settling during the signal acquisition.

The susceptibility-induced relaxation rate for the 1 μm silica bead suspension is presented in figure 5-2 for different echo times. The observed almost linear increase in the relaxation rate at longer echo times (i.e. beyond 20 ms, $\tau \gg 1$) agrees with the predicted Eq. (3). The susceptibility-induced relaxation rate was also measured for the 3 μm silica bead suspension at two echo times of 0.57 and 39.95 ms.

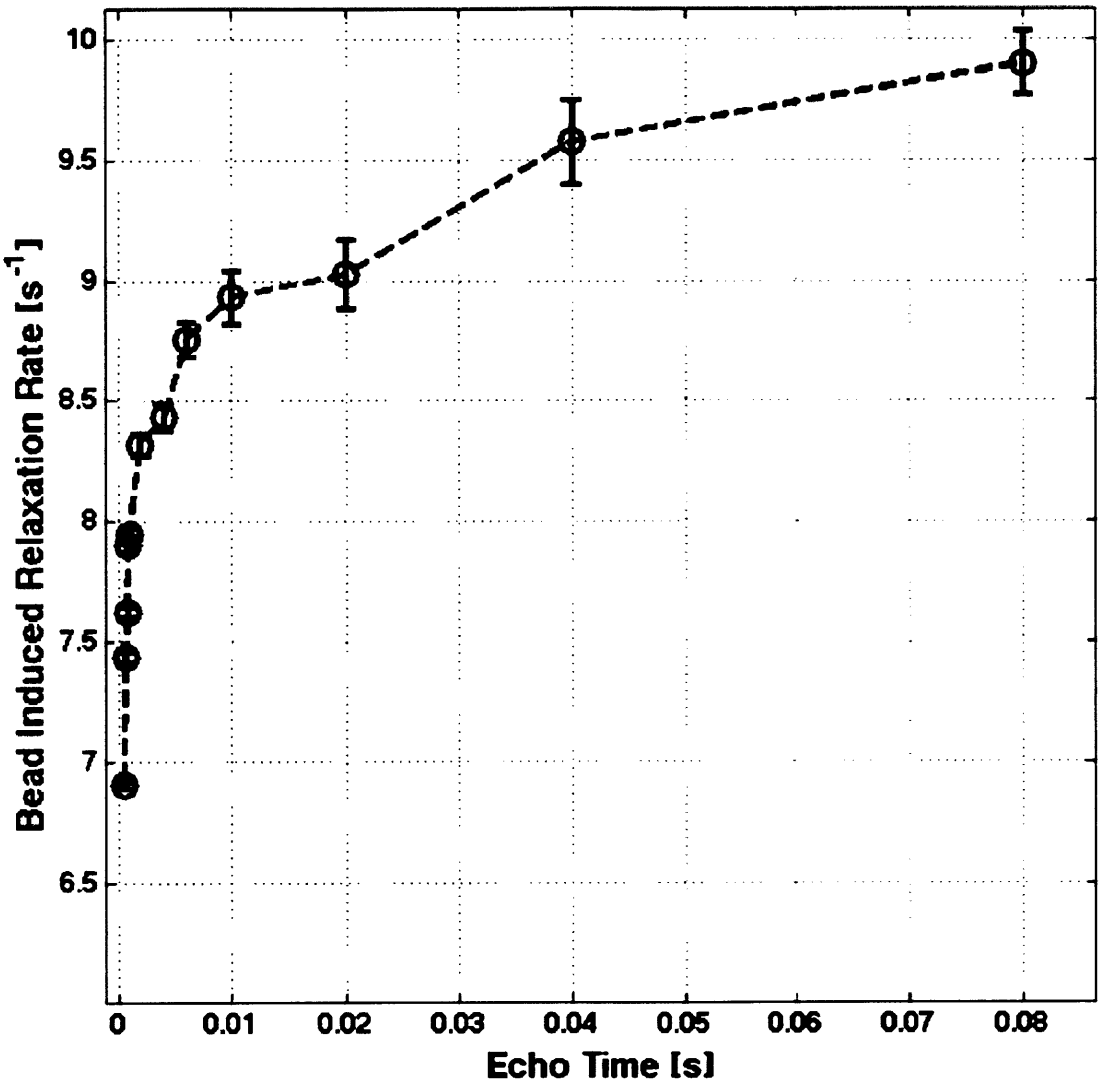

Figure 5-2 Susceptibility induced relaxation rate vs. echo time in the 1 μm silica bead suspension: A direct relation between the induced relaxation rate and echo time is shown. The scale on the horizontal and vertical axes is in s and s^{-1}, respectively. Error bars represent the standard error. The bigger error for longer echo times is due to the smaller number of echoes acquired.

Theoretical accuracy up to 5% is expected using the Gaussian approximation for the 1 μm silica beads, based on the value of the parameter $p.\varphi$ (i.e. 0.0149). Considering the dimensionless time τ of 195 (corresponding to echo time of 80 ms, the longest employed due to the signal lifetime limitations), the linear approximation (Eq. (5)) was employed to calculate the actual void fraction via the bead radius. (As mentioned in the Methods section, the bead size was more reliable control parameter than the tabulated void fraction due to precipitation of beads during the transfer to the cell on the pipette and the cell walls.) The void fraction was found to be 0.0071 ± 0.0001.

Then the 1 μm suspension's void fraction was approximated through the simplified Eq. (7), using the CPMG relaxation rates measured for the bulk water and 1 μm silica bead suspension at the echo times of 0.570 ms and 80 ms. Note that Eq. (7) does not require information on the bead radius. The calculated void fraction was equal to 0.0066 $\pm$ 0.00004, in a good agreement with the value calculated via Eq. (5).

Finally, the bead radius was calculated using the simplified Eq. (8), and obtained 1.04 ± 0.0053 μm, in a very good agreement with the tabulated value of 1.0 μm. Please note that the simplified Eqs. (7) and (8) are independent, and do not require prior knowledge of one of the two parameters, void fraction or bead size, to calculate the other. Therefore, the simplified equations were considered as sufficiently accurate when applied to the control system of 1.0 μm beads.

The discrepancy between the exact bead size and its estimate is partly due to the theory limitations, and partly due to the $t_E \gg t_D$ $(i.e. \tau \gg 1)$ assumption (as discussed by Sukstanskii et al. in [14], even for $\tau = 100$, the difference between an exact result and a linear approximation is still on the order of 10%).

If the requirements for the short and long time limits are not met, the theoretical assumptions will not hold and the discrepancy between the calculated parameters and the true values will increase. In control measurements, it was demonstrated by using 3 μm beads vs. 1 μm beads, which will lead to a difference of 9 in the characteristic diffusion time t_D. For 3 μm beads, assuming the same diffusion as previously, Eq. (8) was employed to calculate the radius of the 3 μm silica beads. It was found to be 1.13 ± 0.043 μm, showing an expected much bigger error (It is also possible that the faster settling of the 3 μm beads in water might impose a bigger D value; its exact measurement was prevented by the fast settling of the beads).

5.4.2 Bubbly Flow Measurements

The bulk void fraction values measured for the bubbly flows were 0.0114 ± 0.0012, 0.0202 ± 0.0016, and 0.0318 ± 0.0014 for airflow rates 11.2, 23.8, and 38.2 CCPM, respectively, which demonstrates a linear relationship between the void fraction and airflow rate. The strong susceptibility driven MR T_2^* effects did not influence the void fraction measurements because of the very short signal evolution time of 26 μs prior to the data acquisition.

Figure 5-3 shows the mechanical dispersion D as a function of Δ in the bubbly flows. As seen, dispersion shows a time-dependent behavior, and it is greatly enhanced for longer Δ times. A direct relation between the airflow rate and dispersion is also suggested by the figure. Changing the rate of the airflow alters the bubble population and their velocity, which affects the degree of disturbance caused to the surrounding water spins.

This is clearly a case of anomalous dispersion. A possible physical model is a combination of strong dispersion events caused by rising bubbles, and weaker ones in the interim. The susceptibility-induced relaxation rate increase is caused by the motion of spins through the bubble-generated magnetic field gradients (i.e. during the strong dispersion event).

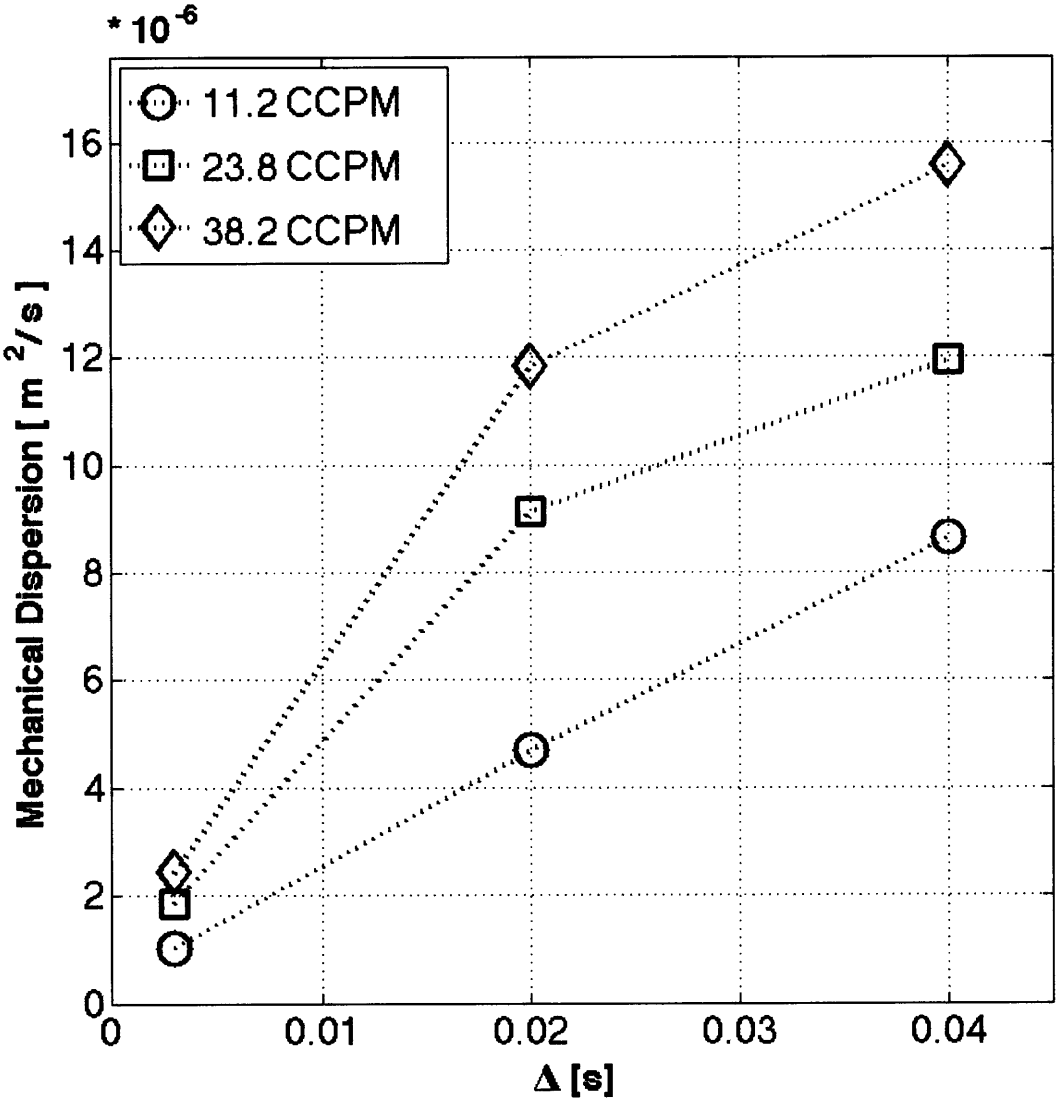

Figure 5-3 Mechanical dispersion vs. Δ in the bubbly flows: Direct dispersion-airflow rate and dispersion-Δ relations are observed. The scale on the horizontal and vertical axes is in s and m^2/s, respectively.

The simplified Eqs. (7) and (8) are derived from (5) and (6) assuming that dispersion next to the bubbles is the same at any echo times. In other words, it is the strong dispersion event that contributes to the relaxation rate change. As long as this dispersion event is close to Gaussian, the simplified equations should be still applicable. To check if this is correct, we calculated the bubble void fraction using Eq. (7). The calculated values were 0.0164 ± 0.0013, 0.0216 ± 0.0017, and 0.0317 ± 0.0027, in excellent agreement with those measured with FID: 0.0114 ± 0.0012, 0.0202 ± 0.0016, and 0.0318 ± 0.0014.

Figure 5-4 presents the bubble induced relaxation rate in bubbly flows for different echo times. Even at the 0.2 T field, the relaxation rate shows the same functional behavior with the echo time as observed for the reference sample. Furthermore, we can detect an increase in the driven relaxation rate with the increase in airflow rate. When air passes with a higher velocity through the frit, larger gaseous bubbles are formed in the water phase, which perturbs the magnetic field within the sample more significantly ($\Delta B_0 \propto R^3$, Eq. (1)) resulting in a more severe drop in the apparent MR spin-spin relaxation time.

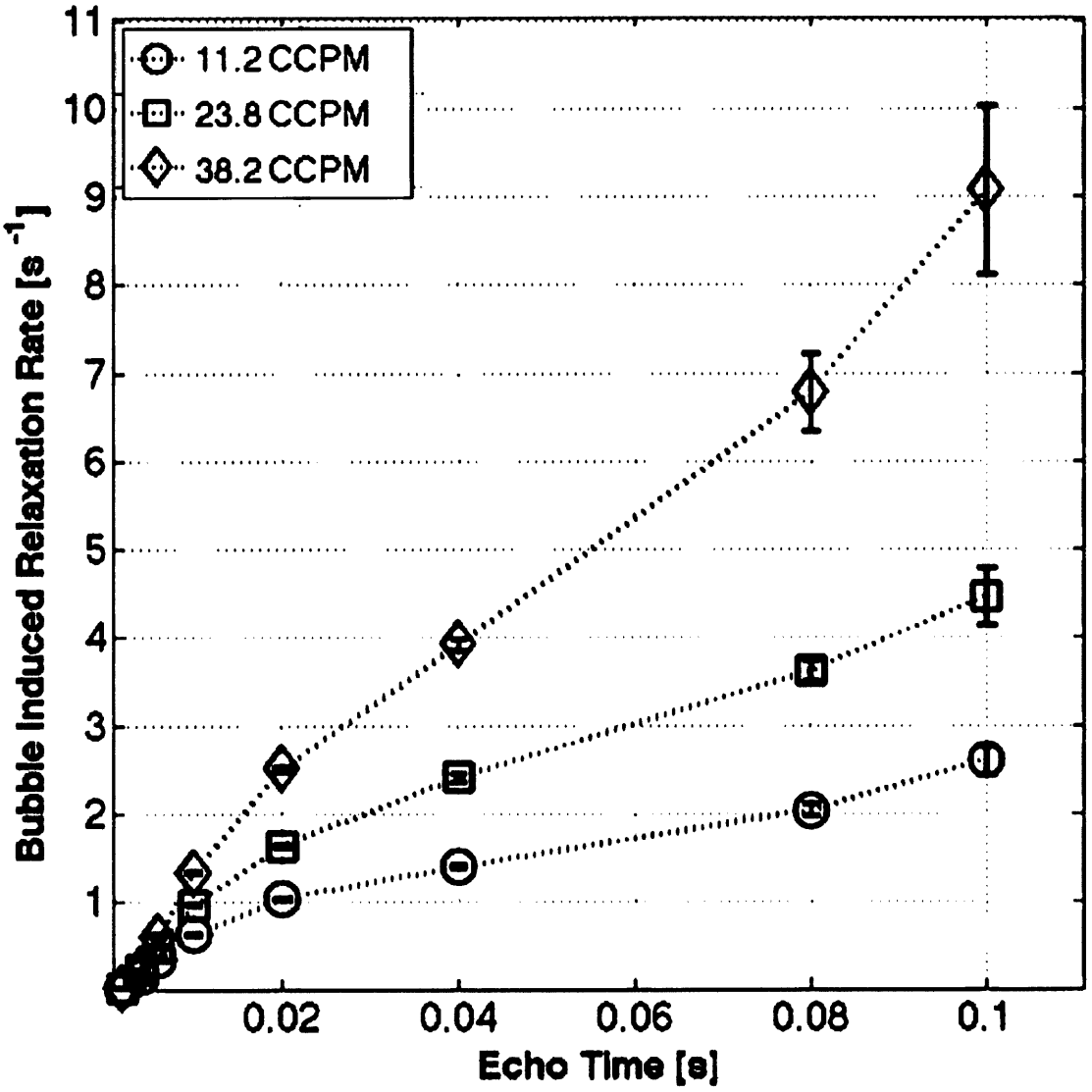

Figure 5-4 Bubble induced relaxation rate vs. echo time in the bubbly flows: A direct relation between the induced relaxation rate, echo time, and airflow rate is observed. The scale on the horizontal and vertical axes is in s and s^{-1}, respectively. Error bars represent the standard error.

According to Eq. (9), and for the void fraction φ and mechanical dispersion D values measured for the bubbly flows at $B_0 = 0.2$ T, the maximum bubble radii which could be reliably estimated using the Gaussian approximation with an accuracy up to 20%, were 342.6, 535.9, and 767.7 μm, for airflow rates 11.2, 23.8, and 38.2 CCPM, respectively. Larger bubble sizes will be underestimated according to Eq. (9).

Figure 5-5 A-C shows the bubble size distribution obtained using the optical measurements and demonstrates the complexity of the bubbly flow systems. As the airflow rate increases, the bubble size distribution broadens, with appearance of bubbles with sizes well beyond the applicability of the presented analytical method. Figure 5-5 D compares the average bubble radius estimates obtained with the MR (Eqs. (5) and (8)) and optical methods. The MR-estimated values with Eq. (5) are 325.2 ± 18.2, 376.9 ± 16.0, and 437.7 ± 11.6 μm for bubbly flows from the lowest to the highest airflow rate, respectively, and the ones obtained from the optical method are 333.4 ± 20, 547.2 ± 56.5, and 959.7 ± 119.3 μm. Although there is a good agreement for the lowest airflow rate, the estimates from the two methods diverge with the airflow rate increase: from 3% for the slowest airflow rate to 2 times difference for the fastest.

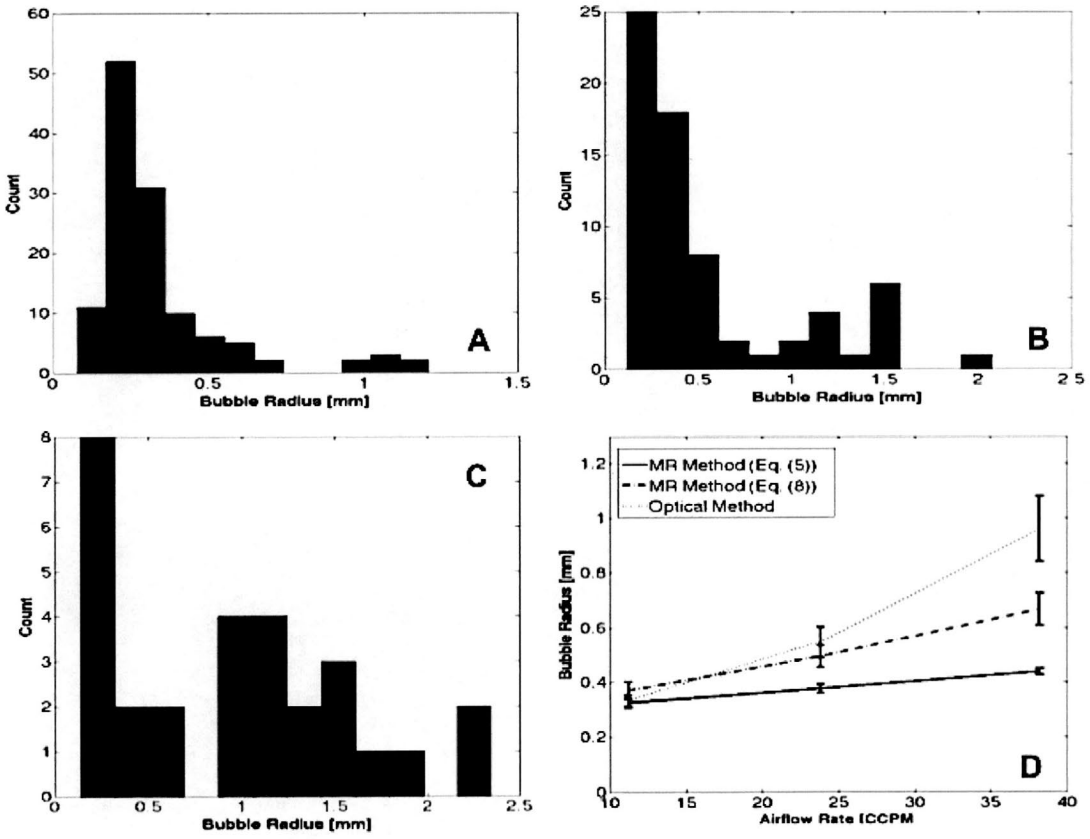

Figure 5-5 (A-C) Bubble size distribution obtained using the optical method for 3 different airflow rates. The scale on the horizontal axis is in mm. (D) Average bubble size estimates from the MR (Eqs. (5) and (8)) and optical techniques. The scale on the horizontal and vertical axes is in CCPM and mm, respectively. Error bars represent the standard error.

Using the simplified Eq. (8), we also estimated the average bubble radius for each airflow rate to be 370.0 ± 15.9, 495.8 ± 20.4, and 666.1 ± 29.4 μm, in better agreement with the optical method than the ones obtained with Eq. (5).

The MR model employed considers bubbles as non-interacting well-separated spherical objects, and this requirement still holds to an acceptable degree for the lowest airflow rate. Analysis of the FID signal for bubbly flows also showed that the Gaussian phase accumulation by diffusing spins was a better approximation for the slowest airflow rate than for the fastest airflow rate (R^2 of 0.9991 vs. 0.9904), meaning that the Gaussian approximation was at least justified for the slowest airflow. However, with the increased airflow rate and a greater number of bubbles in the water phase, bubbles started coalescing more actively, changing to non-spherical shapes, and interacting, which led to the loss of accuracy of the employed model. In addition, the insufficiently long τ time (i.e. roughly 3.4 for the bubbly flows, corresponding to the echo time of 40 ms) added an extra error to the estimates due to the linear approximation made in (5) which is valid only for very long τ values.

On the other hand, the optical method might overestimate the bubble sizes as larger bubbles prevent the detection of smaller ones, and light reflection from bubble surfaces visually exaggerates their size. The limited resolution of the camera also prevented the detection of very small bubbles with a size comparable to the pixel size leading to the higher average estimates.

5.5 Conclusion

In this chapter, we evaluated the applicability of MR methods at a low magnetic field for the measurement of void fraction and average bubble size in a vertically upward bubbly flow. The magnetic susceptibility difference between the air trapped in the bubbles and surrounding water molecules changes the apparent MR spin-spin relaxation time, which permitted us to extract information on the bubble size. Although the susceptibility effects are naturally greater at higher fields, very strong changes in apparent MR spin-spin relaxation time caused by the bubbly flows made possible the implementation of the measurements on a low field system of 0.2 T.

Two simplified equations were derived out of the CPMG transverse relaxation rate expressions in long and short inter-echo time limits. These can be employed to obtain information on the void fraction and inclusions' radius, where the direct measurement of the void fraction and diffusion/mechanical dispersion is not possible, or the magnetic susceptibility of the phases is unknown. Its implementation requires only a standard CPMG measurement at a wide range of echo times.

We employed Gaussian approximation methods previously developed by Sukstanskii et al. for the analysis of the MR SE signal in the presence of impermeable spherical inclusions, and Ziener et al. for the analysis of the CPMG transverse relaxation rate modulated by a simple spherical particle. For very long dimensionless time τ, the long-time expansion of the SE/CPMG signal attenuation function is linear in time, and inclusion size information could be reliably extracted from the standard ΔR_2 relaxation rate. For that to be successful, it is essential that the R^2/D be small compared to the echo time. We examined the validity and accuracy of the Gaussian approximation approach on

two different suspensions of silica beads with bead radii of 1 and 3 μm. The short characteristic diffusion time in the 1 μm silica bead suspension led to acceptably close (< 4%) size and void fraction estimates, while limitations of the longest echo times in the 3 μm silica bead suspension, gave a much greater discrepancy.

The bubbly flows' void fraction values, as estimated by the simplified equation, coincided with the ones directly measured from the FID amplitude. A good agreement was also observed between the average bubble radius estimated by the simplified equation and estimates obtained from the CPMG relaxation rate (Eq. (5)) and optical technique, especially for the lowest airflow rate.

The theoretical analysis by Sustanskii et al. is derived for a Gaussian distribution of displacements near well-separated bubbles so as the number of bubbles increases with the airflow rate and the system dynamics becomes more and more non-Gaussian, the bubble size estimates will be underestimated. The reliability of the method increases for bigger $p * \varphi$ and τ values, which can be achieved for small micro-sized bubbles and long echo times.

Given the limitations of the analytical approach, Monte-Carlo simulations [18,19] can probably be considered as an alternative analysis technique. However, given the nature of the simulations, their use would require mapping of all possible combinations of parameters of interest (void fraction, bubble size distributions, diffusion/dispersion, etc.). This would be extremely time-consuming and not necessarily monotonic. The analytical approach, although crude due to its model limitations, has a benefit of providing a rough estimate of the system parameters immediately.

Despite the complexity of the fluid dynamics in the bubbly flow system, the presented MR measurement and analysis yielded average bubble size estimates reasonably close to those obtained with optical measurement, in particular for the lowest airflow rate flows. In our opinion, this approach shows promise in studies of gas-liquid flows where the size of non-interacting bubbles does not exceed several dozens of microns, and the fluid dynamics can be approximated as Gaussian.

5.6 References

[1] G. F. Lynch, S. L. Segel, "Direct measurement of void fraction of a 2-phase fluid by nuclear magnetic resonance", International Journal of Heat Mass Transfer, 1977, 20, 7–14.

[2] M. S. A. Abouelwafa, E. J. M. Kendall, "Optimization of continuous wave nuclear magnetic resonance to determine in situ volume fractions and individual flow rates in 2 component mixtures", Review of Scientific Instruments, 1979, 50, 1545–1549.

[3] J. Leblond, S. Javelot, D. Lebrun, L. Lebon, "Two-phase flow characterization by nuclear magnetic resonance", Nuclear Engineering and Design, 1998, 184, 229–237.

[4] F. Le Gall, S. Pascal-Ribot, J. Leblond, "Nuclear magnetic resonance measurements of fluctuations in air-water two-phase flow: pipe flow with and without `disturbing' section", Physics of Fluids, 2001, 13, 1118-1129.

[5] N. E. Daidzic, E. Schmidt, M. M. Hasan, S. Altobelli, "Gas–liquid phase distribution and void fraction measurements using MRI, Nuclear Engineering and Design, 2005, 235, 1163–1178.

[6] D.J. Holland, A. Blake, A.B. Tayler, A.J. Sederman, L.F. Gladden, "A Bayesian approach to characterising multi-phase flows using magnetic resonance: Application to bubble flows", Journal of Magnetic Resonance, 2011, 209, 83-87.

[7] J.N. Reyes, "The use of MRI to quantify multi-phase flow patterns and transitions: an application to horizontal slug flow", Nuclear Engineering and Design, 1998, 184, 213-228.

[8] L.F. Gladden, M.H.M. Lim, M.D. Mantle, A.J. Sederman, E.H. Stitt, "MRI visualisation of two-phase flow in structured supports and trickle-bed reactors", Catalysis Today, 2003, 79–80, 203–210.

[9] A.B. Tayler, D.J. Holland, A.J. Sederman, L.F. Gladden, "Time resolved velocity measurements of unsteady systems using spiral imaging", Journal of Magnetic Resonance, 2011, 211,1–10.

[10] A.E. Marble, I.V. Mastikhin, R.P. MacGregor, M. Akl, G. LaPlante, B.G. Colpitts, P. Lee-Sullivan, B.J. Balcom, "Distortion free single point imaging of multi-layered composite sandwich panel structures", Journal of Magnetic Resonance, 2004, 168, 164-174.

[11] M. Sankey, Z. Yang, L. Gladden, M. L. Johns, D. Lister, B. Newling, "SPRITE MRI of bubbly flow in a horizontal pipe", Journal of Magnetic Resonance, 2009, 99, 126–135.

[12] I.V. Mastikhin, A.Arbabi, B. Newling, A. Hamza, A. Adair, "Magnetic resonance imaging of velocity fields, the void fraction and gas dynamics in a cavitating liquid", Experiments Fluids, 2012, 52, 95–104.

[13] A. Arbabi, I.V. Mastikhin, "Magnetic susceptibility based magnetic resonance estimation of micro-bubble size for the vertically upward bubbly flow", Journal of Magnetic Resonance, 2012, 225, 36–45.

[14] A.L. Sukstanskii, D.A. Yablonskiy, "Gaussian approximation in the theory of MR signal formation in the presence of structure-specific magnetic field inhomogeneities. Effects of impermeable susceptibility inclusions", Journal of Magnetic Resonance, 2004, 167, 56–67.

[15] C.H. Ziener, T. Kampf, P.M. Jakob, W.R. Bauer, "Diffusion effects on the CPMG relaxation rate in a dipolar field", Journal of Magnetic Resonance, 2010, 202, 38–42.

[16] R.Dharmakumar, D.B. Plewes, G.A. Wright, "On the parameters affecting the sensitivity of MR measures of pressure with microbubbles", Magnetic Resonance in Medicine, 2002, 47, 264–273.

[17] P.T. Callaghan, "Susceptibility-limited resolution in nuclear magnetic resonance microscopy", Journal of Magnetic Resonance, 1990, Vol. 87(2), 304-318.

[18] R.H. Morris, M. Bencsik, A.K. Vangal, Y. Perrie, "Three-dimensional fluid pressure mapping in porous media using magnetic resonance imaging with gas-filled liposomes", Magnetic Resonance Imaging, 2007, 25, 509–512.

[19] R.H. Morris, M. Bencsik, N. Nestle, P. Galvosas, D. Fairhurst, A. Vangala, Y. Perrie, G. McHale, "Robust spatially resolved pressure measurements using MRI with novel buoyant advection-free preparations of stable microbubbles in polysaccharide gels", Journal of Magnetic Resonance, 2008, 193, 159–167.

6 – Conclusion and future work

6.1 Conclusion

Multi-phase systems, in particular, gas-liquid systems, encompass a wide range of industrial processes. Examples are cavitation (both acoustic and hydraulic), foams, oil transport pipelines, industrial emissions, and etc. In these processes bubbles play a critical role. For a better understanding of these processes, a knowledge of the bubble size is essential. The velocity field and bubble void fraction are other parameters of these systems, which are of interest.

MRI seems a promising technique to study multi-phase systems, because it is inherently 3D, it is non-invasive, and it can be used to study optically and acoustically opaque systems. This thesis examined the employment of MRI techniques, from sophisticated 3D pure phase encode imaging methods to basic methods, for the spatially resolved and bulk measurements of acoustic cavitation and vertical bubbly flows, subsets of two-phase gas-liquid systems, respectively. Pure phase encode MRI methods are immune to time evolution artefcats (e.g. chemical shift, susceptibility difference, and field inhomogeneity). They are also suitable for the measurement of fast flows, because of their short characteristic measurement time. However, pure phase encode methods suffer from low temporal resolution, and do not provide instantaneous information from the medium, as they traverse k-space point-by-point rather than line-by-line.

Due to the magnetic susceptibility difference between the phases in the two-phase gas-liquid systems, the MR T_2 and T_2^* of the liquid phase are shorter than those in the bulk liquid. We used to our advantage the modulation of the MR signal by the magnetic

susceptibility-induced effects to extract bubble size information using existing analytical approaches. Velocity field maps were also extracted for the acoustically cavitating liquid using motion-sensitized pure phase encode imaging methods.

We obtained 3D spatially resolved voidage and velocity maps of the acoustically cavitating liquid for two different samples (water and a surfactant solution) at a magnetic field of 2.4 T. The mono-exponential decay of the FID and the fast dispersion of the water molecules permitted the employment of 3D pure phase encode conical SPRITE with short characteristic measurement times to obtain spatially resolved void fraction maps. 3D velocity data was also obtained with 3D motion-sensitized conical SPRITE.

Vertical bubbly flows were studied at a magnetic field of 4.8 T. We employed an analytical expression originally developed for the MR analysis of stable micro-bubbles to extract both 3D spatially resolved and bulk bubble size information from the susceptibility-induced T_2^* changes. This analytical expression connects the void fraction, bubble size, and MR relaxation. We showed that the void fraction must be measured at as short t_p as possible due to a very strong magnetic susceptibility effect on T_2^*. For the spatially resolved datasets, we obtained the void fraction and T_2^* information with the 3D pure phase encode conical SPRITE. The liquid phase dispersion was measured using the 3D pure phase encode motion-sensitized SE-SPI with reduced k-space sampling for the sake of short total acquisition time. The approach introduced, as expected, underestimated the bubble size at higher airflow rates. This was due to the presence of bigger, non-spherical, and interacting bubbles; violating the theoretical requirements.

We also performed bulk measurements of vertical bubbly flow at a low magnetic field of 0.2 T. Here, susceptibility-induced changes in T_2 were analyzed using approaches

originally developed for the MR analysis of randomly distributed, randomly oriented, and isolated impermeable spheres, and, for a simple model of a spherical particle. Bubble size information was extracted from CPMG signal attenuation at very long inter-echo times. Two simplified equations were also derived based on the CPMG signal attenuation functions at very long and short inter-echo times, to be used for the voidage and inclusion size estimation with basic relaxometry with no need for magnetic field gradient systems (of course, if D is known). The adequateness of the approach was examined with the help of control measurements on silica bead solutions with known bead sizes. Control measurements results agreed well with theory. The results of our bubbly flow measurements were also validated through an independent optics-based technique. A good agreement was observed between the MR and optics-based estimates, especially, for the slowest airflow rate. The method introduced is practical, fast, and reliable, suitable for industry-oriented research where bench-top low magnetic fields are commonly employed. This method lends itself to studies of gas-liquid systems where the size of non-interacting bubbles does not exceed several dozens of microns and the fluid dynamics can be approximated as Gaussian.

6.2 Future work

We showed that the magnetic susceptibility difference in two-phase gas-liquid systems modulates the MR signal. Based on this, we strongly recommend the use of pure phase encode imaging methods in studies where a careful 3D mapping is required. To study multi-phase systems, one can alternatively match the magnetic susceptibility of phases by adding paramagnetic salts [1]. This approach, however, would be difficult, would have

limited range of applications, and, most importantly, would modify the dynamics of the medium by changing the surface tension of the solution and other parameters, with the required concentration of 21.63 mM for Mn^2+ to match the susceptibility of air [2]. In our opinion, using the magnetic susceptibility difference to advantage, is a more universal approach. In addition to bubbly flow studies, we see at least two more areas of research where the approaches developed can be beneficial: gas hydrates and sprays (atomization).

Gas hydrates are naturally occurring, crystalline, ice-like substances composed of gas molecules (methane, ethane, propane, etc.) held in a cage-like ice structure. Gas hydrates are of interest to industry as they block fluid flow in gas pipelines and petroleum wells. They are also considered for energy storage and transportation, and as a potential future source for natural gas. In the hydrate area, the presence of nano-bubbles is an important issue. They appear as spherical regions of high methane concentration during the hydrate dissociation (i.e. release of the gas), when the liquid water phase is supersaturated by methane. These nano-bubbles grow to a certain size, without leaving the water phase. They also act as sites for re-nucleating hydrate as they offer interfacial areas where high concentrations of gas and liquid are in contact. This may be one reason why a "memory effect" (i.e. hydrates are formed much faster from the decomposed hydrate nucleate than if hydrates were formed from the liquids for the first time) is observed. The relation between nano-bubbles and the “memory effect” in gas hydrates can be studied with our developed method, which can also provide an insight into the stabilized size of these nano-bubbles. For an accurate size estimation using Eq. (8) in Chapter 5, for a gas hydrate with nano-bubbles with the average radius of 200 nm and diffusion of $10^{-10}\ m^2/_s$, short and long inter-echo time requirements can be met for any $\tau_{180} < 0.1\ ms$ and

$\tau_{180} > 25$ ms, respectively. Of course, at the short inter-echo time of 0.1 ms, observing any change in the T_2 of water can be very difficult. It makes the employment of a strong magnetic field necessary to enable the detection of any change in the MR T_2, induced by nano-bubbles.

Atomization, the process of generating droplets, refers to the process of forcing liquid through nozzles to generate small droplets of liquid. Each spray can form a range of droplet sizes, which can vary significantly from one type of nozzle to another. Sprays are, in fact, another form of two-phase gas-liquid systems, in which the water phase appears as droplets in the gas phase. Sprays are presently used in almost all industrial operations such as gas cooling, combustion systems, air/gas conditioning, fire suppression, spray drying, and agricultural spraying. Due the wide range of applications, the velocity distributions, and, especially, accurate size information of water droplets in nozzle sprays are important factors in the overall effectiveness of spray nozzle operation. Our proposed technique seems a promising approach to extract the droplet size distribution information. Of course, due to the small volume of the water phase compared to that of the gas phase in sprays, a low SNR can make the detection of MR signal difficult. This, however, might be overcome by employing a high magnetic field and an RF coil with a small sensitive volume. For sprays, with average droplet sizes of 15, 30, and 75 μm and gas diffusion of 10^{-6} m^2/s, meeting the short inter-echo time limit would be rather easy for R=30 and 75 μm with any $\tau_{180} < 0.15$ ms and $\tau_{180} < 1$ ms, respectively. But, for R=15 μm, at least, $\tau_{180} < 0.05$ ms is required, which can be limited by the RF probe dead time. At this short inter-echo time, detecting any change in the gas T_2 relaxation time could be also difficult. On the other hand, employing any $\tau_{180} > 15$ ms and $\tau_{180} > 50$ ms, the long

inter-echo time limit can be perfectly met for R=15 and 30 μm, respectively. Satisfying the long inter-echo time limit, however, for the largest droplet size would be limited by the signal lifetime, as, at least, a $\tau_{180} > 280$ ms would be needed. We can also calculate the range of droplet radii and void fraction values that can be reliably measured using the Gaussian approximation in Chapter 5. Assuming $B_0 = 4.7$ T, $\Delta\chi = 9.41 * 10^{-6}$, and the fixed droplet volume fraction φ of 10%, the maximum droplet radius which could be reliably estimated with the accuracy up to 10% would be 50 μm. For fixed droplet sizes R of 15, 30, and 75 μm, the lower limit for reliable estimation of the droplet volume fraction would be 1%, 4%, and 22%, respectively.

For droplet sizing in sprays, one may also employ the Bayesian approach developed by Holland et al [3]. In this approach, a likelihood function is developed relating the measured MR signal to the bubble size distribution in the multi-phase system. This approach eliminates the need for a stable system during the acquisition, and only assumes a constant average bubble size distribution over time.

6.3 References

[1] A.B. Tayler, D.J. Holland, A.J. Sederman, and L.F. Gladden "Exploring the origins of turbulence in multiphase flow using compressed sensing MRI", Physical Review Letters, 2012, 108, 264505 - 264509.

[2] A. B. Tayler, "Experimental characterization of bubbly flow using MRI", A Thesis submitted for the degree of Doctor of Philosophy, Trinity College, 2011.

[3] D.J. Holland, A. Blake, A.B. Tayler, A.J. Sederman, L.F. Gladden, "A Bayesian approach to characterising multi-phase flows using magnetic resonance: Application to bubble flows", Journal of Magnetic Resonance, 2011, 209, 83-87.

Curriculum Vitae

Candidate's full name: Aidin Arbabi

2010-2014, PhD candidate, University of New Brunswick (UNB), Canada

2007-2009, Master of Science, Royal Institute of Technology (KTH), Sweden

2002-2005, Master of Science, Iran University of Science and Technology (IUST), Iran

1997-2002, Bachelor of Science, Islamic Azad University-Tehran South, Iran

Publications:

[1] A. Arbabi, J. Hall, P. Richard, S. Wilkins, and I. V. Mastikhin, "MR relaxometry of micro-bubbles in the vertical bubbly flow at a low magnetic field (0.2 T)", Journal of Magnetic Resonance, 2014, 249, 16-23.

[2] I.V. Mastikhin and A. Arbabi, "Transiently porous medium: Magnetic resonance imaging studies of acoustic cavitation", Journal of Microporous and Mesoporous Materials, 2013, 178, 3-6.

[3] A. Arbabi and I.V. Mastikhin, "Magnetic susceptibility based magnetic resonance estimation of micro-bubble size for the vertically upward bubbly flow", Journal of Magnetic Resonance, 2012, 225, 36–45.

[4] I.V. Mastikhin, A. Arbabi, B. Newling, A. Adair, and A. Hamza, "Magnetic resonance imaging of velocity fields, the void fraction and gas dynamics in a cavitating liquid", Journal of Experiments in Fluids, 2012, 52(1), 95-104.

Conference Presentations:

[1] A. Arbabi and I.V. Mastikhin, "Magnetic resonance study of micro-bubbles in the upward vertical bubbly flow at the low magnetic field of 0.2 T", 27th edition of the MOOT NMR Symposium in Montreal, Canada, 18th-19th October 2014 (poster).

[2] A. Arbabi and I.V. Mastikhin, "Average bubble size estimation in an upward vertical bubbly flow at a low magnetic field (0.2 T)", 12th International Conference on Magnetic Resonance Microscopy (ICMRM 12) in Cambridge, UK, 25th-29th August 2013 (poster).

[3] A. Arbabi and I.V. Mastikhin, "Bubble size estimation in an upward vertical bubbly flow using pure phase encoding magnetic resonance methods", 11th International Bologna Conference on Magnetic Resonance in Porous Media (MRPM 11) in Guildford, UK, 9th-13th September 2012 (poster).

[4] A. Arbabi, I.V. Mastikhin, B. Newling, A. Adair, and A. Hamza, "MRI measurement of the void fraction and velocity field in an acoustically cavitated liquid", 10th

International Bologna Conference on Magnetic Resonance in Porous Media (MRPM 10) in Leipzig, Germany, 12th-16th September 2010 (poster).

[5] A. Arbabi and S.M. Rejaai "Ergonomic design of bus operator's workstation with the aid of functional design relationship", 12th Iranian biomedical engineering conference in Tabriz, Iran, March 2006 (oral)

[6] A. Arbabi and S.M. Rejaai, "Ergonomic design and evaluation of inter-city bus operator's workstationof bus operator's workstation with the aid of functional design relationship", 4th international industrial engineering conference in Tehran, Iran, 11th-12th March 2005 (oral).